On tailored three-dimensional optical materials by atomic layer deposition

Zur Erlangung des akademischen Grades eines
DOKTORS DER NATURWISSENSCHAFTEN
von der Fakultät für Physik des
Karlsruher Instituts für Technologie (KIT)

genehmigte

DISSERTATION

von

Dipl.-Phys. M. Sc. Andreas Markus Frölich
aus Hannover

Tag der mündlichen Prüfung:	24.5.2013
Referent:	Prof. Dr. Martin Wegener
Korreferent:	Prof. Dr. Kurt Busch

Publications

Parts of this thesis have already been published in peer-reviewed scientific journals:

- A. Frölich, J. Fischer, T. Zebrowski, K. Busch, and M. Wegener, "Titania woodpiles with complete three-dimensional photonic bandgaps in the visible", Advanced Materials, accepted (2013).

- A. Frölich and M. Wegener, "Spectroscopic characterization of highly doped ZnO films grown by atomic-layer deposition for three-dimensional infrared metamaterials, Optical Materials Express **1**, 883-889 (2011).

Parts of this thesis have been presented at scientific conferences (only own presentations):

- A. Frölich and M. Wegener,"Highly doped ZnO films with tailored plasma frequency grown by atomic-layer deposition for three-dimensional infrared metamaterials", **contributed talk**, **DPG Spring Meeting**, Berlin, Germany, March 2012.

- A. Frölich, J. Fischer, T. Zebrowski, I. Staude, K. Busch, and M. Wegener, "Towards Visible-Wavelength Titania-Based Three-Dimensional Photonic-Band-Gap Materials *via* Direct Laser Writing", **contributed talk**, **SPIE Photonics West 2012**, San Francisco, USA, January 2012.

Additional work on related topics has been published in peer-reviewed scientific journals:

- A. Vlad*, A. Frölich*, T. Zebrowski*, C. A. Dutu, K. Busch, S. Melinte, M. Wegener, and Isabelle Huynen, "Direct Transcription of Two-Dimensional Colloidal Crystal Arrays into Three-Dimensional Photonic Crystals", Advanced Functional Materials **23**, 1164-1171 (2013).
  *:contributed equally

- J. K. Gansel, M. Latzel, A. Frölich, J. Kaschke, M. Thiel, and M. Wegener, "Tapered gold-helix metamaterials as improved circular polarizers", Applied Physics Letters **100**, 101109-1-3 (2012)

- I. Staude, C. McGuinness, A. Frölich, R. L. Byer, E. Colby, and M. Wegener, "Waveguides in three-dimensional photonic bandgap materials for particle-accelerator on a chip architectures", Optics Express **20**, 5607-5612 (2012)

- T. Bückmann, N. Stenger, M. Kadic, J. Kaschke, A. Frölich, T. Kennerknecht, C. Eberl, M. Thiel, and M. Wegener, "Tailored 3D Mechanical Metamaterials Made by Dip-in Direct-Laser-Writing Optical Lithography", Advanced Materials **24**, 2710-2714 (2012)
- C. E. Kriegler, M. S. Rill, M. Thiel, E. Müller, S. Essig, A. Frölich, G. von Freymann, S. Linden, D. Gerthsen, H. Hahn, K. Busch, and M. Wegener, "Transition between corrugated metal films and split-ring-resonator arrays", Applied Physics B **96**, 749-755 (2009)

Contents

Publications i

1 Introduction 1

2 Fundamentals 5
2.1 Description of light and matter . . . 5
2.2 Optical properties of three-dimensionally and periodically structured media . . . 6
2.2.1 Comparison: Vacuum vs photonic crystal . . . 8
2.2.2 Scaling properties . . . 12
2.3 Subwavelength structures . . . 14
2.3.1 Interaction of electromagnetic fields with matter - from the microscopic picture to effective material parameters . . . 14
2.3.2 Drude metals . . . 17
2.3.3 Metamaterial perfect absorber . . . 20
2.3.4 Hyperbolic metamaterials . . . 21

3 Template assisted atomic layer deposition 25
3.1 Templates by stimulated-emission depletion inspired direct laser writing 25
3.2 Atomic layer deposition . . . 28
3.2.1 The concept of atomic layer deposition . . . 28
3.2.2 The details of atomic layer deposition . . . 33
3.3 Deposition of Al_2O_3 . . . 36
3.4 Deposition of ZnO . . . 37
3.5 Deposition of TiO_2 . . . 37
3.5.1 Precursor screening . . . 37
3.5.2 Refractive index of ALD grown TiO_2-films . . . 39

4 Doped ZnO films with tailored plasma frequencies 43
4.1 Approach to deposition of tailor-doped films . . . 43
4.2 Spectroscopic characterisation of tailor doped ZnO-Films . . . 45
4.3 Understanding the spectra of doped ZnO-films . . . 47
4.4 So how well can we tailor the permittivity and what about nanofabrication? . . . 51
4.4.1 Range of accesible permittivities . . . 51
4.4.2 Nanofabrication . . . 51

5 Titania double-inversion for photonic crystals **59**
5.1 Implications for design and fabrication 59
5.1.1 The double-inversion concept 59
5.1.2 Limitations of inversion by ALD 60
5.1.3 Implications for bandstructure calculations and design 61
5.1.4 Non-destructive determination of woodpile dimensions 63
5.2 Implementation of the titania double-inversion 64
5.2.1 DLW of large samples and for long writing times 64
5.2.2 Titania double-inversion 70

6 A complete photonic bandgap material for visible light **75**
6.1 Description of the sample 75
6.2 Setup for angle- and polarisation-resolved transmission spectroscopy . 76
6.3 Experimental results and comparison to theory 78
6.4 Outlook: Angle-resolved photon emission spectroscopy 82

7 Conclusion and outlook **89**

Appendix **95**
1 Silanisation 95
2 Sample $FSL212_4$ 96

Bibliography **99**

Acknowledgments **111**

1 Introduction

For me, optics could be defined as the science and technology of the creation, manipulation and detection of light. While applications of light are manifold, the most ubiquitous, from my point of view, is vision. In the process of vision, light is created by a light source, impinges onto the object we will eventually perceive and interacts with it and then enters our eye. Here, it is manipulated by the lens that's part of our eye and finally detected by the cones and rods sitting on the retina. The functionality of the lens is imparted onto it by the combination of its shape and the refractive index of the material it is made of. If one enjoys the view from the top of a mountain, the lens in the eye will have a different shape than the one it would have when reading a book, enabling us to see clearly in both situations. Another example of how the shape of a material alone can be used to tailor its optical functionality is the following one: Glass can either be formed into a window or into the shape of a lens. The former allows clear view across it while the latter has an imaging functionality. Both objects are a lot larger than the wavelength of visible light. Thus, it has been possible since a long time to manufacture them more or less easily. However, there are limits to what one can do by shaping alone if one desires to stick to macroscopic shapes.

Let's take a prism as an example. If one wants to build a prism to separate light passing through it into its different spectral components, the spatial seperation of the different wavelengths at the exit face of the prism can be controlled by its size. The maximum angular deviation attainable is,however, given by the dispersion of the material.

Therefore, the question arises whether it is possible to make materials with tailored optical properties. One approach that has a long and well developed tradition is again found in glass making: Here, different mixtures can be used to fine tune the refractive index or the mechanical properties of glass. The variation of the lead content to change the color or hardness of glass is one prominent example. In the more recent past, however, the advent of micro- and nanotechnology has made the following question one of practical, rather than just intellectual, relevance: Is it possible to tailor an object's optical properties by shaping it at scales comparable to or smaller than the wavelength of light? A grating is an example where a new functionality (the ability to diffract) is imparted to a material by structuring its surface at the scale of half a wavelength.

In this thesis I am looking at tailored, three-dimensional optical materials. I am not treating gratings or other two-dimensional approaches because the most general case of a tailored optical material is a bulk material, as the example of the prism illustrates. The valid question of how to structure a material in three dimensions immediately arises from this approach. Different approaches to solve this challenge

exist. Some of them rely on top-down methods such as self-assembly [1, 2] while others use two-dimensional structuring techniques in a layer-by-layer fashion [3–5]. Three-dimensional structures can be arrived at using holographic lithography in one processing step [6, 7]. It is inherent to this approach to yield periodic structures only. The lithographic technique of direct laser writing (DLW) [8–10] allows for the creation of almost arbitrarily shaped polymer nano- and microstructures. Thus, it is a great tool for three-dimensional structuring but it is limited to one material. If it were possible to replicate, invert or coat a structure made by DLW with a material of choice while maintaining the shape, almost limitless freedom of design would be available.

This challenge is similar to the attempt to homogeneously coat all surface of the outside and the inside of a car without disassembling it. With traditional, directional evaporation techniques in which material travels from the source to the surface along a straight line this is obviously not possible, unless a multitude of surfaces can be created inside the car. With the coating technology of atomic layer deposition (ALD) a different approach to coating provides the solution to this challenge [11]: In ALD, a chemical is emitted from a source as a vapor that only forms a monolayer on the surface. Once that this monolayer is deposited, the vapor does not form material anymore and the excess vapor is pumped away. A second vapor that is reactive to the first one can then be used to react with the monolayer just deposited on the surface to form the desired material. Provided that the window is opened, all surfaces of the car can then be coated in a monolayer-by-monolayer fashion by pumping the vapors in and out of the car one vapor after the other. This quality of ALD makes it an extremely useful technique to coat or replicate three-dimensional micro- and nanostructures. For the replication of some of the structures considered in this thesis, we wanted to completely fill cylindrical pores with a diameter of 100 nm and a length of 135 µm using ALD. For a car, this would correspond to coating the inside of the whole car using a window that is opened a mere 1.5 mm – and that the opening is getting steadily smaller and eventually closes as the process continues.

Thus, the combination of ALD and DLW seems a promising route for the fabrication of tailored, three-dimensionally nanostructured optical materials, with DLW providing a geometry and ALD being used to impart this geometry onto a material. There are two approaches to put this combination to use that I have investigated:

The first one is the avenue of metamaterials, an approach to tailoring optical properties that Sir John Pendry [12] is usually given credit for. It has some similarity with the “chemical” route known from making tailored glasses in that the goal is a material that can be considered to be homogeneous. In a metamaterial, the effective properties are tailored by a proper design of its constituents. These constituents are usually rationally designed nanostructures and are of subwavelength size such that a homogeneous material results. Often, one wishes to use a nanostructure made of a material having a moderately negative permittivity. To make this possible, I have investigated a method to deposit tailor-doped semiconductor films by ALD. With ALD, the doping can be controlled straighforwardly to a great extent and can be used to control the permittivity at optical frequencies. Therefore, the grown material is a

tailored material in its own right. However, since it is grown by ALD, its use can be combined with DLW, resulting in even more possibilities for the design of optical materials.

Photonic crystals are the second approach. This approach is less drastic in terms of the constituent materials employed and Sajeev John [13] and Eli Yablonovitch [14] are usually credited for having invented this class of materials. They are composites of two materials as well, but they derive their unusual properties from the fact that they are periodically arranged in the form of a three-dimensional crystal with a lattice constant on the order of the wavelength of interest. This leads to a drastic modification of the allowed states of the electromagnetic field inside these materials, quite similar to the processes leading to the formation of a band structure for electrons in a crystal. The commonly known dispersion relation for homogeneous media does not apply in these materials any more. The physical properties that can be deduced from it in the case of homogeneous media now have to be reduced from the band structure. In return, all of these properties can then be set by properly tailoring the crystal to have an appropriate band structure. The property that I tried to tailor in this work was the density of states. If properly designed, the band structure of a photonic crystal can be made to have a frequency region void of any bands. This frequency range is then called a complete photonic bandgap. Its existence implies a vanishing density of states for propagating electromagnetic modes. This is the origin of the term "tailored electromagnetic vacuum". Up to now, no photonic crystals with a vanishing density of states for visible light have been reported. The two necessary ingredients for making such a crystal are a sufficiently small lattice constant and an appropriate contrast of permittivities of the two constituent materials. I combined stimulated emission depletion DLW (STED-DLW), a resolution-enhanced version of DLW that was recently developed by Joachim Fischer at the Institute of Applied Physics at the Karlsruhe Institute of Technology in Germany [10] with selective etch material removal methods and ALD deposition of titania. After properly optimizing the geometrical design of the photonic crystal for the constraints imposed by this fabrication method and optimizing the processes, it was possible to fabricate the first photonic crystal exhibiting a complete photonic bandgap for visible light.

In a nutshell, then, this thesis deals with artificial materials that are designed to have specially tailored optical properties. The **outline of this thesis** is as follows:

In **Chapter 2**, I will line out the theoretical foundations for the concepts of metamaterials and photonic crystals that are necessary to appreciate the necessity of the steps undertaken in this thesis and the effects arising.

Both, the metamaterial and the photonic crystal route towards tailoring optical properties were followed in this thesis using ALD. ALD relies on a chemical reaction leading to film growth that is split up into two (or more) selfterminating reactions. In **Chapter 3**, I will show how ALD processes can be performed in general and which points have to be considered to maintain the selfterminating property that is necessary for the coating of three-dimensional templates. The measured properties of

the films grown for the remainder of this thesis and the processes are also discussed here. The necessary templates for structuring in three dimensions are arrived at by the technique of DLW and STED-DLW. An introduction to these techniques is also given in that chapter to the extent that is necessary for this thesis.

In **Chapter 4**, I will show that ALD can be exploited to deposit films of doped ZnO with tailored permittivities that can be tailored at will over a range between 4 and -25. I will also show the different nanofabrication methods that are suitable for this material.

Chapter 5 describes the processes that have been developed or that needed to be refined beyond the state-of-the-art at the beginning of this thesis to produce a titania photonic crystal from a polymer template. The material chemistry of titania is different from that of silicon such that a straightforward adaption of an existing double-inversion procedure [15] for silicon is non-trivial. Also, the feature size of the photonic crystals I produced is much smaller than in the case of silicon photonic crystals. This necessitates a much more careful treatment of process imperfections both during the lithography step and the double-inversion procedure. This treatment is expanded such that the imperfections are already taken into account during the design process for the photonic crystals.

In **Chapter 6**, I will discuss experiments on the photonic crystals obtained using the newly developed double-inversion procedure that give credible evidence for the existence of a complete photonic bandgap between 424 THz and 431 THz. This corresponds to wavelengths between 696 nm and 707 nm, which is completely inside the visible part of the electromagnetic spectrum. Finally, I will sketch a method for the investigation of photonic crystals that has become available with the produced samples.

I will conclude on the work and line out some avenues to develop the presented work further.

2 Fundamentals

As outlined in the introduction, the goal of this thesis was to create tailored optical materials. In this chapter, I will present the theoretical foundations of the two ways towards this goal that were pursued. One approach was to create a photonic crystal, *i.e.*, a periodic, three-dimensional structure composed of at least two materials with different refractive indices that has a lattice constant on the order of the wavelength of operation. This system can be treated using methods known from solid-state physics. As we will see, there is an analogy between propagation of electromagnetic waves in photonic crystals and the propagation of electronic waves in "conventional" crystals. Especially, such photonic crystals can exhibit a complete photonic bandgap, *i.e.*, a frequency range for which no propagating modes exist.

The other approach is based on metamaterials which are materials composed of functional units that are significantly smaller than the operating wavelength of the material and which determine effective material properties ϵ and μ of the metamaterial.

2.1 Description of light and matter

Maxwell's equations supplemented by the constitutive relations describe the interaction of light and matter in a macroscopic way. In the absence of free charges and currents the Maxwell equations read:

$$\boldsymbol{\nabla} \cdot \boldsymbol{D} = 0 \tag{2.1}$$

$$\boldsymbol{\nabla} \cdot \boldsymbol{B} = 0 \tag{2.2}$$

$$\boldsymbol{\nabla} \times \boldsymbol{E} + \frac{\partial \boldsymbol{B}}{\partial t} = 0 \tag{2.3}$$

$$\boldsymbol{\nabla} \times \boldsymbol{H} - \frac{\partial \boldsymbol{D}}{\partial t} = 0 \tag{2.4}$$

and the constitutive relations are

$$\boldsymbol{D} = \epsilon_0 \boldsymbol{E} + \boldsymbol{P} = \epsilon_0 \epsilon \boldsymbol{E} \tag{2.5}$$

$$\boldsymbol{B} = \mu_0 \boldsymbol{H} + \boldsymbol{M} = \mu_0 \mu \boldsymbol{H} \tag{2.6}$$

The vector fields $\boldsymbol{E}$, $\boldsymbol{B}$, $\boldsymbol{H}$, and $\boldsymbol{D}$ are the electric field, the magnetic induction density, the magnetic field and the dielectric displacement. Here, by virtue of the last equality-sign in equations 2.5 and 2.6, I have limited myself to field strengths that are sufficiently small to cause a linear response only. Matter enters *via* ϵ and μ, which describe the dielectric permittivity and magnetic permeability of the materials

considered. They are, therefore, in general functions of space and can have tensorial character. For the following, I will only consider non-magnetic materials, *i.e.*, I will always set $\mu = 1$. This is a good assumption at optical frequencies for natural materials.

Now, by replacing $\boldsymbol{D}$ by $\epsilon\epsilon_0\boldsymbol{E}$ in equation 2.4, dividing it by ϵ and taking the curl we arrive at

$$\boldsymbol{\nabla} \times \frac{1}{\epsilon}\boldsymbol{\nabla} \times \boldsymbol{H} = \epsilon_0 \frac{\partial}{\partial t}\boldsymbol{\nabla} \times \boldsymbol{E}$$

from which we can eliminate $\boldsymbol{E}$ in favor of $\boldsymbol{H}$ using equations 2.3 and 2.6. We thus arrive at

$$\boldsymbol{\nabla} \times \frac{1}{\epsilon}\boldsymbol{\nabla} \times \boldsymbol{H} = -\mu_0\epsilon_0 \frac{\partial^2}{\partial t^2}\boldsymbol{H} \tag{2.7}$$

Considering the most trivial case of vacuum, *i.e.*, an isotropic medium for which $\epsilon = 1$, $\mu = 1$ and using the Grassman-identity, this equation simplifies to

$$\boldsymbol{\nabla} \times \boldsymbol{\nabla} \times \boldsymbol{H} = \boldsymbol{\nabla} \cdot \left(\underbrace{\boldsymbol{\nabla} \cdot \boldsymbol{H}}_{=0} \right) - \triangle \boldsymbol{H} = -\mu_0\epsilon_0 \frac{\partial^2}{\partial t^2}\boldsymbol{H} \tag{2.8}$$

which is the "usual" wave equation and is solved by plane-waves of the form

$$\boldsymbol{H} = \boldsymbol{H}_0 \cdot \exp(\mathrm{i}(\boldsymbol{kr} - \omega t)) \tag{2.9}$$

for almost arbitrary choices of wavevector $\boldsymbol{k}$ and angular frequency ω. The only condition that these quantities have to satisfy is the dispersion relation:

$$\omega^2 = c_0^2\boldsymbol{k}^2 \tag{2.10}$$

Here, the quantity $c_0 = 1/\sqrt{\epsilon_0\mu_0}$ has the value $c_0 \approx 3 \cdot 10^8\,\mathrm{m/s}$. Looking at equation 2.9 again, we see that a point of arbitrary but fixed phase $\phi_0 = (kx_0 - \omega t_0)$ will occur for all space-time coordinates fulfilling $x_0 = (\phi_0 + \omega t_0)/k = \phi_0/k + c_0 t$, *i.e.*, c_0 is the phase velocity of light in vacuum and is independent of k and ω. Here we have looked at one dimension for simplicity. Analogously, in three dimensions, a plane of constant phase propagates with the same speed.

2.2 Optical properties of three-dimensionally and periodically structured media

I will now outline the effects that arise when one considers light propagation in media that have a periodically varying permittivity. These are called photonic crystals. The concept for a photonic crystal discussed here was introduced simultaneously by Sajeev John [13] and Eli Yablonovitch [14] in 1987 together with a prediction of some of the effects arising.[1] For the purpose of this section, I will restrict myself to the

[1] The eigenvalue-treatment of a photonic crystal outlined here loosely follows the treatment in the book by Joannopoulos *et al.* [16].

case of isotropic constituent materials. We will see that this problem is in wide parts analogous to the problem of electrons in a crystal and we will make use of this analogy to solve the optical problem and explain the effects arising. I will also compare some of these effects to their free-space analoga.

Passing from light propagating in a homogeneous medium such as vacuum to the case of three-dimensionally periodic photonic crystals, things turn more complicated than in equation 2.8 as ϵ now depends on all spatial coordinates. Since these crystal are made by a three-dimensional, periodic repetition of a motif of (at least) two materials 1 and 2 having different dielectric permittivities, the permittivity ϵ of the composite is lattice-periodic. This means that $\epsilon(\boldsymbol{r} + \boldsymbol{R}) = \epsilon(\boldsymbol{r})$ for all lattice-vectors $\boldsymbol{R}$ that are elements of the corresponding crystal lattice. ($\boldsymbol{R} = n_1\boldsymbol{a}_1 + n_2\boldsymbol{a}_2 + n_3\boldsymbol{a}_3$ - with n_1, n_2, n_3 being integers and $\boldsymbol{a}_1$, $\boldsymbol{a}_2$, $\boldsymbol{a}_3$ being a set of basis vectors that span a primitive unit cell of the lattice).

The step we made to get from equation 2.7 to equation 2.8 is not permissible any more now. Instead, we can consider

$$\hat{L}(\boldsymbol{r})\boldsymbol{H} := \boldsymbol{\nabla} \times \left(\frac{1}{\epsilon(\boldsymbol{r})} \boldsymbol{\nabla} \times \boldsymbol{H}(\boldsymbol{r}) \right) = \frac{\omega^2}{c_0^2} \boldsymbol{H}(\boldsymbol{r}) \tag{2.11}$$

as an eigenvalue problem for the magnetic field $\boldsymbol{H}$, with an operator $\hat{L}(\boldsymbol{r})$ and eigenvalues $\frac{\omega^2}{c_0^2}$. Since $\hat{L}(\boldsymbol{r})$ is invariant under translations by a lattice vector $\boldsymbol{R}$, we know that Bloch's theorem applies. Therefore we can obtain all solutions by considering only those wavevectors $\boldsymbol{k}$ lying in the first Brilluoin-zone of the reciprocal lattice. For a given $\boldsymbol{k}$ we then expect to find an infinite number of solutions $\boldsymbol{H}_{\boldsymbol{k},\tilde{n}}$ with different frequencies $\omega_{\tilde{n}}$. We can sort and relabel these solutions with an index n in an ascending order by their frequencies $\omega_{\tilde{n}}$ starting with $n = 1$ for the lowest-frequency solution. The index n is then called the band-index and all the pairs ($\boldsymbol{k}$, ω_n) having the same index are said to form the n-th band. A band can then be thought of as a function that maps every point in the Brillouin zone onto an eigenfrequency.

At this point we see the first difference between the electromagnetic fields in photonic crystals and those in free space: Whereas there is a "simple" dispersion relation in free space that relates ω and $\boldsymbol{k}$, we will in general find a more complicated relationship between $\boldsymbol{k}$ and ω in a photonic crystal. This set of solutions is referred to as the photonic band structure of the photonic crystal in analogy to the electronic band structure.

The photonic band structure depends solely on $\epsilon(\boldsymbol{x})$, *i.e.*, on the motif and crystal-lattice and on the magnitude of $\epsilon(\boldsymbol{x})$, *i.e.*, on the strength of the modulation of the permittivity. It can be calculated numerically using a plain-wave expansion method implemented in the freely available software package "MIT photonic bands", MPB in short. [17] MPB takes a wave-vector $\boldsymbol{k}$ and calculates the eigenfrequencies of the first n bands for Blochwaves of this wave-vector. In principle, it is possible to obtain the complete band structure in this way by calculating the eigenfrequencies of every wavevector. Some times, as in parts of this thesis, one is primarily interested in finding the positions of the extrema of the bands. Even though I and others [18] are not aware

of any general proof or justification for this, the extrema are considered to usually occur along lines of high symmetry in the irreducible Brillouin zone. Counterexamples exist [19]. Reference [18] shows from symmetry considerations that for some points in the Brillouinzone, band extrema have to occur.

Let us take the most important photonic crystal of this thesis, the woodpile photonic crystal [20], as an example. It is derived from a face-centered cubic (fcc) lattice with lattice vectors $\boldsymbol{a}_{1,\mathrm{fcc}} = \frac{a_{\mathrm{fcc}}}{2}(\hat{y}+\hat{z})$, $\boldsymbol{a}_{2,\mathrm{fcc}} = \frac{a_{\mathrm{fcc}}}{2}(\hat{x}+\hat{z})$, and $\boldsymbol{a}_{3,\mathrm{fcc}} = \frac{a_{\mathrm{fcc}}}{2}(\hat{x}+\hat{y})$ by placing a motif of two dielectric rods of length $\sqrt{(1/2)}a_{\mathrm{fcc}}$ on every lattice point, where a_{fcc} is the length of the conventional cubic fcc unit-cell.[2] The axes of the rods are pointing along the directions $\boldsymbol{d}_1 = \hat{y}+\hat{z}$ and $\boldsymbol{d}_2 = \hat{y}-\hat{z}$ and they are running through points displaced by $\boldsymbol{p}_1 = \frac{1}{8}(\hat{x}+\hat{y}+\hat{z})$ and $\boldsymbol{p}_2 = -\frac{1}{8}(\hat{x}+\hat{y}+\hat{z})$ from the lattice point.[3] Because of this displacement by a quarter of a space-diagonal, a woodpile photonic crystal is refered to as having a diamond-structure, see Figure 2.1. The Brillouinzone of this lattice is depicted in Figure 2.1b together with its irreducible part. The high-symmetry points are also depicted.

We know from Reference [18] that we will necessarily find extrema at the X, L, and Γ-point. If we are, however, interested in finding all the extrema of the band structure of such a woodpile photonic crystal we have to consider all wavevectors on the colored lines in Figure 2.1b. For the section of the band structure shown in Figure 2.1c, each line connecting two high-symmetry points was discrectized into 64 points and the first 9 bands were calculated.

The woodpiles produced in this thesis are derived from a point-lattice that is compressed along the stacking direction by a factor $s < 1$ with respect to the fcc-lattice. The reasons for this are related to the fabrication method as discussed in Chapters 3 and 5. The lattice is then called centered tetragonal and the corresponding irreducible Brillouinzone, as shown in Figure 2.2, is bigger and has more corners than the irreducible Brillouin zone of an fcc-lattice with the same in-plane lattice constant a_{fcc}.

2.2.1 Comparison: Vacuum vs photonic crystal

As announced in the beginning of this section, I will now compare some aspects of electromagnetics in vacuum and in photonic crystals: In general, the phase velocity, group velocity and density of states are properties which in vacuum can be deduced from the dispersion relation and which are (fundamentally) different in a photonic crystal. First of all, it does not make sense to ascribe a phase velocity to Blochwaves propagating in a photonic crystal, except in the first band. Secondly, the group velocity is a well-defined quantity which can be deduced from the band structure. It can be tailored by a proper choice of geometry and permittivity.

[2] a_{fcc} and the distance a between two rods in the same layer are often confused. In fact, a is the length of basis vectors spanning the primitive unit cell of the fcc-lattice. In this work I will always refer to the distance of two rods in the same layer as a, as indicated in Figure 2.1. For an fcc-woodpile $a_{\mathrm{fcc}} = \sqrt{2}a$.

[3] In fact, the absolute position of these points is not important. What is important is the relative position of the two rods and the orientation with respect to the basis-vectors.

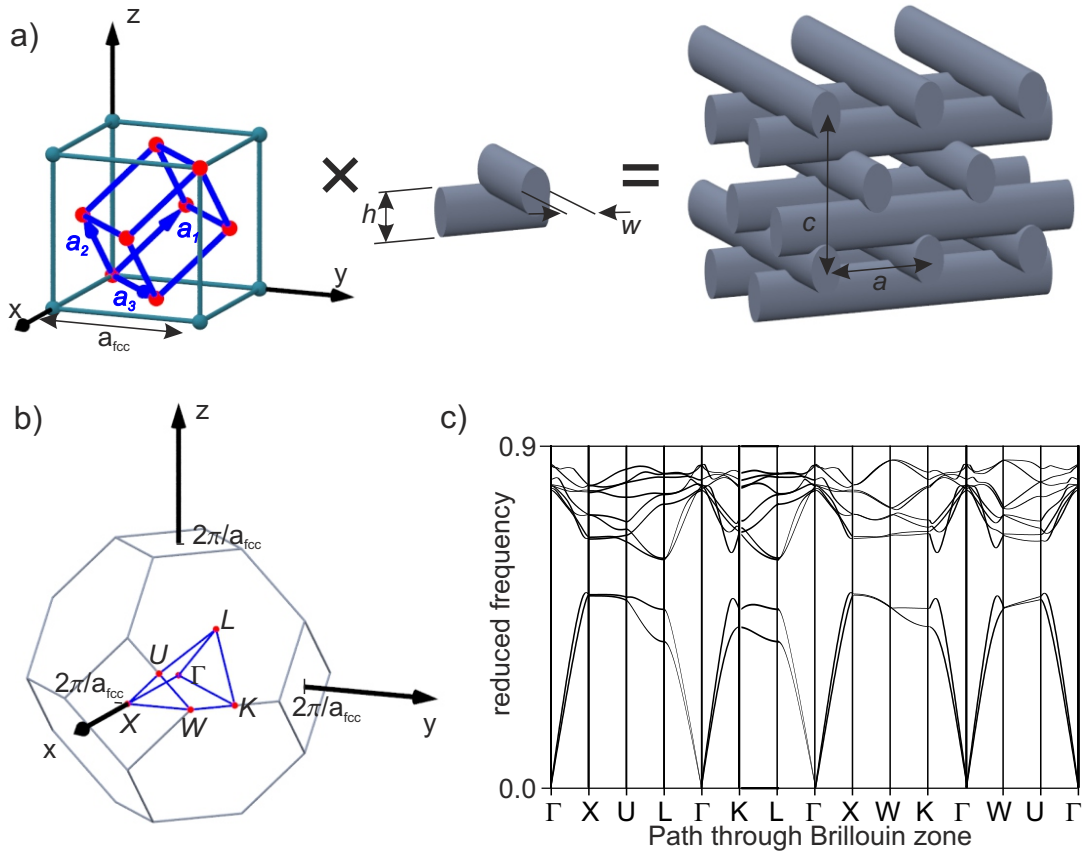

Figure 2.1: Woodpile photonic crystal. Panel a) shows the fcc-lattice together with the three basis-vectors $\boldsymbol{a}_{1,\mathrm{fcc}}$, $\boldsymbol{a}_{2,\mathrm{fcc}}$ and $\boldsymbol{a}_{3,\mathrm{fcc}}$ on the left. By placing the motif of two rods shown in the middle on every point of this lattice results in the woodpile photonic crystal depicted on the right. For elliptical rods it is completely characterized by the rodwidth w, the rod-height h, the rod-distance a, and the permittivities of the rods and that of the background-material. For an fcc-lattice, the lateral and axial lattice constants a_{fcc} and c are equal and of magnitude $\sqrt{2}a$. b) The Brillouinzone belonging to this photonic crystal. Γ, X, W, L, U, and K are the high symmetry points lying in the irreducible Brillouin zone. c) Part of the band structure of the photonic crystal in a) assuming that the rods are made of silicon and that the background material is air. The reduced frequency is connected to the real frequency is given in units of $\omega a/(2\pi c)$

Another important property of an electromagnetic field is the photonic density of states. It shows up in Fermi's golden rule that gives the decay rate $r_{j\to i}$ of an excited

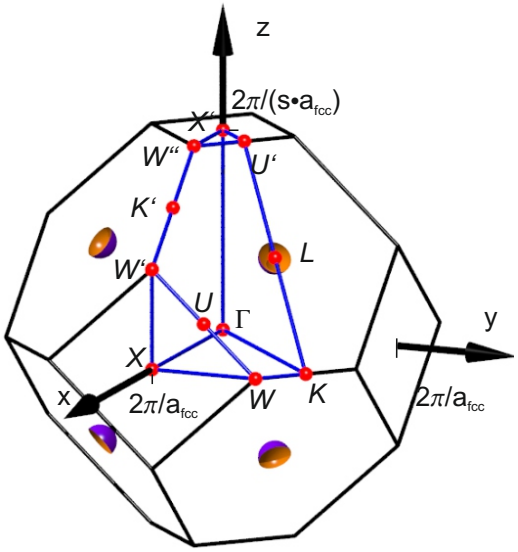

Figure 2.2: The irreducible Brillouin zone of the centered tetragonal lattice and its high-symmetry points, marked in red. Four of the eight parts of a possible isofrequency curve are shown as well in purple and orange. The colors serve for clarity only.

state j to a lower-energy state i:

$$r_{j\to i} = \frac{2\pi}{\hbar}\rho(\hbar\omega_{ji}) \cdot |p_{ij}|^2 \tag{2.12}$$

Here, p_{ij} is the matrix-element of the operator driving the decay (usually the dipole-operator) between the states i and j. Considering an excited atom, decaying radiatively, the density of states $\rho(\hbar\omega_{ji})$ is the product of the number of electronic states at the lower energy $\hbar\omega_i$ and the number $n(\hbar\omega_{ji})$ of photonic states that have an energy corresponding to the energy-difference between states j and i. If the transition couples to photons in vacuum, $n(\hbar\omega_{ji})$ can be deduced easily from the dispersion relation:

$$
\begin{aligned}
n(\omega_{\mathrm{ji}}) &= g \sum_{\boldsymbol{k}} \delta(\hbar\omega_{ji} - \hbar\omega(\boldsymbol{k})) && (2.13)\\
&= 2 \int \mathrm{d}^3\boldsymbol{k} \delta(\hbar\omega_{ji} - \hbar\omega(\boldsymbol{k})) && (2.14)\\
&= 2 \cdot 4\pi \int \mathrm{d}k\, k^2 \delta(\hbar\omega_{ji} - \hbar\omega(\boldsymbol{k})) && (2.15)\\
&= 2 \cdot 4\pi \int \mathrm{d}\omega\, \frac{\omega^2}{c_0^2} \frac{1}{|\boldsymbol{\nabla}_{\boldsymbol{k}}\, \omega(\boldsymbol{k})|} \delta(\omega_{ji} - \omega) && (2.16)\\
&= \frac{8\pi\omega^2}{c_0^3} && (2.17)
\end{aligned}
$$

The factor $g = 2$ that appears before the sum is introduced two account for the two possible polarisations of the photons with equal wavevectors. The term $\boldsymbol{\nabla}_{\boldsymbol{k}}\, \omega(\boldsymbol{k})$ denotes the derivative of ω with respect to $\boldsymbol{k}$. For electromagnetic waves in vacuum, this can easily be calculated from the dispersionrelation 2.10 as $\boldsymbol{\nabla}_{\boldsymbol{k}}\, \omega(\boldsymbol{k}) = c_0 \cdot \hat{k}$, where $\hat{k}$ is a unit-vector pointing in the direction of $\boldsymbol{k}$.

In a photonic crystal, $\omega = c_0 \cdot |\boldsymbol{k}|$ does not hold any more and a correct replacement for $\boldsymbol{k}$ to get from equation 2.15 to equation 2.16 that is independent of $\boldsymbol{k}$ is in the general case not possible anymore. Instead, it will have to be deduced "locally" from the band structure if desired. Also $\boldsymbol{\nabla}_{\boldsymbol{k}}\, \omega(\boldsymbol{k})$ has to be evaluated using the band structure. Furthermore, the degeneracy factor g should be set to unity since the sum now runs over all wavevectors and all bands. In particular, for photonic crystals with a sufficiently large contrast of permittivities and the right geometrical parameters, a situation can arise in which there exists a range of frequencies $[\omega_1, \omega_2]$ for which there are no solutions to equation 2.11. The photonic density of states will then be strictly zero in this frequency interval and the frequency range $[\omega_1, \omega_2]$ is then called a complete photonic bandgap. Light with frequencies inside the bandgap cannot be transmitted through such a photonic crystal, as a plane wave impinging onto it from the outside will not be able to couple to any propagating modes in the crystal. Given that the photonic crystal is non-absorbing, energy conservation then necessitates a total reflection of the incident light. Also, an emitter whose frequency of emission lies inside or at the edge of a photonic band will not emit or will do so in a strongly modified fashion, as discussed in [14, 21, 22] and demonstrated in References [23–27]. These authors investigate effects connected to the decay rate. One should expect another effect of a photonic bandgap environment on the emission process of an emitter: It is perfectly conceivable that the band structure has only few allowed states at certain frequencies, that might correspond to very few wave-vectors only. Actually, as the following short argument will show, such a situation necessarily arises: We know that band extrema necessarily occur at the Γ, L, and X-point. The L- and X-point lie on the surface of the Brillouin zone and for these points all eigenfrequencies are necessarily either all smaller or all larger than those in their environment, meaning that none of the neighbors of the L- and X-point are part of the isofrequency surfaces

$\omega(\boldsymbol{k}) = \omega_n(\boldsymbol{k}_\mathrm{L})$ and $\omega(\boldsymbol{k}) = \omega_n(\boldsymbol{k}_\mathrm{X})$, respectively. Hence, the isofrequency curves $\omega(\boldsymbol{k}) = \omega_n(\boldsymbol{k}_\mathrm{L})$ and $\omega(\boldsymbol{k}) = \omega_n(\boldsymbol{k}_\mathrm{X})$ necessarily have a gap around the points X and L. We then expect a non-isotropic emission from emitters emitting at these frequencies at least along the directions corresponding to $\boldsymbol{k}_\mathrm{L}$ and $\boldsymbol{k}_\mathrm{X}$. This is illustrated in Figure 2.2 for the case that the minimum of the third band delimits a complete photonic bandgap. This is the case for the photonic bandgaps presented later in this chapter. What is shown is a schematic isofrequency surface for a frequency slightly above the minimum of the third band. The outside and the inside of the surfaces are shown in purple and orange, for reasons of clarity. Also, only those isofrequency surfaces near those boundaries of the Brillouin zone that are visible in this perspective are shown. As one can see, only few wavevectors are covered by this isofrequency surface and correspondingly one should expect directional emission from emitters inside photonic crystals at this frequency. For the frequency at the band extremum at the L-point, the isofrequency curve is only a point, resulting in extremely directional emission at these frequencies.

Effects linked to this have been investigated with two-dimensional photonic crystals [28] and in opal photonic crystals. [29, 30]. Opal and opal-derived photonic crystals usually contain a lot of defects and consist of polycristalline domains. This will lead to an averaging of the directional features of the emission if one examins the whole crystal and is not singling-out one domain. With the approach we employed and describe in Chapter 5, we are able to produce mono-crystalline samples. In addition, none of the systems in the above references had a complete, three-dimensional bandgap, however, in which this effect is expected to be very pronounced as outlined above. [31]

Complete photonic bandgaps have been realized at microwave and infrared wavelengths [3,15,32–43], but have proven elusive in the visible part of the electromagnetic spectrum. [44] This spectral range is of particular interest for two reasons: First, any application of photonic crystals that is related to human perception will necessarily have to work in the visible. Secondly, the technical tool box for optical experiments is a lot more evolved for visible light than for light of longer wavelengths, with excellent single-photon-detectors and light-sources readily available. For example, the experiments on directional emission shown in Chapter 6 were greatly facilitated by the possiblity to use a nitrogen-cooled silicon CCD. In this thesis I therefore pursued the goal of making a photonic crystal with a complete photonic bandgap at visible frequencies.

2.2.2 Scaling properties

I will now take a look at some properties of the eigenvalue problem stated in equation 2.11. This will prove to be useful to illustrate the necessity of the steps undertaken in this thesis in order to construct a complete photonic bandgap in the visible:

Assume that we want to spatially shrink (or expand) a photonic crystal by some scaling factor $s < 1$ ($s > 1$). This means to replace the distribution of dielectric $\epsilon(\boldsymbol{r})$ by a different distribution $\epsilon'(\boldsymbol{r}) = \epsilon(\boldsymbol{r}/s)$. If we want to consider this as a change of variables form $\boldsymbol{r}$ to $\boldsymbol{r}'$ in equation 2.11 the necessary substitutions are:

- $\boldsymbol{\nabla} = s\boldsymbol{\nabla'}$
- $\boldsymbol{r} = \boldsymbol{r'}/s$

In particular, this means that $\epsilon'(\boldsymbol{r}\,') = \epsilon'(s \cdot \boldsymbol{r}) = \epsilon(\boldsymbol{r})$. Inserting all this yields:

$$\begin{aligned} s\boldsymbol{\nabla'} \times \left(\tfrac{1}{\epsilon(\boldsymbol{r'}/s)} s\boldsymbol{\nabla'} \times \boldsymbol{H}(\boldsymbol{r'}/s)\right) &= \tfrac{\omega^2}{c_0^2}\boldsymbol{H}(\boldsymbol{r'}/s) \\ \Leftrightarrow \qquad \boldsymbol{\nabla'} \times \left(\tfrac{1}{\epsilon'(\boldsymbol{r'})}\boldsymbol{\nabla'} \times \boldsymbol{H}(\boldsymbol{r'}/s)\right) &= \tfrac{\omega^2}{c_0^2 s^2}\boldsymbol{H}(\boldsymbol{r'}/s) \end{aligned} \tag{2.18}$$

Thus, a solution $\boldsymbol{H}(\boldsymbol{r})$ to equation 2.11 for the unscaled photonic crystal with an eigenfrequency ω also yields a solution $\boldsymbol{H'}$ for scaled versions of that photonic crystal with a new eigenfrequency $\omega' = \omega/s$ if we define $\boldsymbol{H'}$ as $\boldsymbol{H'}(\boldsymbol{r'}) = \boldsymbol{H}(\boldsymbol{r'}/s)$. In particular, this means that the scaled version of a photonic crystal having a complete photonic bandgap spanning from [ω_1,ω_2] will have an equally-sized bandgap spanning from [ω_1/s,ω_2/s]. Here, the size of the complete photonic bandgap is measured as the gap-to-midgap ratio defined as $2 \cdot \frac{\omega_2 - \omega_1}{\omega_2 + \omega_1}$. A first attempt at making a photonic bandgap at visible frequencies might therefore be to scale down the dimensions of the silicon-based photonic crystal with a complete photonic bandgap at telecom frequencies in Reference [45]. The geometric parameters of this crystal were optimised to have a bandgap at as high frequencies as possible under the fabrication constraints faced by the authors. Its upper bandedge is situated at a wavelength of 1550 nm, corresponding to a frequency of 193.5 THz and the rod-distance a is 566.3 nm. To bring only the upper band edge to 750 nm wavelength it would thus be necessary to bring the rod distance to $a' = 750/1550 \cdot a = 274$ nm. This is slightly beyond the reach of the nanofabrication techniques used in this thesis.[4]

The previous consideration of spatiallly scaling a photonic crystal was quite instructive. It told us that there is no fundamental length scale in a photonic crystal. This is actually not utterly surprising since Maxwell's equations are scale-invariant as long as ϵ and μ are scale-invariant. What about a fundamental scale for the permittivity, however? If we replace $\epsilon(\boldsymbol{r})$ according to $\epsilon'(\boldsymbol{r}) = \epsilon(\boldsymbol{r})/s^2$ in equation 2.11 we get

$$\boldsymbol{\nabla} \times \left(\frac{1}{\epsilon'(\boldsymbol{r})}\boldsymbol{\nabla} \times \boldsymbol{H}(\boldsymbol{r})\right) = \frac{s^2\omega^2}{c_0^2}\boldsymbol{H}(\boldsymbol{r}), \tag{2.19}$$

i.e., $\boldsymbol{H}(\boldsymbol{r})$ is a solution to 2.11 for both ϵ and ϵ'. The corresponding eigenfrequencies, however, increase with decreasing absolute values of the permittivity ϵ. Can we use this to simply scale a bandgap from telecom- to visible frequencies? The silicon woodpile in Reference [45] is composed of high-permittivity silicon-rods and low-permittivity air with permittivity $\epsilon_{\text{air}} = 1$. Since nonabsorbing materials with $0 < \epsilon < 1$ are not available, the answer is that we unfortunately cannot. However, the question of what would happen if we exchange silicon by a material with a lower permittivity arises. The operator $\hat{L}$ is linear and hermitian. It is therefore possible to apply perturbation theory [16, 46] to the eigenvalue problem 2.11 for small changes

[4] In addition to this, silicon is not a suitable material for photonic crystals in the visible spectrum as it is absorbing for light of wavelengths smaller than 1117 nm.

$\Delta\epsilon(\boldsymbol{r})$ to a given permittivity $\epsilon(\boldsymbol{r})$. The most convenient formulation for the change in frequencies in this case is, however, not in terms of $\boldsymbol{H}$ but in terms of $\boldsymbol{E}$. In this formulation the frequency shift $\Delta\omega_{n,\boldsymbol{k}}$ that the mode $\boldsymbol{H}_{n,\boldsymbol{k}}$ will undergo under the action of $\Delta\epsilon$ reads [16]

$$\Delta\omega_{n,\boldsymbol{k}} = -\frac{\omega_{n,\boldsymbol{k}}}{2}\frac{\int \mathrm{d}^3\boldsymbol{r}\Delta\epsilon(\boldsymbol{r})\left|\boldsymbol{E}_{n,\boldsymbol{k}}(\boldsymbol{r})\right|^2}{\int \mathrm{d}^3\boldsymbol{r}\epsilon(\boldsymbol{r})\left|\boldsymbol{E}_{n,\boldsymbol{k}}(\boldsymbol{r})\right|^2} + \mathcal{O}(\Delta\epsilon^2), \tag{2.20}$$

where $\boldsymbol{E}_{n,\boldsymbol{k}}$ is the electric field associated to the mode $\boldsymbol{H}_{n,\boldsymbol{k}}$. Hence, a small reduction of the permittivity of the woodpile rods will lead to an increase of the eigenfrequencies. For large changes in the permittivity of the rods, the field distributions $\boldsymbol{E}_{n,\boldsymbol{k}}$ will change as well but we expect that the trend holds. The chosen material for this thesis is titania because it has a high refractive index, can be deposited conformally on three-dimensional templates and is transparent in the entire visible spectrum. It has a permittivity of $\epsilon_{\text{titania}} = 6.2$ for light with a wavelength of $\lambda = 700\,\text{nm}$. The silicon rods in the aforementioned example were assumed to have a permittivity of $\epsilon_{\text{Silicon}} = 9.9$. If we gradually decrease the permittivity of the silicon rods towards the titania value, we see that the complete photonic bandgap shifts from the near-infrared towards the visible but decreases in size and eventually closes, cf. Figure 2.3a. As Figures 2.3c and d show, the band structure is not merely scaled but changes during this process. Differences can be seen easily for example along the $KW'U'$-section of the band structure and in the region of the complete photonic bandgap where the bands overlap partially for the low-permittivity woodpile. The bandgap corresponding to a different set of geometric parameters is also depicted in Figure 2.3a. For this set of parameters a complete photonic bandgap lying entirely in the visible can be achieved for sufficiently low (but high enough) permittivities, the banddiagramm of one such case is shown in Figure 2.3. How exactly one arrives at the final, close-to-optimal parameters for a big complete photonic bandgap is discussed in Chapter 5 once that the constraints imposed by the chosen fabrication method are clear.

2.3 Tailoring optical properties by subwavelength structure

In this section I will extend the description of light and matter as given in equations 2.1 to 2.4 by not taking ϵ as a parameter that is dictated by naturally available materials. I will outline the origin of ϵ in naturally occuring materials and show how this concept can be carried over to a level at which it is amenable to tailoring ϵ and thereby the optical properties of a material.

2.3.1 Interaction of electromagnetic fields with matter - from the microscopic picture to effective material parameters

With electromagnetic phenomena, one is usually interested in $\boldsymbol{E}$ and $\boldsymbol{B}$. How these fields interact with matter is determined by how they influence the atomic constituents. Classically, these are described by stating the positions $\boldsymbol{r}_i$, momenta $\boldsymbol{p}_i =$

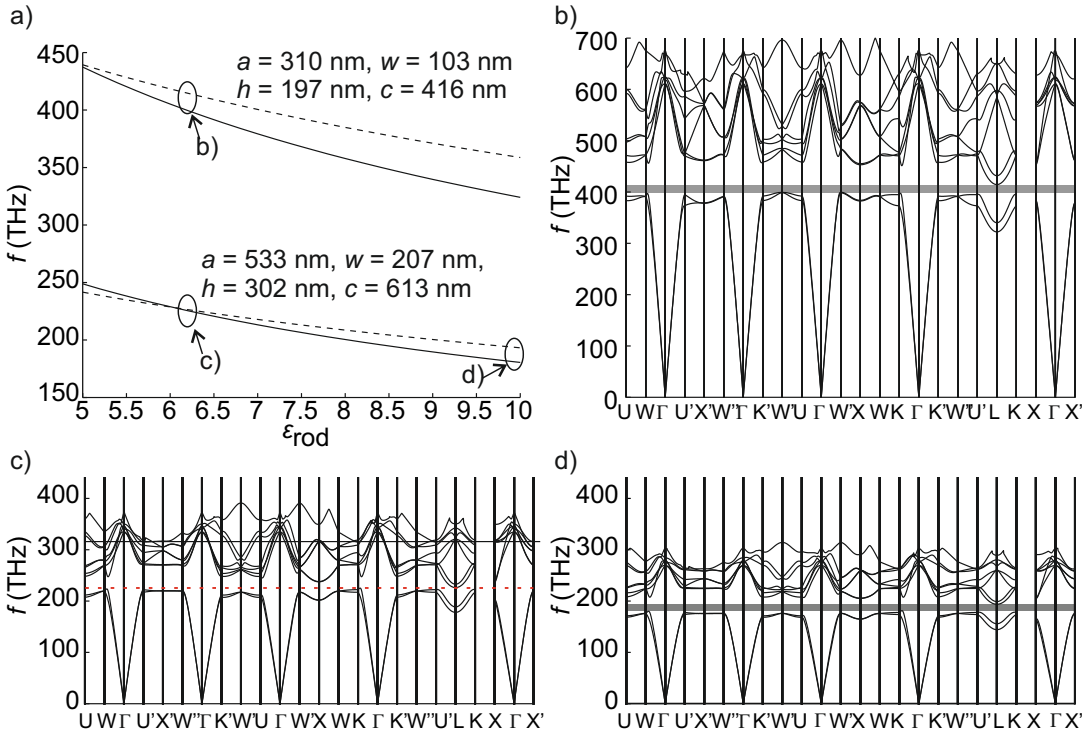

Figure 2.3: Effect of a variation of rod permittivites and geometry for two centered tetragonal woodpile photonic crystal. a) Positions of the maxima (solid lines) of the 2nd and the minima (dashed lines) of the third band for two different woodpile geometries as a function of the permittivity of the rod material. The band structures for some cases are shown in panels b) through d). b)band structure of a woodpile composed of titania-rods of permittivity $\epsilon_{\mathrm{rod}} = 6.2$. A complete photonic bandgap of 3.7% size exists and is lying entirely in the visible spectrum (above 400 THz). c) A titania woodpile with the geometrical parameters given in panel a. There is no complete photonic bandgap. The red line touches the maximum of the 2nd band in the ΓK and the ΓW-directions and the minimum of the third band at the L-point. d) For silicon rods with $\epsilon_{\mathrm{rod}} = 9.9$ the same geometry leads to a 6.9% complete photonic bandgap in the near-infrared. The gray areas in b) and d) highlight the region of the complete photonic bandgaps. For all band structures 9 bands are shown.

$m_i \boldsymbol{v}_i$ and charges q_i of the $i = 1, \ldots, N$ particles under consideration and the interparticle interactions. The interaction of these particles and electromagnetic fields is given by the Lorentz-force and interparticle forces

$$m\ddot{\boldsymbol{r}} = e\left(\boldsymbol{E}(\boldsymbol{r}) + \dot{\boldsymbol{r}} \times \boldsymbol{B}(\boldsymbol{r})\right) + \text{other forces}, \tag{2.21}$$

and the Maxwell equations in vacuum with free charge and current densities ρ and $\boldsymbol{j}$

$$\epsilon_0 \nabla \cdot \boldsymbol{E}(\boldsymbol{r}) = \rho(\boldsymbol{r}) \tag{2.22}$$

$$\nabla \cdot \boldsymbol{B}(\boldsymbol{r}) = 0 \tag{2.23}$$

$$\boldsymbol{\nabla} \times \boldsymbol{E}(\boldsymbol{r}) + \frac{\partial \boldsymbol{B}(\boldsymbol{r})}{\partial t} = 0 \tag{2.24}$$

$$\boldsymbol{\nabla} \times \boldsymbol{B}(\boldsymbol{r}) - \epsilon_0 \mu_0 \frac{\partial \boldsymbol{E}(\boldsymbol{r})}{\partial t} = \mu_0 \boldsymbol{j}(\boldsymbol{r}). \tag{2.25}$$

Here, ρ and $\boldsymbol{j}$ are meant to describe the precise, microscopic charge and current densities, *i.e.*:

$$\rho(\boldsymbol{r}) = \sum_{\mathrm{i}=1}^{N} q_{\mathrm{i}} \delta(\boldsymbol{r} - \boldsymbol{r}_{\mathrm{i}}) \tag{2.26}$$

$$\boldsymbol{j}(\boldsymbol{r}) = \sum_{\mathrm{i}=1}^{N} q_{\mathrm{i}} \boldsymbol{v}_{\mathrm{i}} \delta(\boldsymbol{r} - \boldsymbol{r}_{\mathrm{i}}) \tag{2.27}$$

Knowledge of these densities allows for the deduction of macroscopic properties such as the polarisation $\boldsymbol{P}$.
Usually a description in terms of N particles is neither of interest nor feasible. In these cases one takes recourse to a description using fields and densities which are averaged over volumina V that are small compared to the wavelength of the electromagnetic wave. This turns equations 2.23 and 2.24 into

$$\boldsymbol{\nabla} \cdot \langle \boldsymbol{B} \rangle_{\mathrm{V}} (\boldsymbol{r}, t) = 0 \tag{2.28}$$

$$\boldsymbol{\nabla} \times \langle \boldsymbol{E} \rangle_{\mathrm{V}} (\boldsymbol{r}, t) + \frac{\partial \langle \boldsymbol{B} \rangle_{\mathrm{V}} (\boldsymbol{r}, t)}{\partial t} = 0 \tag{2.29}$$

where $\langle A \rangle_{\mathrm{V}} (\boldsymbol{r}, t)$ indicates the spatial average of A over a volume V around the point $\boldsymbol{r}$. The two Maxwell equations containing ρ and $\boldsymbol{j}$ turn into:

$$\epsilon_0 \boldsymbol{\nabla} \cdot \langle \boldsymbol{E} \rangle_V (\boldsymbol{r}, t) = \langle \rho \rangle_V (\boldsymbol{r}, t) \tag{2.30}$$

$$\boldsymbol{\nabla} \times \langle \boldsymbol{B} \rangle_V (\boldsymbol{r}, t) - \epsilon_0 \mu_0 \frac{\partial \langle \boldsymbol{E} \rangle_V (\boldsymbol{r}, t)}{\partial t} = \mu_0 \langle \boldsymbol{j} \rangle_V (\boldsymbol{r}, t) \tag{2.31}$$

The average $\langle \rho \rangle$ which appears here is equivalent to a series expansion of ρ whose leading terms are the monopole-moment ρ_0 and the divergence of the polarisation:

$$\langle \rho \rangle_V (\boldsymbol{r}, t) = \rho_0 - \boldsymbol{\nabla} \cdot \langle \boldsymbol{P} \rangle_V + \ldots \tag{2.32}$$

Similarly, the average of $\boldsymbol{j}$ can be approximated by a contribution accounting for the macroscopic currents, the curl of the magnetic moment $\boldsymbol{M}$ and the time-derivative of the dipole moment:

$$\langle \boldsymbol{j} \rangle_V (\boldsymbol{r}, t) = \boldsymbol{j}_0 + \frac{\partial \langle \boldsymbol{P} \rangle_V}{\partial t} + \boldsymbol{\nabla} \times \langle \boldsymbol{M} \rangle_V + \ldots \tag{2.33}$$

Inserting these two approximations into equations 2.30 and 2.31 and rearranging we get:

$$\epsilon_0 \boldsymbol{\nabla} \cdot \langle \boldsymbol{E} + \boldsymbol{P} \rangle_V (\boldsymbol{r}, t) = \rho_0 \tag{2.34}$$

$$\boldsymbol{\nabla} \times \left\langle \frac{1}{\mu_0} \boldsymbol{B} - \boldsymbol{M} \right\rangle_V (\boldsymbol{r}, t) - \frac{\partial \langle \epsilon_0 \boldsymbol{E} + \boldsymbol{P} \rangle_V (\boldsymbol{r}, t)}{\partial t} = \boldsymbol{j}_0 \tag{2.35}$$

This is what prompts us to introduce the fields $\boldsymbol{H}$ and $\boldsymbol{D}$ *via* the constitutive relations 2.5 and 2.6 given at the beginning of this chapter. With these fields, the macroscopic Maxwell equations 2.1 to 2.4 result.

The important thing here for the remainder of this chapter is that the polarisation on a sub-wavelength scale that an electric field induces in a material is what determines its effective permittivity ϵ. By tailoring the polarizability of a material, one is thus tailoring its permittivity. This is the avenue towards tailored optical materials that is exploited in the field of metamaterials [12, 47]. (The same holds true for the permeability μ, but since I have not tried to influence this property in this thesis, I will not consider it further). Here, the polarizability is changed, for example by building materials composed of resonant elements (such as the ubiquitous Split-Ring resonator [5, 48], metal helices [49], or fishnet materials [50, 51]) or by tailoring the volume fraction of one material in a mixture (such as a mixture of polymer and air, for example a photonic crystal operated in the long-wavelength limit [52] or a sequence of layers [53, 54]).

In what follows, I will first show that the density of free electrons is an important optical parameter in Subsection 2.3.2 and proceed to demonstrate that this parameter is amenable to use in rational design. For this, I will outline two ways in which this parameter can be used for the construction of tailored optical materials. The first example in Subsection 2.3.3 relies on a graded profile of the permittivity. For the second exmaple in Subsection 2.3.4, I will outline how the effective permittivity of a layered system depends on the permittivites of the constituent materials. Using these two examples I will illustrate the particular benefits that my approach to tailoring the effective permittivity has over other methods.

2.3.2 Drude metals

In order to go from the general considerations about the polarisation in the previous section to a concrete example and application relevant for this thesis, I will now derive the permittivity of a free electron gas.

For this, I will consider the response of a single electron that is free to move under the influence of an electric field and subject to damping that is proportional to its velocity. These assumptions are the basis of Drude's theory for the free electron gas.

The equation of motion of such an electron with mass m_e and charge $-e$ under the influence of a harmonic electric field oscillating with a frequency ω is:

$$m_e\ddot{\boldsymbol{r}} + m_e\gamma\dot{\boldsymbol{r}} = -e\boldsymbol{E}_0 e^{-\mathrm{i}\omega t} \tag{2.36}$$

Here m_e is the electron mass, γ is a damping constant and $\boldsymbol{E}_0$ is the polarisation and amplitude of the electric field. This equation is solved by $\boldsymbol{r} = \boldsymbol{r}_0(\omega)e^{-\mathrm{i}\omega t}$ with a frequency-dependent amplitude

$$\boldsymbol{r}_0(\omega) = \frac{e\boldsymbol{E_0}}{m_e}\frac{1}{\omega^2 + i\omega\gamma}. \tag{2.37}$$

This oscillation of the electron has a dipole-moment

$$\boldsymbol{p} = -e\boldsymbol{r}_0(\omega). \tag{2.38}$$

In a gas of free electrons with n electrons per unit volume, a polarisation $\boldsymbol{P} = n\boldsymbol{p}$ will thus build up. Inserting this into the constitutive relation for $\boldsymbol{D}$ we get:

$$\boldsymbol{D} = \epsilon_0\boldsymbol{E}_0 e^{\mathrm{i}\omega t} + \boldsymbol{P} = \epsilon_0\left(1 - \frac{ne^2}{m_e\epsilon_0}\frac{1}{\omega^2 + \mathrm{i}\omega\gamma}\right)\boldsymbol{E}_0 e^{\mathrm{i}\omega t}. \tag{2.39}$$

Introducing the plasma frequency as $\omega_{\mathrm{Pl}}^2 = \frac{ne^2}{m\epsilon_0}$ and identifying the term in brackets as ϵ (as outlined above) we get the permittivity of the free electron gas, as known from Drude theory:

$$\epsilon(\omega) = 1 - \frac{\omega_{\mathrm{Pl}}^2}{\omega^2 + \gamma^2} + \mathrm{i}\frac{\gamma}{\omega}\frac{\omega_{\mathrm{Pl}}^2}{\omega^2 + \gamma^2} \tag{2.40}$$

In a semiconductor, n and therefore the plasma frequency can be controlled by intentionally doping the semiconductor, for example by the introduction of impurity atoms. If chosen properly, these impurity atoms contribute an unbound electron that can be thought of as quasifree but having an effective mass m_e^* instead of the mass of the free electron. In this thesis, zinc oxide (ZnO) was used as the semiconductor and aluminum as well as titanium were used as dopants. For this case the permittivity of the doped ZnO is not solely determined by the contribution of the free electrons, however. The ZnO contributes an additional nearly frequency-independent polarisation response that can be accounted for by modifying the Drude formula for the free electron gas to:

$$\epsilon_{\mathrm{ZnO}}(\omega) = \epsilon_\infty - \frac{\omega_{\mathrm{Pl}}^2}{\omega^2 + \gamma^2} + \mathrm{i}\frac{\gamma}{\omega}\frac{\omega_{\mathrm{Pl}}^2}{\omega^2 + \gamma^2} \tag{2.41}$$

For ZnO, ϵ_∞ is of the order of four.

Figure 2.4 shows the degree to which we can expect the permittivity of doped ZnO to be tailorable.

As a rule of thumb, $\mathrm{Re}(\epsilon)$ will become negative for frequencies smaller than $\omega_{\mathrm{zerocrossing}} \approx \omega_{\mathrm{Pl}}/\sqrt{\epsilon_\infty}$. The damping frequency slightly shifts this value. We also note that for low

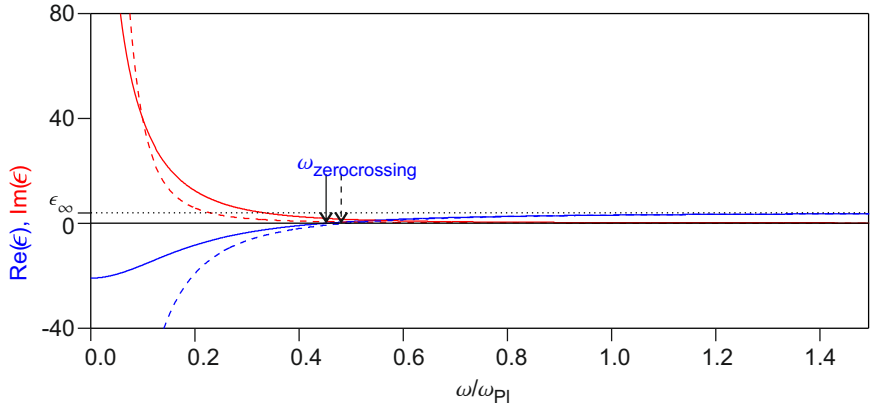

Figure 2.4: Complex permittivity of a Drude metal for two cases: $\gamma/\omega_{\mathrm{Pl}} = 0.2$ (solid lines) and $\gamma/\omega_{\mathrm{Pl}} = 0.05$ (dashed lines). The frequencies $\omega_{\mathrm{zerocrossing}}$ at which $\mathrm{Re}(\epsilon) = 0$ are indicated for the two cases as well by the solid and dashed arrows for $\gamma/\omega_{\mathrm{Pl}} = 0.2$ and $\gamma/\omega_{\mathrm{Pl}} = 0.05$, respectively.

frequencies at which

$$\frac{\omega_{\mathrm{Pl}}^2}{\omega^2 + \gamma^2} \gg \epsilon_\infty \tag{2.42}$$

holds, the ratio of the imaginary and the real part of the permittivity is approximately γ/ω. So the operating frequencies of doped ZnO based materials should lie between γ and $\omega_{\mathrm{Pl}}/2$ and the question arises what kind of damping frequency we have to expect for doped ZnO. Boltasseva *et al.* have recently systematically screened various materials for this property and have suggested that doped ZnO might have a low damping corresponding to $\gamma = 2\pi \cdot 30\,\mathrm{THz}$. [55–57] To estimate the order of the probably achievable plasma frequency we can use $n = 10^{21}\mathrm{cm}^{-3}$ (a value commonly used for highly doped silicon) and use the mass of the free electron instead of the effective mass, which gives us a maximum plasma frequency $\omega_{\mathrm{Pl,max}} = 2\pi \cdot 285\,\mathrm{THz}$. We therefore expect to be able to use doped ZnO as a good tailored metal between 30 THz and 142 THz, corresponding to wavelength between 10 µm and 2.1 µm.

I used atomic layer deposition (ALD) to deposit this material. Details of the method and the variation of permittivity that can be obtained with it will be discussed in Chapter 4. For the remainder of this chapter it is necessary to know however, that tailor-doped layers with thickness as small as a few nm can be deposited this way. It is also straightforwardly possible to integrate layers of different doping or dielectric layers into the deposition-procedure.

It seems somewhat obvious that having such a tailored material at hand relaxes design constraints for all kinds of devices. However, the following two examples will illustrate the benefits that arise from the availability of such a material. Also, a material with permittivity of choice is desired for many applications in transformation optics [12, 58, 59] or as an epsilon-near-zero material. [60].

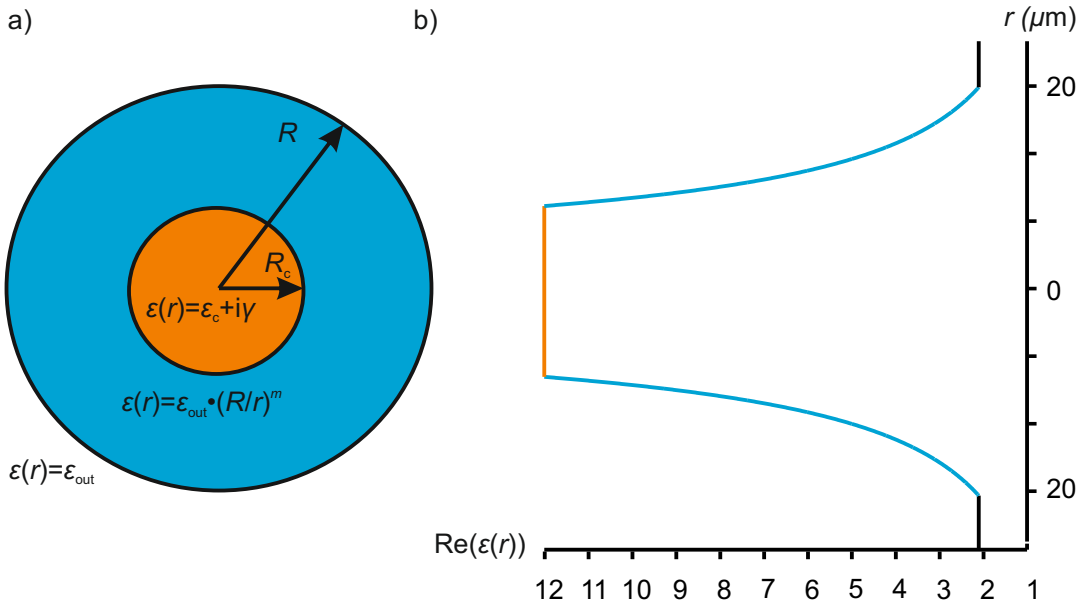

Figure 2.5: a) Sketch of the device proposed in Reference [61]. b) One hypothetical realisation discussed in the same reference. It consists of a doped silicon core (orange) and a shell (blue). The shell is made up of a tailored material with a permittivity varying as indicated for $m = 2$ and it is embedded in silica with a permittivity $\epsilon_{\text{out}} = 2.1$. For these parameters the structure absorbs nearly all light that is incident on it.

2.3.3 Metamaterial perfect absorber

To give an example for the usefulness of a tailored material, I will now consider the device depicted in Figure 2.5a. It is discussed in Reference [61]. It has a shell of radius R with a radially decreasing permittivity $\epsilon(r)$ as depicted in Figure 2.5b and an absorbing core of radius R_{c} with a permittivity $\epsilon_{\text{c}}+\text{i}\gamma$. It is embedded in a dielectric environment with a permittivity ϵ_{out}. Such a structure can be designed to increase the absorption cross section of the absorber in its center to the geometric cross-section of the entire device, which can be utilized in structures that aim at collecting incident electromagnetic energy, for example.

It is shown in Reference [61] that for permittivities of the shell varying as

$$\epsilon(r) = \epsilon_{\text{out}} \left(\frac{R}{R_{\text{c}}} \right)^m \tag{2.43}$$

where $m \geq 2$ nearly all light that is incident onto the structure is absorbed if R_{c} is chosen as $R_{\text{c}} = \sqrt{\epsilon_{\text{out}}/\epsilon_{\text{c}}} R$.

It is evident, that a multitude of materials will be necessary in order to fabricate this device unless one can gradually vary the permittivity of one material. Exactly this is

possible if one uses ALD to grow the material as the scale at which one can vary the material composition can be as small as a few nanometres.

2.3.4 Hyperbolic metamaterials

The metamaterial absorber which I just discussed consists of an inhomogeneous but locally isotropic material. As I will show in the following chapters, it is easily possible to deposit layers of different materials onto each other with ALD, even with thicknesses of a few nanometres only. An alternating stack of two different materials is expected to result in an effectively anisotropic medium if the layers are sufficiently small compared to the wavelength. This is exploited, for example, in hyperbolic metamaterials [53, 62–65]. These metamaterials have a uniaxial permittivity with at least one negative entry in the permittivity tensor $\epsilon = \mathrm{diag}(\epsilon_{\mathrm{xx}}, \epsilon_{\mathrm{xx}}, \epsilon_{\mathrm{zz}})$ with $\epsilon_{\mathrm{xx}} \cdot \epsilon_{\mathrm{zz}} < 0$, *i.e.*, they are a dielectric in one or two directions, and metallic in the remaining directions. The dispersion relation for light propagating in such a material is [64]:

$$\frac{k_x^2 + k_y^2}{\epsilon_{zz}} - \frac{k_z^2}{\epsilon_{xx}} = \frac{\omega^2}{c_0^2} \tag{2.44}$$

Isofrequency curves for waves propagating in such a material are hyperbolas – thus the name hyperbolic metamaterials (HMM). What is tempting about a material with such a dispersion relation is that for any given frequency, wavevectors of arbitrary magnitude exist. This can result in an increased photon density of states and the ability to transport information about arbitrarily high spatial frequencies.[5] The dependence of the effective permittivity of the stack shown in Figure 2.6a on the permittivity of its constituents is [53, 66, 67]:

$$\frac{1}{\epsilon_{\mathrm{zz}}} = \frac{f}{\epsilon_{\mathrm{A}}} + \frac{1-f}{\epsilon_{\mathrm{B}}} \tag{2.45}$$

$$\epsilon_{\mathrm{xx}} = \epsilon_{\mathrm{yy}} = f\epsilon_{\mathrm{A}} + (1-f)\epsilon_{\mathrm{B}} \tag{2.46}$$

Here, ϵ_{A} is the permittivity of material A, ϵ_{B} is the permittivity of material B and f is the filling fraction of material A as given by $f = d_{\mathrm{A}}/(d_{\mathrm{A}} + d_{\mathrm{B}})$. Furthermore, d_{A} and d_{B} are the thicknesses of the layers of materials A and B, respectively, and z is assumed to be the stacking direction. A distinction between two classes of hyperbolic metamaterials can be made. Depending on whether there is one or two negative entries in ϵ one talks about type-I and type-II hyperbolic metamaterials, respectively (sometimes also refered to as transverse positive and transverse negative). Looking at equations 2.45 and 2.46 we see that one constituent material with negative permittivity and one with positive permittivity is required in both cases. For applications aiming at utilising the ability to excite arbitrarily high wavevectors, the type-I effective material is required. In order for ϵ_{xx} to be positive, it is necessary to balance the filling fractions

[5] However, the validity of equation 2.44 is limited to wavevectors that are not able to resolve the individual layers, *i.e.* to $|\boldsymbol{k}| << \pi/\min(d_A, d_B)$. For wavevectors of larger magnitude the effective medium approximation cannot hold.

of the negative and positive permittivity constituents. It is always possible to fulfill this necessary condition by choosing an appropriate filling factor f. I will now briefly consider the case that the negative-permittivity component is one of the "commonly" used noble metals such as gold or silver. Silver has a plasma frequency of $2\pi{\cdot}2179\,\mathrm{THz}$. From this, a large but negative permittivity on the order of -100 results for light of a free-space wavelength of 1300 nm (corresponding to a frequency of 231 THz). This will need to be balanced by the positive-permittivity constituent which can be chosen from the the selection of available dielectrics. Silicon is a high-refractive index material that is transparent at 1300 nm and has a permittivity of about 12.2 (corresponding to a refractive index of 3.49). This results in a silver filling fraction of $f \leq 0.108$. In order for the effective medium approximation to hold, a single silicon layer, a single silver layer and the entire unit cell of the metamaterial have to be of subwavelength-size. If we, loosely, require the silicon-layer to be less than a quarter-wavelength thick, we arrive at a silicon thickness of $d_{\mathrm{Si}} \leq 0.25 \cdot 1300\mathrm{nm}/3.49 = 93.1\,\mathrm{nm}$ which implies a silver thickness of less than $d_{\mathrm{Ag}} \leq f/(1-f) \cdot d_{\mathrm{Si}} = 10\,\mathrm{nm}$. This is maybe possible, but will surely be challenging to deposit. Also, this filling factor does not lead to a type-I hyperbolic metamaterial since $\epsilon_{zz} = 13.88$ for this filling fraction. A tailored-permittivity material such as doped Zincoxide would allow for working with larger filling factors and/or the usage of smaller-permittivity dielectrics. The preceeding back-of-the-envelope calculation is systematically depicted in Figure 2.6 for silver and a Drude metal with a plasma frequency of $2\pi{\cdot}300\,\mathrm{THz}$. We expect to work in the infrared if we employ doped zinc oxide. In the plots, I have therefore omitted the visible wavelength range in which it is possible to construct type-I hyperbolic metamaterials using thin silver layers. [54, 62]

As we can see, there are indeed three benefits to having a tailored metal with a moderately negative permittivity at hand: First of all we notice that it is not possible at all to engineer a type-I hyperbolic metamaterial at the wavelengths shown using silver and even a high permittivity dielectric such as silicon. However, this is the case for the tailored metal. Secondly, by comparing the red and green areas in panels c) and d) we see that using the tailored metal we have the ability to choose the wavelengths at which the material behaves as a type-I hyperbolic metamaterial by a proper choice of dielectric. Thirdly, we can get the type-I behaviours over a wide wavelength range for moderate metal filling fractions. Additionally, as I will show in the following two chapters, it is possible to grow even very thin films of doped ZnO easily by ALD.

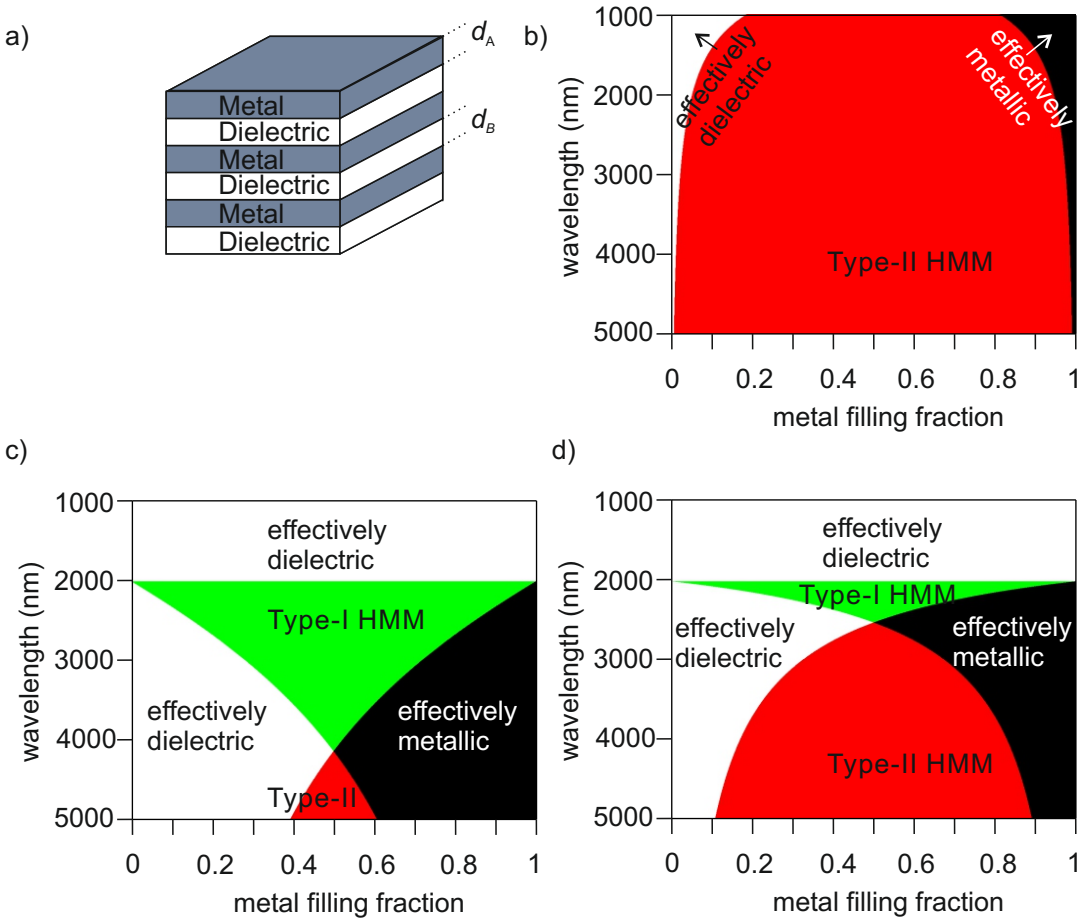

Figure 2.6: Hyperbolic metamaterials (HMM) a) Sketch of one possible realisation of a hyperbolic metamaterial. A hyperbolic dispersion of type-I or type-II results only if the filling fraction and permittivities of the dielectric and metal are chosen correctly, as seen in the phase diagrams shown in b-d. b) Phase diagramms for silver and a dielectric with permittivity 12.2, corresponding to silicon, c) the same dielectric and a drude metal with a plasma frequency $\omega_{\mathrm{Pl}} = 2\pi \cdot 300\,\mathrm{THz}$, a damping frequency $\gamma = 2\pi \cdot 20\,\mathrm{THz}$ and a background permittivity $\epsilon_{\mathrm{inf}} = 4$, and d) the same drude metal and a dielectric with a permittivity of 2.25, corresponding roughly to SiO_2.

3 Template assisted atomic layer deposition

As we have seen in the preceding chapter, photonic crystals with a complete photonic bandgap and metamaterials are interesting artificial optical materials that derive their unusual optical properties from a tailored arrangement of a material with a specific permittivity in three dimensions. In this chapter I will present the basics of atomic layer deposition, a coating technique that is – as we will see – extremely well suited for working with three-dimensional samples, and present the basic coating processes that were utilized to obtain the results shown in this thesis. Before this, I will outline how stimulated-emission depletion inspired direct laser writing (STED-DLW) can provide templates that define an almost arbitrary three-dimensional geometry with feature sizes approaching 100 nm.

3.1 Templates by stimulated-emission depletion inspired direct laser writing

The setup used for STED-DLW in this thesis was built and operated by Dr. Joachim Fischer. Here, a pulsed laser beam with a wavelength of 800 nm is focused *via* a microscope objective into a sample of photoresist composed of a monomer and a photoinitiator. This laser is referred to as the writing laser. The photoinitiator contained in the resist is transparent at 800 nm but does show absorption at 400 nm, such that in the volume of the laser focus absorption can occur *via* a two-photon process. The thus-excited photoinitiator molecules trigger a local polymerisation reaction. For sufficiently high exposure doses (where the dose is the product of squared laser intensity and exposure time), this polymerisation reaction leaves a solid piece of polymer behind that is insoluble in the monomer and also in isopropanol. Thus, after exposure, the unpolymerized photoresist can be washed away, leaving only the polymerized material behind.

The volume inside of which the reaction takes place is determined by the shape of the writing-laser focus and is called a voxel in analogy to the picture element pixel. If one now scans the sample across the writing-laser's focus, one can define a three-dimensional geometry of polymerized material whose smallest feature sizes are given by the shape of the voxel. This method is called direct laser writing (DLW) and the steps just outlined are depicted schematically in Figure 3.1. It has been developed originally by Maruo *et al.* [8] and has since become a well-established technology for three-dimensional structuring on the micro- to nanoscale.

The sample can be moved with respect to the focus of the writing laser with very high precision, for example if it is mounted to a stage driven by piezo-actuators. The precision with which the stage can be moved limits the precision with which structures can be defined in DLW. However, there is no guarantee for a direct correspondence between the trajectory of the sample and the geometry of the developed, polymerized material. This is due to shrinkage which the polymer undergoes upon development. This can be compensated during the writing process by choosing a properly pre-stretched geometry for the polymer structure to be written. But the amount of shrinkage depends sensitively on the exposure dose and the geometry of the structure being written, so there is no general recipe for the compensation of shrinkage.

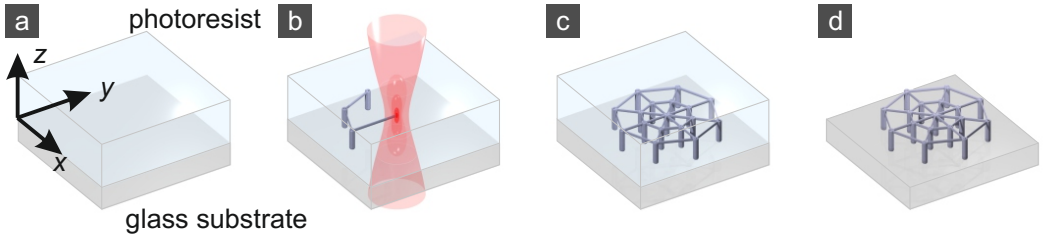

Figure 3.1: The essential steps of a direct laser writing process. a) The fabrication starts with a glass substrate with photoresist on it. The essential ingredients of the resist are a monomer and a photoinitiator. b) The sample is scanned across the focus of a laser. In the focus, two-photon absorption by the photoinitiator triggers a polymerisation reaction of the monomers that leads to a local solidification the resist. c, d) At the end, the unpolymerized resist is washed away in a developer that does not solve or attack the solidified resist. This way, freestanding polymer structures can be obtained. Image adapted from Reference [68].

The mechanism underlying the polymerisation in DLW is the photoactivation of the photoinitiator molecule. The capability to produce three-dimensional structures is attained by performing this activation *exclusively* in a several-photon-process for which there is sufficient intensity only in the voxel. This way it is possible to focus the laser through the photoresist without exposing it along the path of the light to the foucs. This imposes constraints on the combination of photoresists and lasers that can be used. In our case, we use a photoresist that is polymerized by two-photon absorption of photons in the focus of a pulsed 800 nm laser beam. The intensity distribution in the voxel is given by the optics used to create the laser focus and the wavelength. Thus, there is a fundamental limit to the lateral resolution Δx, *i.e.*, to the minimum seperation of two features in the x-y-plane (see Figure 3.1) that can be produced by DLW. [10, 69] There is also a fundamental lower limit to the seperation Δz of two features along the optical axis z. For the lateral case this is the Abbe

criterion for two-photon absorption

$$\Delta x = \frac{\lambda}{2\sqrt{2}\mathrm{NA}} = 202\,\mathrm{nm} \tag{3.1}$$

$$\Delta z = \frac{\lambda \cdot \mathrm{AR}}{2\sqrt{2}\mathrm{NA}} = 505\,\mathrm{nm} \quad , \tag{3.2}$$

where NA is the numerical aperture of the microscope objective used to focus the laser into the photoresist. AR is the aspect ratio of the focus produced by the exposing laser. In our case the numerical aperture is 1.4 and the aspect ratio is 2.5, resulting in the value quoted above.

The shortest distance of two non-touching rods in the axial direction for a woodpile is $3/4^{\mathrm{th}}$ of the axial lattice constant. From Chapter 2 we know that we will need to produce woodpiles with a rod distance a of 310 nm derived from a centered-tetragonal lattice that is compressed with respect to the fcc-lattice by about 10%. The minimum resolution we need for this is then $\Delta z_{\mathrm{min}} = 0.75 \cdot a_{\mathrm{fcc}} \cdot 0.9 = 295\,\mathrm{nm} < \Delta z = 505\,\mathrm{nm}$. Therefore, conventional DLW at 800 nm wavelength does not allow for producing woodpiles with a sufficiently small resolution. A way to improve the resolution of DLW is stimulated-emission depletion DLW (STED-DLW). In this approach to direct laser writing a photodeactivation of the photoinitiator molecules is introduced. I will now briefly outline the concept of STED-DLW employed in this thesis:

If one combines the two-photon activation of the photoinitiator with a photodeactivation it should be possible to switch off the polymerisation reaction selectively at those places where the resist is illuminated by the deactivating laser. This is done in stimulated-emission depletion microscopy where dyes are excited by one laser and simultaneously depleted with a depletion laser with both lasers being focused at the same spot. The latter beam has, however, passed a phase mask. This phase mask changes its intensity profile in such a way that it forms a focus in which there is sufficient intensity to suppress the dye's emission in all places except in the center of the spot. Here, there is zero intensity of the depletion-laser. Loosely speaking, the result is a net excitation of the dye molecules only in the region corresponding to the difference of the excitation and the depletion laser's foci, resulting in a resolution beyond the diffraction limit.

Transferring this technique from high-resolution microscopy [70] to DLW, it is possible to overcome the limits to the resolution mentioned above. [10, 52, 71] To do this, a second laser — the depletion laser — which has a wavelength of 532 nm is focused onto the same spot through the same microscope objective. However, as above, this laser beam passes a phase mask that changes its phase profile before it enters the objective. The resulting focus then has a different shape, depending on the design of the phase mask. Notably, it has zero intensity at the center of the writing laser's focus. The situation is depicted in Figure 3.1a for the particular phase mask used in this thesis. [72] The effect of the depletion laser is to locally switch off the polymerisation reaction in the volume of high depletion laser intensity. Thus, while both foci are diffraction-limited, the effectively polymerized volume of photoresist is of

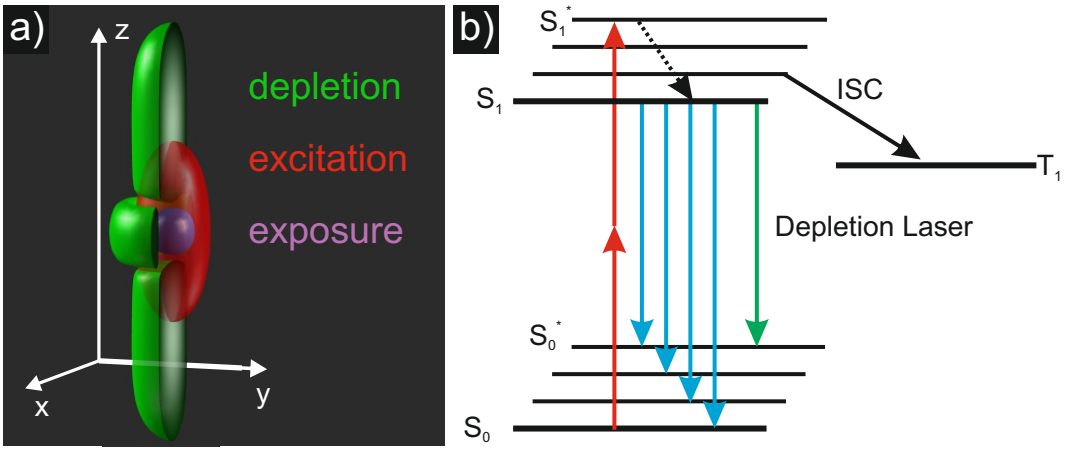

Figure 3.2: Working principle of stimulated emission depletion DLW (STED-DLW). a) Sketch of the different foci and the effectively exposed volume. b) Jablonski diagram of the processes occuring in STED-DLW. In the focus of a pulsed laser with 800 nm wavelength (red in a)), photoinitiator molecules are excited to the first singlett state *via* a two-photon process (red arrows in b)). If left to themselves, they would either initiate a local polymerisation of the photoresist after having undergone an inter-system crossing (ISC) process (black, solid arrow) or would decay back to the ground state by emitting a fluorescence photon (blue arrows). With these processes it is possible to perform direct laser writing. In STED-DLW, a second laser (green in a)) is used to suppress ISC locally by forcing the excited photoinitiator molecules to undergo stimulated emission. At the core of STED-DLW is the ability to shape the foci of the red and green lasers. Image a) courtesy of Joachim Fischer. Image b) adapted from Reference [10].

sub-diffraction-limited size. As one can see in Figure 3.1a, the size of the effectively exposed volume is reduced both in the lateral and in the axial direction. With this technique it is possible to create polymer templates with the necessary resolution for a woodpile photonic crystal with a complete photonic bandgap (after double-inversion into titania, as outlined in Chapter 5).

3.2 Atomic layer deposition

3.2.1 The concept of atomic layer deposition

The basic concept for film growth *via* atomic layer deposition (ALD) is illustrated in Figure 3.3: A material is grown from at least two different chemicals A and B. In Figure 3.3, these correspond to Diethylzinc (DEZn) and water. These chemicals

are subsequently introduced into a reaction chamber (steps 1 and 4) separated by so called purge phases in which the reaction chamber is emptied of unreacted precursor and gaseous reaction products (steps 3 and 6). The chemicals are selected such that they react with the surface of the growing film in a self-terminating manner. This way, after one monolayer of precursor has attached to the substrate, there is no chemical reaction anymore (the situation after steps 2 and 5). Additionally, the precursors are complimentary in the sense that the surface left behind by precursor A is reactive to precursor B and vice versa. For purge phases sufficiently long to ensure strict separation of precursors A and B in the gas phase it is thus ensured that reactions leading to material deposition only take place at the surface and only last until all the reactive sites or species left behind by the preceeding precursor are consumed.

These processes are almost always conducted under vacuum, in a heated chamber and with a heated substrate. This vacuum chamber and its components are then called an ALD reactor. Usually, one also continuously pumps the reactor and keeps up a constant flow of a chemically inert purge gas from a mass flow controller to the pump. The ALD reactor I used for the work presented here is schematically depicted in Figure 3.4. The example in Figure 3.3 depicts the growth of zinc oxide from the precursors water and diethylzinc (DEZn, chemical formula: $Zn(C_2H_5)_2$). The DEZn-precursor consists of a zinc atom chemically bound to two ethyl ligands. This process can be run in a large range of deposition parameters which all procude a self-terminating or nearly self-terminating mode of film growth. For this example, one model of the ALD process looks as follows:

1. Initially, the substrate's surface contains hydroxyl groups, as depicted in Figure 3.3a.

2. The DEZn-precursor is introduced into the chamber as a vapor. This process is called pulsing and represents step 1 in Figure 3.3.

3. The DEZn molecules start reacting with the hydroxyl-groups on the substrate as depicted in Figure 3.3b. For each hydroxl group that is consumed, one ethane molecule (C_2H_6) is produced that quickly goes into the gas phase. The zinc atom in the DEZn molecule participating in the reaction attaches to the oxygen atom in the former hydroxyl group and is thus chemically bonded to the substrate surface. It is then referred to as being chemisorbed. The other ethyl ligand of the DEZn molecule remains bound to the zinc atom. Thus, an O-ZnC_2H_5 group is attached to the surface at the end of this step.

4. The substrate is exposed to the DEZn vapor for an exposure time $t_{exp,1}$, corresponding to step 2 in Figure 3.3. After this time, all hydroxyl groups are consumed and no chemisorption of precursor molecules takes place anymore. This is the state reached in Figure 3.3c. This exposure can be realized by simply pulsing enough DEZn into the chamber or by pulsing for a sufficiently long time while leaving the chamber attached to the running pump. Alternatively, one can disconnect the reactor from the pump during the exposure time.

5. One empties the chamber of all gaseous species (step 3 in Figure 3.3). At this point these are ethane and excess DEZn. If necessary, one continues pumping the chamber until physisorbed or condensed DEZn has detached from the surface and been pumped out of the chamber. At the end, the state depicted in Figure 3.3d is reached.

6. One pulses H_2O vapor into the chamber (step 4 in Figure 3.3). The water molecules react with the chemisorbed O-ZnC_2H_5 groups as depicted in Figure 3.3e. This reaction produces one ethane molecule per consumed water molecule and results in an attached O-Zn-OH group.

7. After the substrate has been exposed to the water vapor for an exposure time $t_{exp,2}$ (step 5 in Figure 3.3) all ZnC_2H_5 groups have been converted to chemisorbed O-Zn-OH groups. One layer of ZnO has been added to the substrate at this point already. The sample surface has now reached the state depicted in Figure 3.3f.

8. One empties the chamber of all gaseous species (step 6 in Figure 3.3). At this point, these are ethane and excess water molecules. If necessary, one continues pumping the chamber until physisorbed or condensed water has detached from the surface and been pumped out of the chamber.

9. The substrate surface now contains hydroxyl groups again and it is possible to repeat the procedure starting with step two. The state of the sample is now again the one depicted in Figure 3.3a, except that a layer of ZnO has been added to it.

With such a process it is possible to grow films conformally, at a growth rate of one monolayer of precursor that is constant everywhere on the sample, even deep inside pores and trenches. This property was *the* quality of ALD that prompted its heavy use in this thesis.
In the remainder of this chapter I will first give some details on the above steps that one needs to keeep in mind when choosing precursors and process parameters for an ALD process and in designing an ALD reactor. The films grown for the work presented here are ZnO, Al_2O_3 and TiO_2. All of these films were grown for different purposes and therefore the characterisation of the process and film properties undertaken varies from film to film. Where important for the other chapters of this thesis, I will also outline the properties of the films obtained in this chapter.

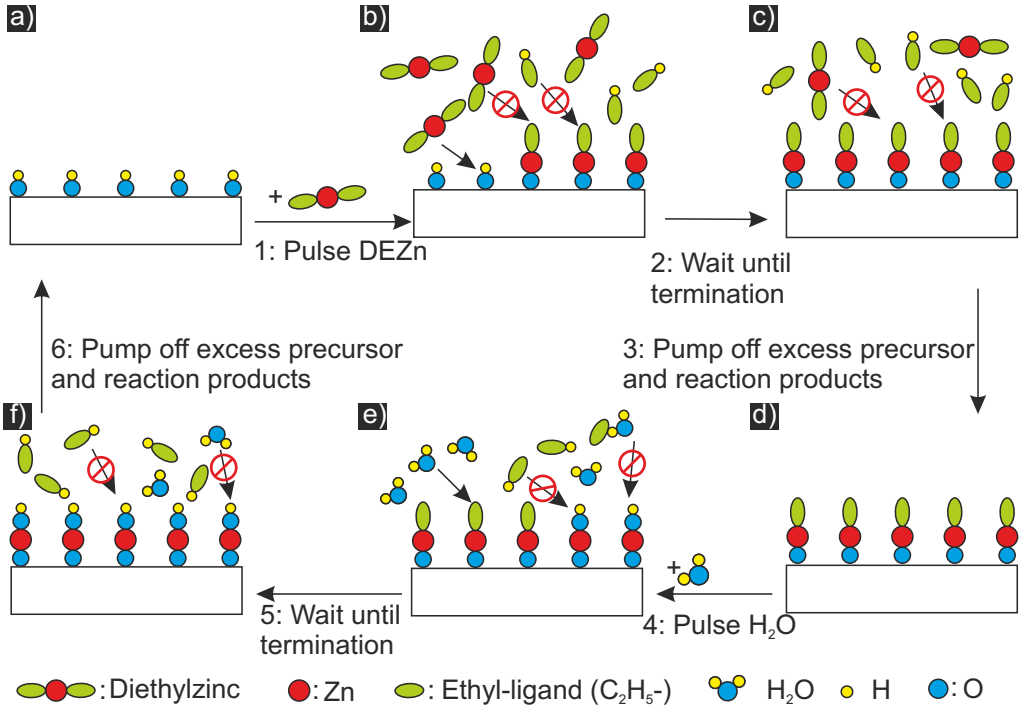

Figure 3.3: Schematic illustration of an ALD process taking the case of zinc oxide growth from diethylzinc and water as an example. All reactions between gas phase and substrate species that are required for the process to work are indicated by arrows. All reactions that must not occur between these species are indicated by crossed-out arrows. Reactions of surface or gas phase species with each other are not included but are discussed in the main text. Initiation of the film growth mechanism is possible in step 1 or 4 if the substrate is reactive to the respective precursor. All numbered arrows represent events that are influenced by the process parameters. The state of the sample depicted in the panels and the processes taking place in the individual images are dominated by the properties of the chose precursors, and to some extent by the temperature and the pressure inside the reactor.

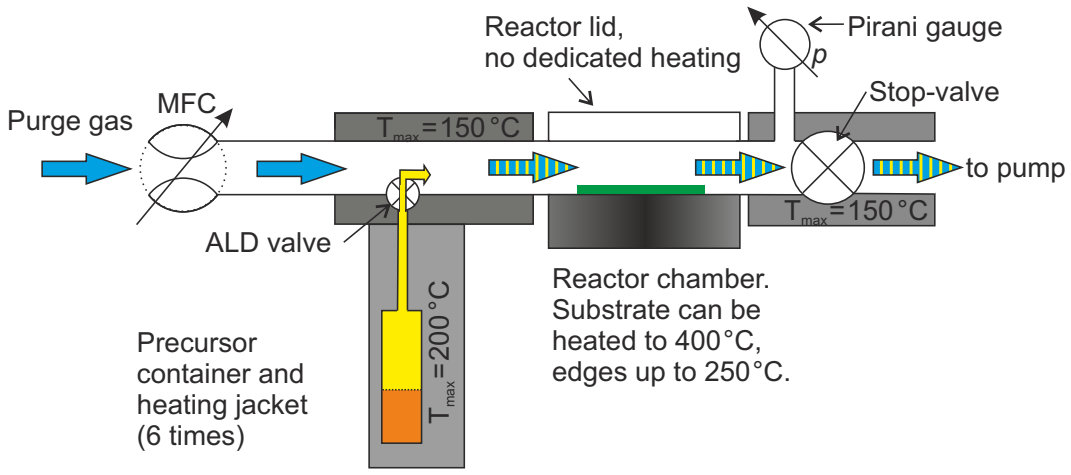

Figure 3.4: Schematic illustration of the reactor used in this thesis, a Savannah-100 ALD reactor by Cambridge Nanotech, Inc. A mass-flow controller is used to deliver purge gas (N_2 or Ar, blue) into the chamber with a flow between 6 sccm and 100 sccm. This carries the precursor vapor (yellow) which flows into the chamber if the ALD valve is opened. The reaction chamber contains two different heating elements: The central piece of the bottom of the chamber that carries the substrate (green) can be heated to 400 °C, the edge up to 250 °C. The substrate can be up to 4 inch in diameter. The lid of the reaction chamber is only heated by conduction through the chamber walls and the gas inside the chamber. The stop valve can be used to disconnect the pump from the reactor. Zones of heated piping are indicated by the gray areas, together with the maximum temperature to which the different elements can be heated. All other areas of piping are in contact with ambient air. A Pirani gauge is also installed. sccm: a unit of mass flow, see main text.

3.2.2 The details of atomic layer deposition

Phenomenology of an ideal ALD process

I will now point out the important points in the different steps of the ALD process. The Al_2O_3 process based on water and TMAl (chemical formula: $Al(CH_3)_3$) is the textbook example for an ALD process. Therefore, I will base all examples on this process where appropriate. The textbook model for this process is as follows [73]: TMAl, which consists of one Aluminum-atom bonded to three methyl ligands reacts with $n = 1$ or $n = 2$ hydroxyl groups on the substrate surface, releasing one or two methane molecules and leaving an O_n-Al-$(CH_3)_{(3-n)}$ group on the surface. This group is considered to be static for properly chosen ALD process parameters until water is pulsed into the chamber. The water removes the remaining methyl ligand and leaves behind hydroxyl groups. This reaction, as the one for growth of ZnO outlined above, is an example where a chemical reaction of the form

$$2 \cdot \mathrm{M(L)}_n + n \cdot \mathrm{H_2O} \rightarrow 2n \cdot \mathrm{HL} + \mathrm{M_2O}_n \tag{3.3}$$

is split up into the following two half-reactions:

$$m \cdot (\mathrm{OH})_{\mathrm{ads}} + \mathrm{ML}_{n,g} \rightarrow m \cdot \mathrm{HL_g} + (\mathrm{O}_m\mathrm{ML}_{n-m})_{\mathrm{ads}} \tag{3.4}$$

$$(\mathrm{O}_m\mathrm{ML}_{n-m})_{\mathrm{ads}} + (n-m) \cdot \mathrm{H_2O} \rightarrow (n-m)\mathrm{LH}_g + (O_m\mathrm{M(OH)}_{n-m})_{\mathrm{ads}} \tag{3.5}$$

Here, M indicates a metal atom, L indicates a ligand and the indices “g” and “ads” denote species that are adsorbed to the substrate or in the gas phase, respectively. If these reactions take place exactly as stated and only those reactions take place, an ideal ALD process is, indeed, arrived at. Such a process will result in conformal, pinhole free films, whose thickness is strictly proportional to the number of ALD cycles. In the following I will outline points that have to be considered when going beyond this simple approach in considering real-world ALD processes. Since I have focused on the growth of metal oxides in this thesis I will refer to one precursor as the metal precursor and the other precursor as the oxygen precursor.

Initiation of film growth

In order for an ALD process to start, at least one of the precursors has to be reactive to the substrate. This step is therefore precursor-specific. When working with trimethylaluminum (TMAl) or DEZn, this is usually not a concern as these will quickly react with any adsorbed hydroxyls. The TMAl molecule has also been shown to adsorb sufficiently strong to non-polar surfaces such as silicon to initiate growth without chemisorption. In this case, the first layer of adsorbed TMAl molecules reacts with the first pulse of water employed. In case of growing a TiO_2-film onto silicon, I found a deviation from the ideal, linear growth behaviour, corresponding to an effective nucleation delay of 12 cycles for untreated silicon. When subjecting the silicon to an air-plasma treatment for 10 minutes directly before the growth, I found a strictly linear growth behaviour. I therefore used this pretreatment for all the coating of

all samples discussed in this thesis as long as the samples were compatible with this treatment.

Thermal stability of precursors

For an ALD process to run as outlined above, it is essential that no film deposition occurs without consumption of chemically reactive surface sites. Any mechanism leading to such a deposition reaction would lead to a loss of conformality. This means that the precursor vapor has to be chemically stable during the whole exposure time t_{exp} at the deposition temperature unless it gets in contact with the surface. Gas phase reactions amongst the precursor molecules or between the precursor molecules and the gaseous reaction products can be permitted only if they do not lead to deposition. Also, the reaction product remaining at the surface has to be thermally stable until it is converted to the final film constituent by the complementary precursor or leaves the substrate into the gas phase. If it undergoes any changes, these too must not lead to film growth.

Upon increasing the substrate temperature one eventually reaches a regime in which the adsorbates are not stable anymore but start to decompose. If the decomposition process is slow with respect to the exposure time, self-termination of film growth may still occur. In this case, a layer-by-layer growth mode of a chemically pure film is maintained if the oxygen precursor is able to remove the by-products of the decomposition. There is a special case in which the precursor can decompose into the film material. This is the case for titanium isopropoxide (TTIP) which is one of the precursors I used to grow TiO_2. At substrate temperautres temperatures above 250 °C, thermal decomposition of this oxygen-containing precursor sets in, leading to formation of TiO_2 and other products. The latter can be removed by water and hydrogen-preoxide. [74–76] The appropriate term for this growth mode in the context of this thesis is, however, not ALD but pulsed chemical vapor deposition. The justification for this is as follows: I aim at infiltrating three-dimensional templates that contain tubes with a constant length. As material is deposited inside these tubes they get narrower and the exposure time necessary for the mere transport of precursors into the template will increase. For long exposure times, however, one would assume that TTIP will be able to adsorb onto the TiO_2 sites formed by decomposition. Then, the growth per cycle will not be surface-limited anymore but will instead be limited by the supply of precursor at the point of growth — as is the case in CVD. This is, therefore, not an acceptable mode of film growth. When depositing TiO_2 with TTIP, this effect therefore places an upper limit on the deposition temperature. Data demonstrating the assumption made above is found in Reference [77].

Precursor introduction and dosing

Regardless of what is happening in the chamber, an ALD process can only take place if the precursor can be delivered into the chamber in sufficient quantities. Several methods to do this exist. For non-gaseous, suitable precursors, the most convenient

is called vapor draw. It uses the vapor pressure p_{vap} of the liquid or solid precursor to simply push it into the chamber through the ALD valve. Thus, it can be easily implemented with a heated precursor container and one valve. Whether a precursor is suitable for this method of delivery depends on its vapor pressure at the temperature of the container and on whether it can condense inside the valve and piping or not.

I will first look at precursors that do not condense at the temperature of the valve and can be heated to have a vapor pressure higher than the pressure p_{ch} inside the chamber. For these, the flow q into the chamber through a valve with a flow coefficient C_{v} can be described using the equations for low and high pressure drop flow, respectively [78]:

$$q = N \cdot C_{\mathrm{v}} p_{\mathrm{vap}} \left(1 - \frac{2(p_{\mathrm{vap}} - p_{\mathrm{ch}})}{3p_{\mathrm{vapor}}}\right) \sqrt{\frac{p_{\mathrm{vap}} - p_{\mathrm{ch}}}{p_{\mathrm{vap}} G_{\mathrm{g}} T_{\mathrm{cylinder}}}} \quad \text{for } p_{\mathrm{ch}} > 0.5 p_{\mathrm{vap}} \tag{3.6}$$

$$\tag{3.7}$$

$$q = 0.471 N \cdot C_{\mathrm{v}} p_{\mathrm{vap}} \sqrt{\frac{1}{G_{\mathrm{g}} T_{\mathrm{cylinder}}}} \quad \text{for } p_{\mathrm{ch}} < 0.5 p_{\mathrm{vap}} \tag{3.8}$$

Here, q is the flow measured in sccm, N is a constant with the value $6.95{\cdot}10^6\,\mathrm{K}^{-1/2}\mathrm{sccm/bar}$, T is the temperature of the precursor container, the pressures are taken in bar and G_{g} is the weight of the gas relative to that of air. The unit sccm denotes a flow of 1 cubic centimeter of gas at 0 °C and a pressure of 101,325 Pa. The ALD valves employed here have a flow coefficient of $C_{\mathrm{v}} = 0.27$. To get a feeling for the numbers we are looking at here, I will consider the case of TMAl, whose vapor pressure follows $\lg(p_{\mathrm{vap}}/\mathrm{torr}) = 8.22 - 21343.8\mathrm{K}/T$ and whose vapor is 2.49 times heavier than that of air. In a freshly filled container of TMAl, the space available for vapor is 30 ml. If the cylinder is not intentionally heated, it will have a temperature of approximately 39 °C. At this temperature, the vapor pressure of TMAl is 31 mbar. Putting these numbers together tells us that $2.3{\cdot}10^{19}$ molecules are in the cylinder. If the chamber pressure is 3 mbar, $6.6 \cdot 10^{18}$ of these molecules will flow into the chamber within the nominal minimum opening time of the ALD valve of 15 ms. The total inner surface of the chamber and the piping leading to it is a bit smaller than $0.05\,\mathrm{m}^2$. An equally large area of silicon oxide would contain up to $0.3 \cdot 10^{18}$ hydroxyl groups [79]. Thus, this dose of precursor is sufficient to saturate the inner surface of the reactor and leave enough molecules to saturate another $0.32\,\mathrm{m}^2$ of sample surface.
For water, hydrogen peroxide, TMAl, and DEZn this procedure works well. These precursors are liquids inside their containers, but the vapor pressures are sufficiently high. Also, condensation is not an issue since their boiling points at 1 bar are all below 150 °C. Since the valves and the piping can be heated up to 150 °C, condensations can thus be avoided. In the case of TTIP, the vapor pressure is theoretically high enough but the vapor draw method did not work, possibly due to a low evaporation rate. Details for this case are discussed below.

Purging, exposure and precursor condensation

As outlined above, one of the necessary ingredients for a conformal ALD process is the strict seperation of the precursors inside the reaction chamber and a sufficient, at least saturating dose of every precursor during every pulse. These requirements can easily be fulfilled if one takes the liberty of allocating arbitrarily long times for the purge steps 5 and 8 in the scheme outlined above. In order to minimize the necessary time for these steps, it is useful to heat all parts of the reactor to as high a temperature as possible. The limiting factors here are the thermal stability of the precursors used and that of the components of the reactor. In the case of the Savannah-100 reactor I used, these are the ALD valves, the O-ring seals and the mass flow controller used to introduce purge gas. The mass flow controller's operation temperature is 50°C. Therefore, it has to be sufficiently thermally isolated from other heated parts of the ALD reactor which can be heated to at least 150°C. This has an important implication for processes in which long residence times of the precursors in the chamber are neccesary: If the pump is to be seperated from the chamber, the precursor molecules inside the chamber will start to diffuse back to the mass flow controller. Besides the possible damage they might do to it, they will necessarily encounter surfaces that are substantially cooler than the rest of the chamber on their way. Precursors that are liquids at room temperature will likely condense there. Very long pump times will be necessary to remove this condensate from those surfaces. Also, since it is located "upstream" of everything else in the reactor, the vapor created by these condensates over time will come in contact with everything in the chamber. This means that with the pump disconnected from the chamber it is necessary to maintain a sufficient flow of purge gas into the chamber to avoid back-diffusion and condensation of the precursors. Thus, long residence times imply rising pressure in the chamber.

Another solution for long exposure times would be to devise a system in which the precursors can be supplied continuously to the chamber while it is connected to the pump. There is no fundamental problem with this. With the vapor draw method, this is not feasible, however, if the evaporation rate of the precursor is not incidentally exactly the one needed for saturation or slight overdosing. If this is not the case, a continuous flow of precursor with a vapor draw method would lead either to underdosing or strong overdosing. Underdosing leads to non-saturating conditions. Strong overdosing is extremely dangerous, as common ALD precursors cannot be allowed to mix in large quantities due to the high reactivity they are designed to have towards each other. Even if one avoids a mixing in the gas phase, the vapors will accumulate in the oil of the pump or in the exhaust, leading to damage to the system.

3.3 Deposition of Al_2O_3

The process for depositing doped zinc oxide that was used for the work described in Chapter 4 relied on aluminum as a dopant. This was introduced into the growing zinc oxide film by introducing a TMAl pulse between ALD cycles of zinc oxide. Aluminum

oxide test films were grown for this. Also, the ALD process for Al_2O_3 using TMAl and H_2O is the most robust and well-documented ALD process known. It can be used to test the state of the ALD reactor, check for leaks, and test the homgeneity of deposition across the substrate. Al_2O_3 films for these purposes were grown from H_2O or H_2O_2 and TMAl. These precursors are liquids which have a sufficient vapor pressure at room temperature to not need heating. However, TMAl is pyrophoric and needs to always be handled under dry, inert gas. The pulse times were 15 ms, the necessary purge times at 110 °C and 250 °C substrate temperature, respectively, were found to be on the order of 60 s and 5 s. In the former case the other parts of the chamber were heated to 110 °C, in the latter case they were heated to 150 °C. A continuous flow of 20 sccm nitrogen or argon was used for purging, and the chamber was continuously pumped. The growth rate is approximately 0.11 nm/cycle at 250 °C.

3.4 Deposition of ZnO

ALD of ZnO was used for the work described in Chapter 4. Also, ZnO was used as an intermediate material in the titania double-inversion procedure. Planaer zinc oxide was grown from H_2O and later H_2O_2 and Diethylzinc (DEZn) which was not heated. Like TMAl, DEZn is a pyrophoric liquid and needs to always be handled under dry, inert gas. For the growth on planar substrates, the same growth parameters as those for Al_2O_3 can be used. However, DEZn suffers from a slow thermal decomposition at 250 °C [80] which needs to be taken into account when increasing the exposure above values used for planar films. The growth rate at 250 °C is about 0.19 nm/cycle. The films are conducting, the refractive index is on the order of 2.

3.5 Deposition of TiO_2

3.5.1 Precursor screening

TiO_2 can be grown from titanium-halides, titanium-alkoxides and titanium-amides. Out of this group of precursors, I evaluated titanium-isopropoxide (TTIP, CAS-number 546-68-9), titanium-tetrachloride ($TiCl_4$, CAS-number 7550-45-0) and tetrakis-(dimethylamido)-titanium (TDMATi, CAS-number 3275-24-9) for the deposition of TiO_2 in this thesis because they are the three most commonly used precursors for ALD of titanium oxide. This way I could compare my results to published results as easily as possible. I eventually discarded $TiCl_4$ and TDMATi for the following reasons:

- $TiCl_4$ and water [81–83] can be used to grow TiO_2 using the half-reaction deposition scheme characteristic to ALD up to at least 400 °C. [84] The produced HCl leads to massive corrosion of the pump and the reactor, however. Also, a process called self-poisoning is likely to occur. [82, 85] In short this means that the reaction byproducts of the film forming reaction adsorb at reactive sites on the sample surface and inhibit the film growth in the next cycle. This leads

to a decreased growth rate and in a loss of conformality, severly limiting the usefulness of this precursor for coating high aspect-ratio samples such as those used in the double-inversion procedure used to create TiO_2 woodpile photonic crystal (see Chapter 5).

- TDMATi can be used to deposit TiO_2-films with a higher refractive index than the films deposited from TTIP and H_2O at 250 °C (see below) but turned out to not be sufficiently thermally stable at 250 °C for use in the double-inversion procedure described in Chapter 5. Since the samples produced in this thesis required the ALD process to infiltrate and fill pores of an initial diameter on the order of 100 nm and a length of 135 000 nm, the precursors needed to be kept in the chamber for as long as possible. The maximum infiltration time was 110 s, but it turned out that TDMATi does not conformally coat the templates under these conditions and that the growth rate is larger at these conditions than it is under standard conditions that minimize the precursor residence time in the chamber. The most likely reason for both of these phenomena is that TDMATi is not entirely stable against thermal decomposition. This assumption is supported by other findings [86] that have shown that a TiN film grown using the same precursor exhibits carbon concentrations in excess of 6% throughout the entire film even at 200 °C growth temperature. TDMATi was the only carbon containing chemical species used in these experiments, implying TDMATi as the carbon source.

For these reasons, TiO_2 was grown from H_2O and later H_2O_2 as an oxygen source and TTIP as the metal-containing precursor. It is an air-sensitive liquid that should be handled under dry, inert gases only. Its vapor pressure is $\lg(p_{\text{vapor}}) = 9.837 - 3193.7/\text{T}$ [87] where p is measured in Torr. At room temperature it therefore has a vapor pressure of 0.13 Torr, which is not sufficient to introduce it into the chamber with the vapor draw method. The degree to which it can be heated to increase the vapor pressure is limited as well, however, since TTIP ages inside the precursor cylinder under the influence of heating, resulting in a decrease in growth rate[1] (also see Figure 3.5). The duration of one TiO_2-growth run for the double-inversion procedure is 8 days. One should therefore limit the amount of heating to a reasonable minimum. A satisfactory method turned out to be a pressurisation of the precursor container to approx. 200 mbar with argon before opening the ALD valve, such that the precursor vapor inside the cylinder is swept into the chamber by the Argon and heating the TTIP to 80°C. At this temperature TTIP has a vapor pressure of 6.2 Torr. Theoretically, this pressure is sufficient to introduce it into the chamber using the vapor draw method. However, reproducible results could not be obtained with it, possibly because the evaporation rate of TTIP is not high enough to actually reach the vapor pressure in

[1] Eric Deguns has systematically examined this aging process in an ALD setup identical to the one I used while working at Cambridge Nanotech. He has found a reduction in the growth rate per cycle of more than 60% for 45 days aging at 75°C and a visually apparent aging of the precursor after 3 days at 90°C. Unfortunately the data was never published before the bankruptcy of Cambridge Nanotech. He currently works at Oerlikon-Leybold, USA.

the time between two pulses. With the pressurisation of the container, a growth rate of 0.053 nm/cycle was reached at a substrate temperature of 250 °C. Even for 1.5 s pulse time and 20 min between pulses this value would not be reached with the vapor draw method.

Besides the effect of the aging apparent by the reduction in growth rate, the precursor also leaves a solid residue in the cylinder which can be removed using a bath of 80 °C hot 25% KOH solution. Fresh TTIP, filled into the cylinder under an argon atmosphere in a glovebox was, therefore, used for every deposition run shown in this thesis unless otherwise noted.

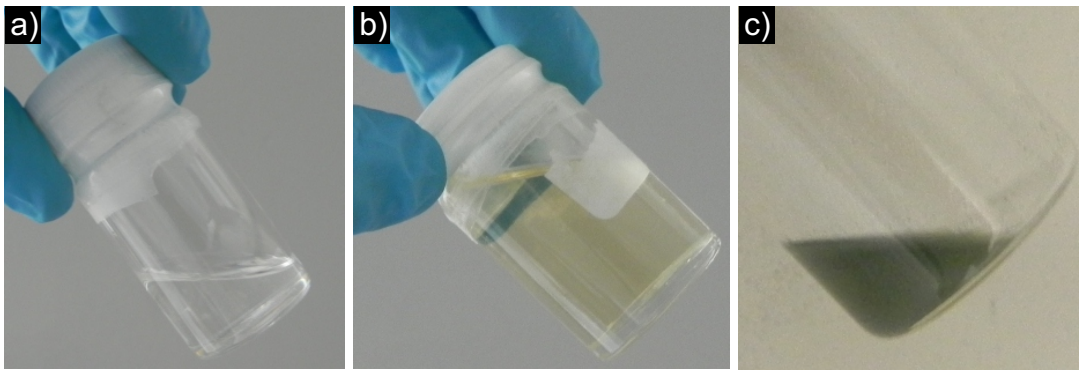

Figure 3.5: TTIP aging. a) fresh precursor b) precursor that has been in a stainless-steel precursor cylinder for five months with 12 days at 80 °C. c) precursor that has been in the cylinder at 80 °C for 40 days.

3.5.2 Refractive index of ALD grown TiO_2-films

As the refractive index is a key parameter for the correct design of woodpile photonic crystals, I measured the refractive indices of the TiO_2-films. As a dependence of the refractive index of TiO_2 films grown by ALD on the used precursors has been reported [88] for films grown at 120 °C I also examined the influence of the precursors on the refractive indices. The measured refractive indices for TiO_2 films grown under conditions identical to those used in the procedure for the fabrication of titania woodpiles using TTIP and TDMATi as Ti-precursors and water as well as H_2O_2 as the oxygen source are shown in Figure 3.6a.

The data shown in Figure 3.6a are derived from variable angle spectroscopic ellipsometric (VASE) measurements [89]. In these measurements one directs polarised light onto the sample at oblique angles and measures the polarisation ellipse of the beam which is reflected at the different interfaces in the sample, see Figure 3.6b. On one hand, the fresnel coefficients for reflection at the different interfaces are polarisation dependent and sensitive to the refractive indices at both sides of the interface. On the other hand, the interference between the reflected beams is dependent on the optical path that the light has traversed and by virtue of this on the angle of incidence

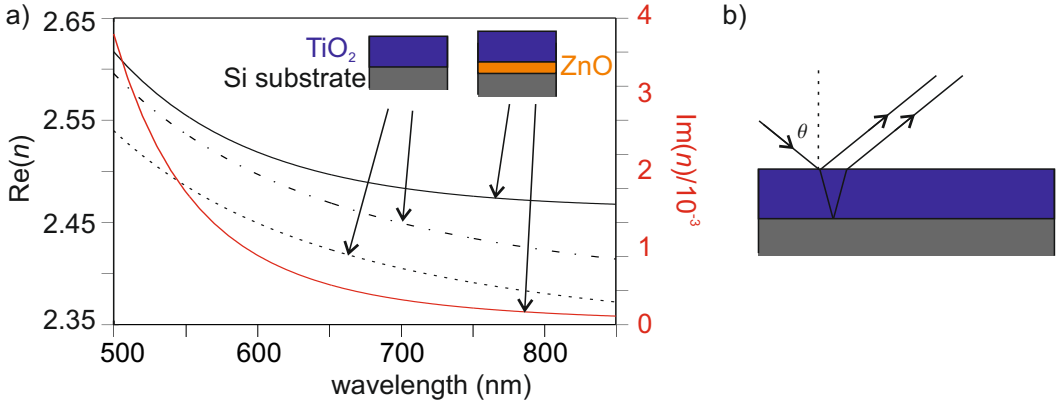

Figure 3.6: Optical properties of TiO_2 films grown by ALD and measured with variable angle spectroscopic ellipsometry (VASE). a) The real part of the refractive indices of TiO_2 films grown using different combinations of precursors: TTIP and water (dashed line), TDMATi and H_2O_2 (dash-dotted line), and TTIP and H_2O_2 (solid black line). For the combination of TTIP and H_2O_2 the imaginary part of the refractive index is also shown (red line). The insets show the layer sequence of the different samples. b) Illustration of the measurement principle of VASE: A change in polarisation of linearly polarised light is caused by interference of the partial beams reflected at different interfaces in the sample. A VASE dataset can be inverted to give information about the refractive index and the film thickness if the measurement includes several angles θ of incidence.

θ. The detected light beam is therefore generally elliptically polarized. This change of polarisation can be mapped unambiguously onto refractive indices of the layers if the layer thicknesses are known or if several angles of incidence θ are measured and the layer thicknesses are roughly known. In order to take data corresponding to a well defined system, the exclusion of reflections from the backside of the substrate is necessary. The samples for the VASE measurements were therefore grown on silicon substrates which are intransparent for visible light, except the film grown using TTIP and H_2O_2. This precursor combination is the one eventually used in the titania double-inversion described in Chapter 5. This film is grown on a ZnO layer deposited at 110°C substrate temperature, an Argon flux of 20 sccm, a precursor exposure time of 110 s, 0.015 s pulse duration for DEZn and H_2O_2, 120 s purge time and all other parts of the machine held at 110 °C. These conditions are identical to those used for the ZnO reinfiltration step of the titania double-inversion. The only deviations from the procedure are the presence of the silicon substrate and the fact that TiO_2 is grown onto a planar surface instead of one with a radius of curvature of 50 nm. Also, the ZnO that TiO_2 is grown onto during the double-inversion originates from two ZnO ALD steps: A first step during which roughly 70 nm are grown and a second step which deposits about 12 nm. In between the two steps, the ZnO is heated to 420 °C

for 12 hours. This treatment might change the ZnO film for the first step which is the starting surface for the second one. The heat treatment is omitted here because ZnO films submitted to it develop severe cracks, making later VASE measurements impossible. Since I have grown 12 nm of ZnO onto the silicon substrate for the VASE measuremts using the double-inversion process parameters for ZnO and have then deposited the TiO_2 film on to this layer, this sample represents the material found in the final woodpiles as closely as possible.

In addition to the amorphous form of titania there are three different polymorphs with different optical properties: Rutile, Brookite and Anatase. The X-ray diffractogram shown in Figure 3.5.2 clearly shows that the Brookite and Rutile phases are absent in the films I grew. The anatase phase is present. Its refractive index is a bit higher than the one measured on the TiO_2 films ellipsometrically. This indicates that the films consist of a mixture of anatase and amorphous titania, consistent with published results. [76,90] It should also be pointed out that the film on which the spectrum was taken was 10 times thicker than the ones grown during one double-inversion.

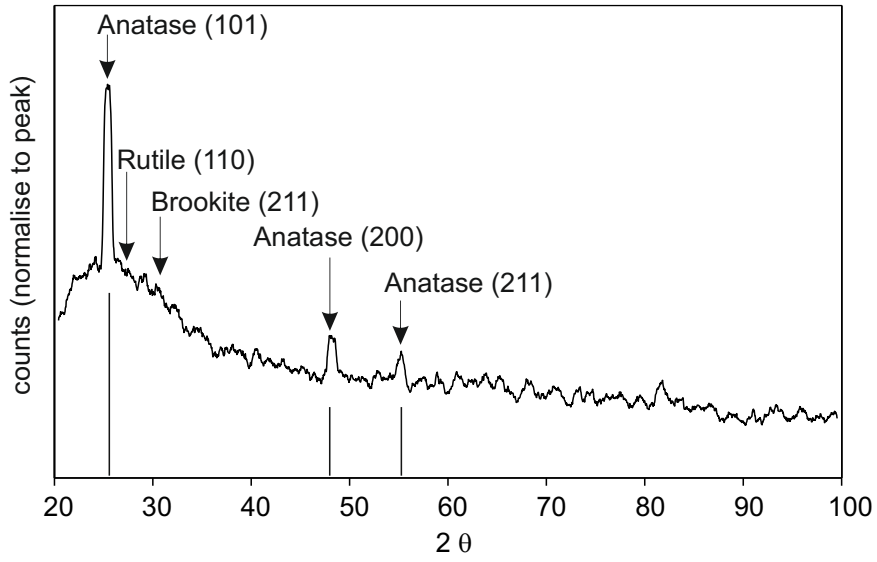

Figure 3.7: X-Ray diffractogram of an ALD grown TiO_2 film. The positions of three anatase peaks are indicated by the arrows. The bars show the relative intensities of these peaks as taken from literature. [91] The position of the most prominent peak of the rutile phase [92] and the second most-prominent peak of the brookite phase [93] are indicated at the position given by literature. The most prominent brookite-peak overlaps with the anatase (101) peak and has therefore been omitted.

It would be conceivable to use a different temperature than 250 °C for the double-inversion. In the literature two findings have been established however: First, 250 °C

is a clear upper limit on the temperature at which a self-limiting ALD reaction can be performed with TTIP. [76,90,94] Above 250 °C a CVD-like film growth sets in during which film growth occurs by thermal decomposition of TTIP. Secondly, the refractive indices of TiO_2-films grown by ALD increase with the depositon temperature. For these reasons I have not investigated the influence of the deposition temperature and have limited myself to working with the maximum possible temperature. The VASE measurements on test films of TiO_2 deposited under the same conditions as those used in the double-inversion show that these films have a refractive index that is sufficiently high for their use as a constituent material for a photonic cyrstal crystal with a complete photonic bandgap in the visible part of the electromagnetic spectrum.

4 Doped ZnO films with tailored plasma frequencies

As discussed in Chapter 2 the ability to deposit films having a tailored plasma frequency is useful, possible even unavoidable for some implementations of metamaterials. We have also seen in Chapter 3 that atomic-layer deposition (ALD) is one method of choice for this application as it is inherently a conformal coating technique. In this chapter we will see how ALD can also be used conceptually easily to deposit films of ZnO (a semiconductor with a bandgap of 3.3 eV) with a tailored doping and therefore a tailored permittivity.

4.1 Approach to deposition of tailor-doped films

ZnO is a semiconductor with a bandgap of 3.3 eV, *i.e.*, it is transparent in the visible and infrared spectral range. It can be n-doped with different elements, *e.g.*, Aluminum, Indium and Gallium. In case of Aluminum-doping, it is sometimes referred to as AZO. Since there are well known ALD processes for aluminum- and zinc oxide, see for example References [73, 95, 96], I combined these two processes to deposit ZnO doped with Al. I also tested if ZnO can be doped efficiently with Titanium, but found that doping with Aluminum leads to better results. For the film growth I followed the scheme depicted in Figure 4.1. Here, N cycles of ZnO are grown from Diethylzinc (DEZn) and water, followed by one doping cycle with Trimethylaluminum (TMAl). I refer to such a sequence of N cycles of ZnO-growth and one cycle of doping as a macrocycle.

There are three conceivable pulse sequences to introduce a dopant for a macrocycle containing N cycles of ZnO-growth:

1. Grow N-1 cycles of ZnO, followed by pulses in the order H_2O, DEZn, H_2O, TMAl, H_2O, DEZn, then grow ZnO as usual. In terms of surface chemistry and pulse sequences this case is most similar to growing one cycle of Al_2O_3 onto a hydroxlyated ZnO surface and followed by growth of ZnO on a hydroxylated surface.

2. Grow $N-1$ cycles of ZnO, followed by pulses in the order DEZn, H_2O, TMAl, DEZn, H_2O, then grow ZnO as usual. In terms of surface chemistry and pulse sequences this case corresponds to the first half-reaction of Al_2O_3-growth on a hydroxylated surface, followed by the the exposure of the TMAl-covered surfaced to DEZn-vapor. The layer resulting from this exposure is then oxidised by the

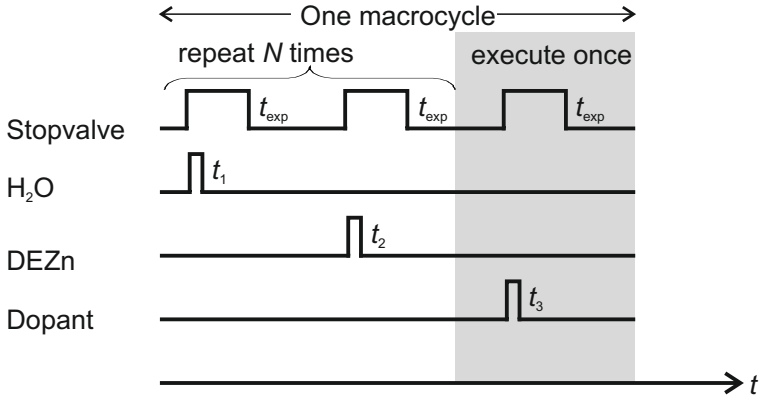

Figure 4.1: Pulse sequence used for one macro-cycle of doped ZnO film growth. The vessels containing the precursors are opened for a time t_i ($\mathrm{i}=1,\ 2,\ 3$) and the precursor vapors are held in the reaction chamber for a time t_exp to allow sufficient time for the precursors to react with the substrate surface and infiltrate a threedimensional polymer template. This is done by closing the valve connecting the ALD reactor to the pump. After N cycles of ZnO-growth, an additional dopant pulse is introduced into the chamber. Adapted from Reference [97].

water pulse. If the surface chemistry of the DEZn and TMAl precursors is ideal in the sense discussed in Chapter 3, this film will be identical in composition to the one grown with the first pulse scheme because the DEZn precursor will not be able to attach to the TMAl-covered surface. The DEZn pulse would then leave the surface unchanged and only after the subsequent H_2O-pulse, would growth occur as usual.

3. Grow N-1 cycles of ZnO, followed by pulses in the order H_2O, DEZn, TMAl, H_2O, DEZn, then grow ZnO as usual. This pulse sequence is the one shown in Figure 4.1. For ideal precursor chemistries TMAl would not be able to attach to the DEZn covered surface, resulting in an undoped ZnO film.

I tested if the order employed makes a difference for a macrocycle corresponding to $N = 18$. The material parameters retrieved as described below were not significantly different, however, so that I worked with the third case. The reason for this was that the TMAl precursor has been reported to etch the surface of a growing film ZnO-film if $N < 7$. For $N > 7$, the growth rate during the TMAl-pulse is still lower than during regular growth of Al_2O_3. [98] Both of these observations suggest that usage of the third case will results in a sub-monolayer coverage of adsorbed TMAl during the doping and therefore in a less dense concentration of Al-dopants than in the case of a close-packed monolayer. The other deposition parameters were a substrate temperatur of 250 °C, 150 °C heating of the remaining parts of the reactor, an exposure time of $t_\mathrm{exp} = 1\,\mathrm{s}$, purge times of 30 s using a flow of 20 sccm of nitrogen and 0.015 s pulse

times for all precursors. All precursors were unheated. The process parameters are chosen in such a way that the conformal coating of polymer templates produced by direct laser writing is possible. The number of macroycles was chosen such that films with thicknesses on the order of 250 nm were obtained. All films discussed here were grown onto microscopy glass-slides unless noted otherwise.

4.2 Spectroscopic characterisation of tailor doped ZnO-Films

Transmittance and reflectance spectroscopy can probe the permittivity of a thin film. In this thesis a Fourier-Transform Infrared spectrometer (FTIR spectrometer) was used for this purpose. The instrument is a Bruker Equinox 55 device with an attached Hyperion microscope. It uses a cassegrain objective or alternatively, a Calcium-Fluoride objective to focus light onto the sample and collect it. The former objective is reflective and therefore non-dispersive but will focus light onto the sample with incidence angles between 15 °and 30 °, whereas the latter focuses the light onto the sample in a cone centered around 0 °but is transmissive and therefore has chromatic aberrations, which are given by the dispersion of the CaF_2. This effect is not very pronounced over the interval between 1 µm and 5 µm [99], but it becomes more important at longer wavelengths. The working distance of the CaF_2 objective is too large to allow the use of 2 CaF_2-objectives for transmission measurements with the Hyperion microscope. For normal-incidence measurements in transmission the Cassegrain-objective can be used if one limits the angles of incidence of the beam by blocking parts of the objective and tilts the sample to lie perpendicular to the unblocked beam. This is illustrated in Figure 4.2b. An essential part of the FTIR spectrometer is the Michelson-interferometer contained in it as shown in Figure 4.2. The beamsplitter in the interferometer is the only transmissive component of the Equinox spectrometer and does not work for all wavelengths between 500 nm and 5 µm. Therefore, 2 beamsplitters are used alternatingly. A quartz-beamsplitter that works for wavelengths of light shorter than roughly 1.1 µm and a Si/CaF_2 beamsplitter working for longer wavenlengths. When investigating samples over both of these wavelength ranges, it is therefore necessary to change the beamsplitter. This in turn necessitates taking two reference spectra which might not be continously connected to each other at 1.1 µm. This is the cause for the discontinuities in some of the spectra shown in the remainder of the chapter.[1]

For the reflectance measurements a silver mirror was used as a reference, in transmission a microscope glass-slide similar to the one the samples were deposited on was used. Before the measurements the film grown on the backside of the substrate was removed by application of a drop of dilute HCl followed by a rinse in H_2O. Figure 4.3 shows a selection of spectra of differently doped films spanning the aluminum concentrations I examined.

[1] Even if working in only one freqeuncy range a slightly different alignment of the reference and the sample leads to a slight error in the spectra. This is not evident from a graph, however, because in this case the error is a multiplication with a wavelength-dependent but continuous function.

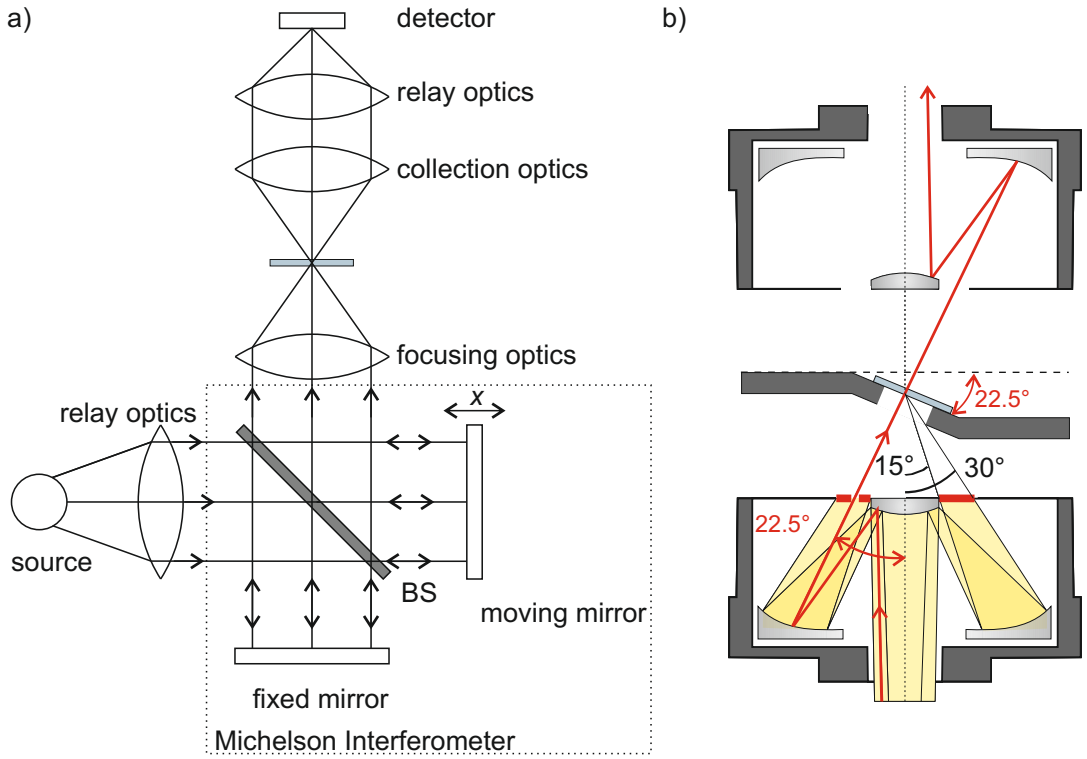

Figure 4.2: a) Schematic illustration of the FTIR spectrometer used: A tungsten-lamp serves as a light-source for infrared and visible light. Its output is relayed into a Michelson-interferometer. Here, the light-beam is split by a 50%/50% beamsplitter. The 2 beams are reunited after having traversed different optical paths in the 2 arms of the interferometer, leading to them interfering with a phase difference proportional to the displacement of the moving mirror. The light is then relayed to the Hyperion microscope where it is focussed onto the sample either by the Cassegrain-objective or a CaF_2-lens. Either the transmitted or the reflected portion of the light is collected and relayed to the detector. The Fourier-transform of the intensity of the detector as a function of x contains the transmission or reflection of the sample as a function of wavelength. In the Equinox-spectrometer, both arms of the interferometer are attached to one sea-saw that is continuously tilting and the time-resolved position of the interferometer is recorded by following the intensity of a HeNe-Laser passing the same interferometer. The same principle applies, however. b) Sketch of the Cassegrain-objective and its usage for transmission measurements under normal incidence. Curved mirrors are used to focus light onto the sample at incidence angles between 15 °and 30 °with respect to the optical axis. If one tilts the sample and uses the apertures shown in red to block most of the light, it is possible to take transmission spectra under normal incidence.

4.3 Understanding the spectra of doped ZnO-films

The measured reflection and transmission spectra can be compared to spectra calculated for the layer-stack depicted in Figure 4.3: An air half-space, a film of thickness d with drude permittivity, 170 µm of glass, another air halfspace. The inclusion of the second air half-space is necessary to correctly account for the 4% of light reflected at the air-glass interface and the absorption occuring in the glass substrate at infrared frequencies. Its inclusion produces rapid Fabry-Perot oscillations in the calculations. If one uses a coarse set of frequencies for modeling, it would be necessary to pick the frequencies in such a way that one knows on which part of this oscillation the reflection or transmission value for this frequency is located. I therefore used a frequency grid corresponding to the experimental resolution of 0.12 THz. All measured and calculated spectra shown in the remainder of this section are a moving average of 6 THz range over these data.

For the calculations a self-written implementation of the method described in Reference [100] was used and the imaginary part of the refractive index of the glass substrate was determined from reflection and transmission measurements on bare glass substrates. To determine the Drude-parameters of a given film, the slab thickness d, the background permittivity ϵ_∞, the plasma frequency ω_{Pl} and the damping frequency γ were used as fit parameters. Initially, the fitted thicknesses were checked against values taken from SEM-micrographs of the sides of fractured samples. They did not deviate from these values by more than 20 nm, corresponding to a deviation of less than 10%. In addition, the Fabry-Perot oscillations visible near the blue end of the spectra of the films contain information about the (weakly varying) optical thickness at these wavelengths. Since the physical film-thickness is, of course, fixed and the dispersion of the Drude model permittivity is weak in the visible for all the parameters considered here, this part of the spectrum is most sensitive to the high-frequency limit ϵ_∞ of the Drude permittivity and the film thickness. This fit procedure worked well for doping levels corresponding to $N \leq 144$.

The permittivity of AZO is changing from that characteristic of a dispersive dielectric to that of a metal as the frequency is decreased. The increase in reflection towards low frequencies, accompanied by the drop in transmission that is seen in the spectra is indicative of this transition. The transition sets in at increasingly higher frequencies as the carrier concentration inside the AZO films and therefore the plasma frequency is increased. For a very high doping density corresponding to $N = 6$ the reflectivity starts to decrease again in comparison to $N = 12$. One possible explanation for this is that these highly Al-doped films are made up of a mixture of Al:ZnO and the spinel $ZnAl_2O_4$ which is a non-conductive ceramic. This process might be even more pronounced by an overporportional Al-content due to the etching of the ZnO-surface by the TMAl-precursor which has been observed for $N < 7$. [98] Since this renders this film uninteresting as a tailored metal, we did not investigate this further, however.

In order to test whether the thus derived Drude-parameters are due to Aluminum doping we have looked at various films doped to different degrees N. Considering the

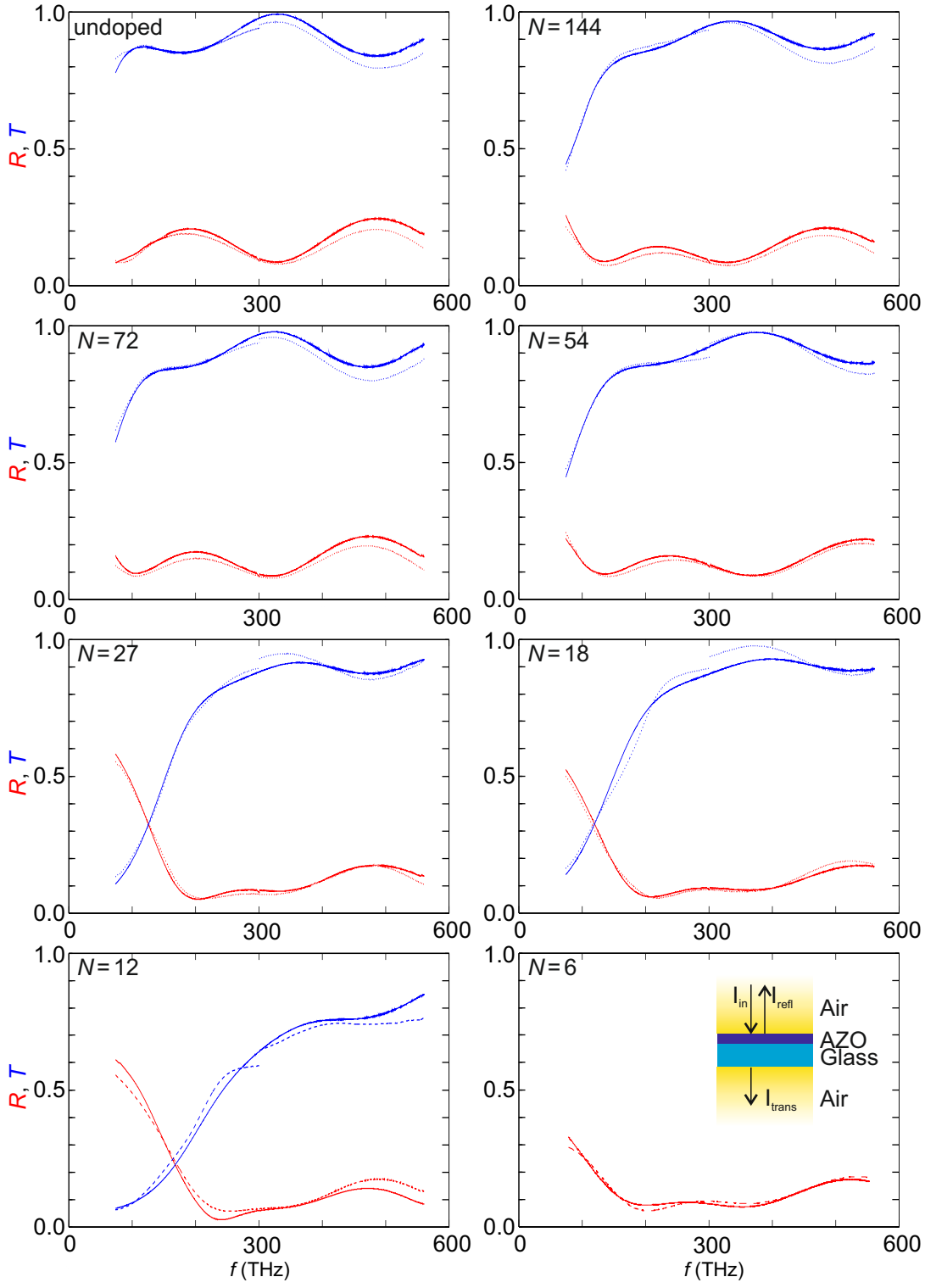

Figure 4.3: Reflection (blue) and transmission (red) spectra of ZnO films with different doping concentrations. The dashed lines show measured data, the solid lines are fits using the Drude model as described in the text. For $N = 6$ only reflection data is shown. The inset shows the geometry of the measurements which is also considered in the calculations (not to scale).

prediction of the Drude model that

$$\omega_{\mathrm{Pl}}^2 = \frac{ne^2}{m^*\epsilon_0}, \tag{4.1}$$

we would expect ω_{Pl} to vary proportionally to $\sqrt{n} \propto \sqrt{\frac{1}{N}}$, where m^* is the effective electron mass, n is the density of free electrons, e is the electron charge and ϵ_0 is the vacuum permittivity. Looking at Figure 4.4, which displays the Drude parameters as a function of dopant concentration, we see that this is approximately the case for $N \geq 12$. However, we note that extrapolating the data points for ω_{Pl} back to a nominally undoped film, there seems to be some intrinsic doping in the films corresponding to a plasma frequency of $\omega_{\mathrm{Pl}} = 2\pi \cdot 63 \cdot 10^{12}\,\mathrm{s}^{-1}$. We attribute this to a non-stochiometric composition of the ZnO due to an increased zinc-content from a slow DEZn decompositon-reaction that takes place in parallel to the desired ALD growth reactions. [80, 101] We also notice a slight dependence of the damping frequency on the dopant concentration for $N \geq 18$ and a greatly increased damping for $N = 12$.

Based on this, we assumed that for $N \geq 12$ the film's optical properties can faithfully be described using the Drude model. We further checked this assumption by measuring the dopant concentration in these films by energy-dispersive x-ray (EDX) spectroscopy. In this method, bound electrons of the atoms in the sample are excited by a beam of electrons. The spectrum of the x-rays this produces is given by the electronic energy levels and is therefore characteristic for the atoms the electrons belong to. EDX spectra can in principle be evaluated quantitatively. However, the EDX-spectra were collected using the electron beam of a LEO 1530 scanning electron microscope that is also used for imaging. In this case, the excited volume has a pear-like shape and includes the glass-substrate which contains about 1% aluminum-oxide. Since the exact dimensions of the excited volume are not known, a reliable quantitative determination of the Al-content of the films is not possible from one measurement only. However, it is possible to take the Al-signal measured for an undoped ZnO-film as a reference and subtract this value from the Al-signal measured on doped ZnO-films of the same thickness. The thus-obtained value should then give a reliable estimate for the Al-concentration in the doped ZnO-films. This data is presented in Figure 4.5.

The titanium doped ZnO (Ti:ZnO) films mentioned above turned out to be inferior in performance as a tailored metal: For a doping level of $N = 20$, the retrieved plasma frequency was $\omega_{\mathrm{Pl}} = 2\pi \cdot 185 \cdot 10^{12}\,\mathrm{s}^{-1}$ and a damping frequency of $\gamma = 2\pi \cdot 57 \cdot 10^{12}\,\mathrm{s}^{-1}$. For $N = 18$ the plasma frequency for the case of Aluminum-doping is $\omega_{\mathrm{Pl}} = 2\pi \cdot 297 \cdot 10^{12}\,\mathrm{s}^{-1}$ at a comparable damping of $\gamma = 2\pi \cdot 53 \cdot 10^{12}\,\mathrm{s}^{-1}$. Therefore AZO is a better choice as a tailored metal than Ti:ZnO.

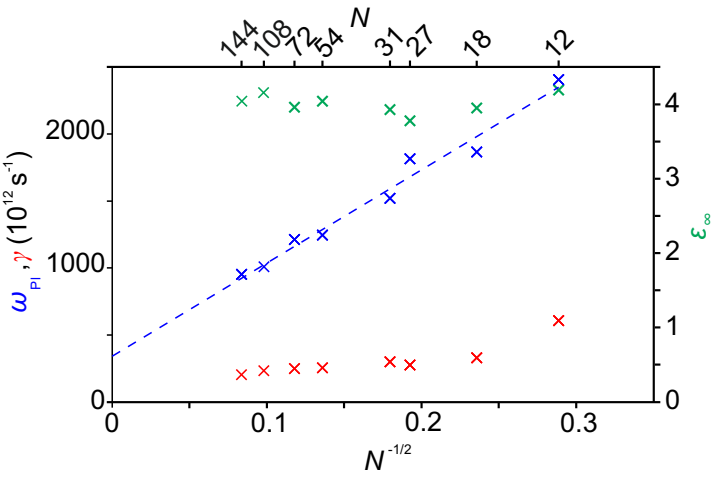

Figure 4.4: Drude paramters of Aluminum doped zinc oxide films doped to different degrees N. The plasma frequencies ω_{Pl} (blue), the damping frequency γ (red) and the background dielectric constant ϵ_∞ (green) were obtained from fits to reflection and transmission spectra as decribed in the main text. The dashed blue line is a linear fit to the plasma-frequency datapoints and intercepts the y-axis at $\omega_{\mathrm{Pl}} = 2\pi{\cdot}63{\cdot}10^{12}\,\mathrm{s}^{-1}$. Adapted from Reference [97].

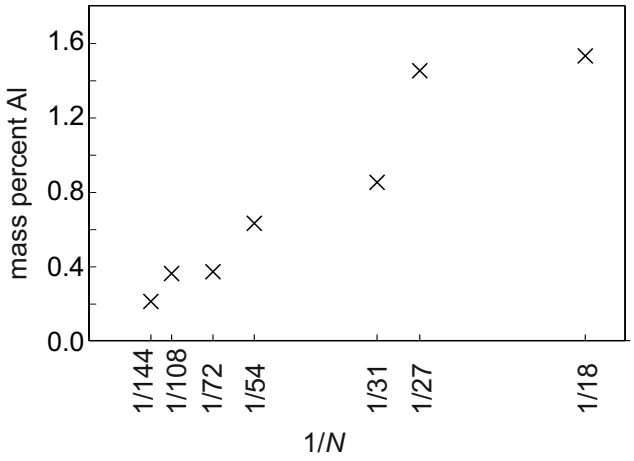

Figure 4.5: Aluminum content in doped zinc oxide films doped to different degrees N measured by EDX.

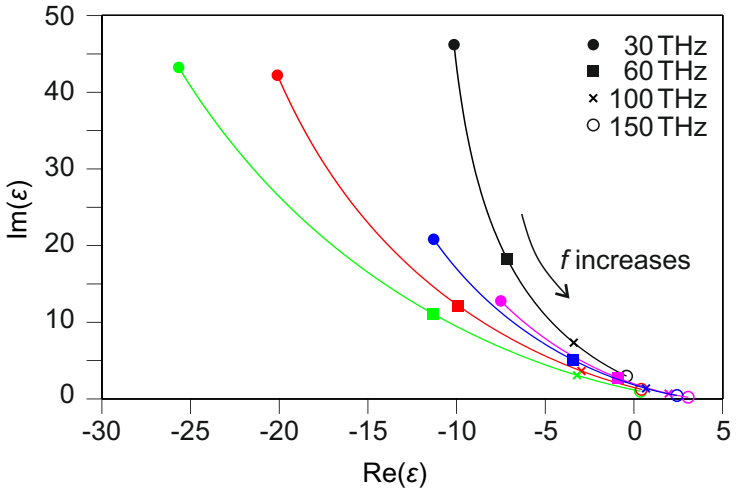

Figure 4.6: Range of permittivities accessible with doped ZnO for $12 \leq N \leq 144$. The frequency range considered is 30 THz to 150 THz. Each line corresponds to the permittivities achievable with one doping level between 30 THz and 150 THz. The end of the line in the lower right corner is 150 THz, the end in the upper left corner is 30 THz. The marks on the lines are at 30, 60, 100, and 150 THz (filled circles, squares, crosses and empty circles, respectively). The black, red, green, blue and magenta lines are for $N = 12, 18, 27, 72$, and 144, respectively.

4.4 So how well can we tailor the permittivity and what about nanofabrication?

4.4.1 Range of accesible permittivities

Figure 4.6 shows the range of permittivities which Aluminum doped ZnO can be tailored to by controlling N. In the frequency range between 30 THz and 150 THz the accesible permittivities span the range -25 to +3.

4.4.2 Nanofabrication

Smooth, thin, conformal coatings

The goal of depositing a tailorable metal has therefore clearly been achieved. In order to put this to use for applications such as the ones outlined in Chapters 2 and 3 it is also necessary to have a capacity to structure it (in three dimensions preferably). We chose to grow doped ZnO by ALD for exactly this reason and as one can see in Figure 4.7 it is indeed possible to conformally coat three-dimensional DLW polymer templates with AZO using our process. This Figure shows a focused-ion beam cut of a polymer woodpile that served as a test-template for three-dimensional film growth.

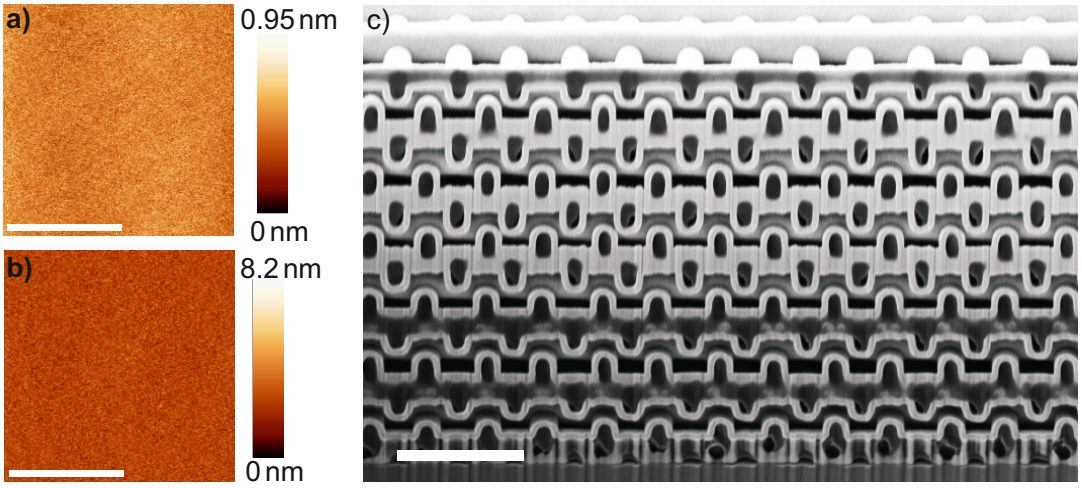

Figure 4.7: Smoothness and conformality of AZO films grown by ALD. a) a silicon wafer before deposition of 110 nm of AZO. The root-mean-square (rms) roughness is 0.11 nm. After deposition (b) the rms roughness increases to 0.59 nm, corresponding to a slight roughening only. c) A polymer woodpile template made by direct laser writing is conformally coated with AZO. The scale bars in a,b, and c are 5 µm, 5 µm, and 2 µm, respectively.

The viewing angle is 54°. The variation of the AZO film thickness on the polymer between the bottom and the top is too small to be determined from the FIB-cut, indicating that it is less than the pixel size of 2.5 nm. The woodpile photonic crystal shown there has been coated with AZO starting at a substrate temperature of 110°C in order to avoid melting of the polymer. The temperature can be raised once that 30 nm of material have been grown and stabilize the template. It is also possible to replace the initial stabilizing layer by a dielectric such as Al_2O_3, ZnO or TiO_2. These materials can all be grown by ALD at 110°C and have refractive indices on the order of 1.6, 1.9, and 2.3 in the infrared, respectively. Figure 4.7 also shows an AFM image of a silicon wafer coated with AZO in the same deposition run as the woodpile. The root-mean-square roughness is only slightly increased to 0.59 nm with respect to the silicon wafer before deposition 0.11 nm, despite the film having a thickness of 110 nm. This is an especially important property if one is interested in growing layered systems, as high-quality, smooth interfaces should be achievable.

Effect of heat

In combination with templating approaches based on polymer templates it may be desirable to remove the polymer after coating. This is, however, not straightforwardly possible by a simple calcination step as it is employed in usual single- and double-inversion procedures [15, 35, 37, 43] for two reasons: First, upon heating to 420°C for 12 hours AZO films develop severe cracks, even if heated up at a rate of only

0.5°C/min. Most likely this results from the different thermal expansions that the glass substrate and the AZO-film undergo and might be alleviated by a different choice of substrate.[2] Secondly, the AZO films dramatically change their permittivity upon heating as well. Figure 4.8 shows transmittance and reflectance spectra of a polymer-woodpile conformally coated with AZO. As expected from the metal-like properties of AZO in this wavelength range, there is close to no transmission. After opening the AZO-polymer composite with a reactive-ion-etching process described below and calcination of the polymer as described above, high, pronounced transmission of the AZO-air-inverse woodpile is evident in the infrared. This indicates that the material that was originally grown as AZO now has a dielectric-like response to light. It is referred to as "heated AZO" in the Figure. In order to verify that this change in the spectra is really related to the material, and not to other process steps, I have further processed this sample. First, I have filled the heated AZO/air composite with silicon by CVD. I then removed the heated AZO from the structure and redeposited AZO of the same doping level into the structure. The spectra of the two different silicon-AZO composites are shown in Figure 4.8c) and e), respectively. There is a clear distinction of the two spectra. Most notably, the reflection in Figure 4.8e) increases towards low frequencies and the transmission is suppressed to below 0.3% over almost the entire spectral range, consistent with what one expect for a photonic crystal in a metal-like background. The spectra of the silicon-air woodpile and the heated AZO-air woodpile are conform to a well ordered, dielectric photonic crystal, ruling out structural defects as the cause for the transition seen between panels a) and b) of Figure 4.8. I therefore conclude that AZO of a doping level $N = 18$ undergoes a transition from a metal-like phase to a dielectric-like phase upon heat treatment at 420°C in air. A possible reason for this is a thermally activated formation of spinel or a demixing process: The aluminum dopants in the AZO-films are not distributed homogeneously but in a layered fashion where aluminum atoms sit comparably close to each other. One would expect this from the way the films were grown and it has been shown in Reference [102, 103]. A thermally driven transition towards a phase mixture of Al_2O_3-clusters or the above-mentioned spinel in a ZnO background matrix seems possible. [98] Boltasseva *et al.*, have seen a phenomenologically similar phenomenon when attempting to improve the damping of AZO films grown by pulsed laser deposition on sapphire substrates by an annealing step. [57] In independent experiments aiming at the same goal I have tested the influence of the atmosphere present during the heat treament, but I was not able to improve the damping, regardless of the annealing conditions. Under ambient air, forming gas and in vacuum I was never able to produce a reduction in the damping frequency of the AZO films.

[2] Optimally, this substrate should be compatible with direct-laser-writing. The recently developed technique of dip-in direct laser writing allows for the usage of even opaque substrates in DLW, so this is not a very hard condition.

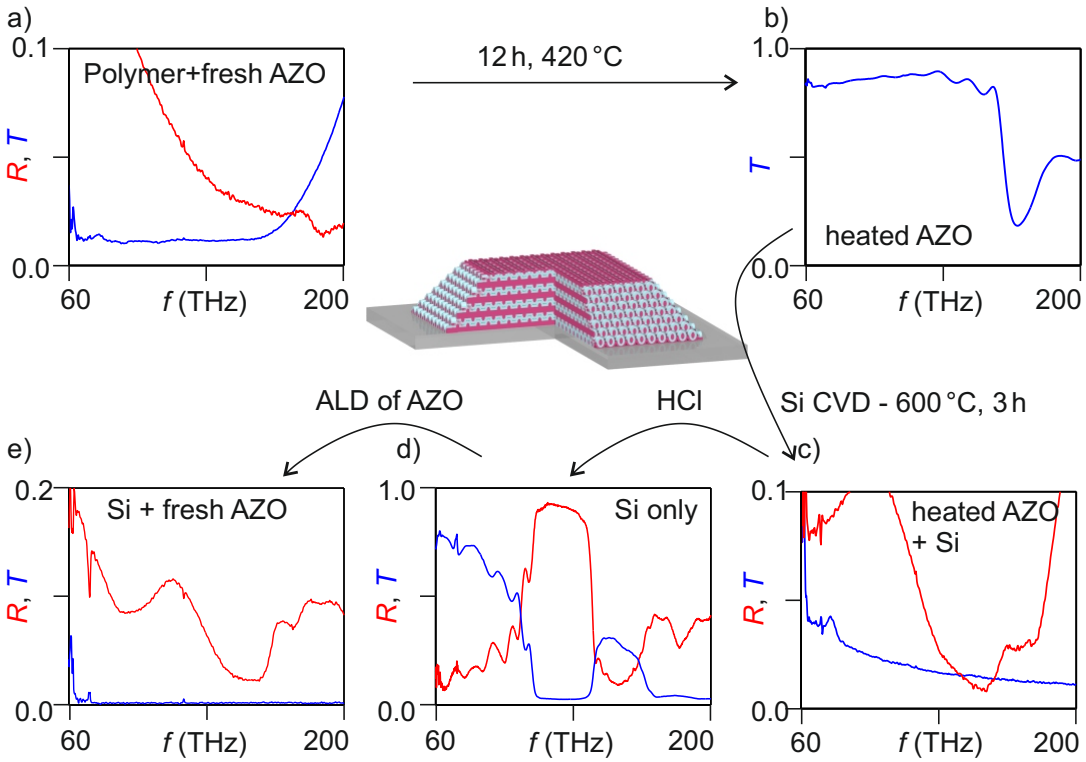

Figure 4.8: FTIR spectra of one sample in different conditions as described in the main text. a) Polymer-woodpile/AZO composite. b)AZO inverse woodpile after heating to 420°C to remove the polymer. c) as b but with air replaced by silicon. d) as c but with AZO removed. e) as d with the AZO regrown by ALD. The image in the middle shows a sketch of the sample. At the beginning the purple material corresponds to polymer, the blue material to freshly grown AZO. Note the different axis-scalings.

Subtractive processes for AZO

AZO can be grown onto polymer templates, glass, and silicon. What about inhibiting its growth or removing it selectively afterwards with the goal of patterning it? Since the DEZn-molecule that serves as one of the precursors for AZO-ALD is very reactive towards any hydroxyl adsorbates passivating a surface against growth of AZO is very challenging. Some success has been made by silanizing the substrate with a hydrophobic layer and patterning the layer. This approach was not followed here since a method to apply this method three-dimensionally was not available at that time. A recently developed photoactivation method that allows for locally defined surface functionalisation of an already developed photoresist using a laser beam might be suitable for applying such a passivation layer selectively, however. [104] Luckily it is possible to remove AZO directionally using the dry-etching technique of reactive ion etching (RIE). Commonly used etching procedures for ZnO use Argon as a sputtering species and chlorine based gas chemistries to contribute a chemical attack to the material. [105] The latter was not available at the beginning of this thesis so that I tried to adapt the RIE process to work without the chemical component on an Oxford Plasmalab 80 plus equipped with argon, oxygen, CHF_3 and SF_6 as etching gases. The best results are obtained under these circumstances with a flow of 10 sccm of Argon, at a pressure of 10 mTorr, and a plasma power of 200 W. These parameters result in an etch rate of 8 nm/min and a pronounced directionality, as can be seen in Figure 4.9b.

AZO can also be removed using a wet etch with 0.5% HCl. The etch process is very rapid and I was not able to measure the etching speed. This etch process is used in the novel titania double-inversion procedure described in Chapter 5 and in a new version of the previously published silicon double-inversion procedure [15,35,37] where ZnO replaces glass as an intermediate material. [106] This is very beneficial because of ZnO's higher resistance to thermal deformations during the polymer-calcination step employed in this procedure. This can also be seen by the spectra shown in Figure 4.9a. The transmission at the short wavelength side of the stopbands visible there recovers to more than 0.5. This is not the case if glass is used as an intermediate material. In this case the structures suffer from strong deformation during the heating step. This can also be seen by comparing the pictures of the photonic crystal waveguides shown in References [99] (glass) and [106] (zinc oxide).

Inversion and replication of polymer templates with AZO

As already mentioned above, it may be necessary for applications to to obtain a free-standing AZO-air composite derived from a three-dimensional polymer template. For this, the single- and double-inversion procedures for silicon cannot be applied. I have, however, devised a variation of these procedures that allows for an effective single- or double-inversion of a polymer-template into AZO. One key feature of the established single- and double-inversion procedures is the ability to selectively remove only one component from a three-dimensional, two-component composite. For

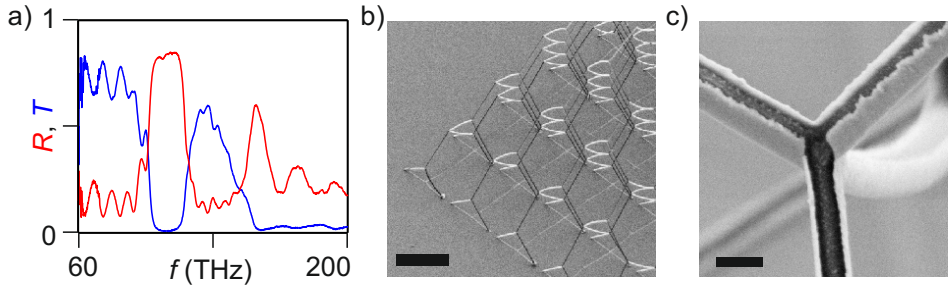

Figure 4.9: Nanofabrication with AZO: a) FTIR transmission and reflection spectra of a silicon woodpile produced by double-inversion using ZnO as an intermediate material. The features at high frequencies are not present if glass is used as an intermediate material. b) AZO can be removed directionally using an Argon-based sputtering process. The bright lines on the substrate are the areas where the 30 nm thick AZO-layer was shielded from the Argon bombardment by the polymer rod above it. The highest point which still shields the substrate from etching is 50 µm above the substrate. c) Close-up view of one of the coated polymer rods after the etching. Its diameter is 800 nm. From b) and c) the slope of a sidewall that this etching process would produce can be estimated as: $\Delta h/\Delta x = 50/0.8 = 62.5$. Scalebars in b) and c) are 20 µm and 1 µm, respectively.

the silicon double-inversion procedure, these material systems are polymer/glass and glass/silicon, where the removal is done selectively by heat in the former case and hydrofluoric acid in the latter case. In the silicon single-inversion case the composite consists of a polymer with a glass protective coating and silicon. The polymer is removed by a heat treatment. Zinc oxide and its doped versions are easily etched by hydrofluoric acid and all other acids I tested and a heat treatment cannot be applied as discussed above. Therefore neither the single- nor the double-inverson procedure can be applied to AZO straight-forwardly because of a lack of suitable intermediate material. It is possible to remove one material selectively from doped zinc oxide without needing to take recourse to an acid or heat, however: Silicon. It can be removed using an isotropic gas etch with XeF_2 which does not attack the zinc oxide. The spectra of XeF_2-treated AZO films are the same before and after the treatment. Thus, a polymer template can be replicated into AZO or inverted with AZO by combining silicon single- or double-inversion with AZO growth by ALD and a XeF_2 removal-step. This procedure is then an AZO single-inversion step based on a silicon template which is produced by silicon-single or double-inversion of the polymer-template.

Finally, I will answer the question in the heading of this section about how well we can tailor the permittivity and if AZO is a material that is amenable to nanofabrication: A number of techniques to fabricate nanostructures with AZO *via* ALD exist as I showed above. A variation of the aluminum content, allows for the tailoring of the plasma

frequencies of AZO films over more than one octave spanning plasma frequencies between nearly $2\pi \cdot 400 \cdot 10^{12}\,\mathrm{s}^{-1}$, *i.e.*, the red end of the visible spectrum, and $2\pi \cdot 152 \cdot 10^{12}\,\mathrm{s}^{-1}$, corresponding to a wavelength of 2 µm. At a frequency of 100 THz, the range of permittivities that can be reached with AZO then covers the interval $\epsilon = 1.95$ to $\epsilon = 3.40$. At lower frequencies, this range gets even bigger.

5 Titania double-inversion for photonic crystals

In Chapter 2 we have seen what is necessary for the creation of three-dimensional photonic crystals with a complete photonic bandgap in the visible part of the electromagnetic spectrum: It is necessary to arrange a high refractive-index material periodically in three dimensions. We have also seen in Chapter 3 that STED-DLW allows for the creation of three-dimensional templates and that ALD is a method to conformally deposit materials such as titania (TiO_2) and zinc oxide (ZnO) on such templates. In this chapter we will see how STED-DLW and ALD can be combined with dry- and wet-etch steps to create a TiO_2-almost-replica of a polymer template. The double-inversion (D) fabrication principle employed here has largely been used before to replicate polymer templates into silicon [15,35,37]. Due to the different final material, none of the process steps from that procedure are suited directly for titania DI, however. The cause of this is the need to be able to selectively remove one material from a composite of two materials twice during the procedure. This way, a different final material requires a different intermediate material and thus a completely new materials chemistry. I will refrain from detailing the reasons why the different process steps known from silicon DI cannot be transfered to titania DI and will instead focus on describing the solutions and will only treat the problems to the degree in which this is useful for understanding the necessity of the individual steps and measures.

Under the constraints of the used fabrication steps, the resulting TiO_2-structure is not an exact replication of the geometry defined using STED-DLW. I will therefore discuss how to account for the deviations in the design, optimisation and fabrication of the aimed-at complete photonic bandgap photonic crystals.

5.1 The double-inversion fabrication method and its implications for the design and fabrication of woodpile photonic crystals

5.1.1 The double-inversion concept

The principle of double-inversion used in this thesis has in large parts been used in the recent [15, 35, 37] and also in the distant past. To briefly illustrate, we look at the method for creation of a bell: Forming a metal directly in form of a bell has not been feasible in the past. Therefore a template is first defined in the form of clay and then confined in a shell enclosing it completely and tightly, thus replicating its

form. In making a bell, the template is then destroyed, resulting in a negative of the bell-template in the form of void space in the background material. This negative is infiltrated with molten metal and after cooling and solidifaction of the metal an exact replica of the initial clay-template is obtained.

Our approach towards the creation of TiO_2-woodpiles is somewhat similar: First, a template is made by STED-DLW. Secondly, a negative of this template is made by tightly and completely enclosing the polymer with ZnO by ALD and either filling or sealing all void spaces. Thirdly, a selective removal of the polymer from this composite yields a negative of the polymer template. Then, fourthly, TiO_2 is conformally deposited inside the negative by ALD. Finally, another selective removal step (of the ZnO this time) yields a TiO_2-almost-replica of the original template.

I will now look at the details of this process, show its inherent limitations and discuss how to account for them in the design and optimisation of the final geometry of the TiO_2-woodpile. At this point we will see that the double-inversion procedure outlined above is not able to produce a complete photonic bandgap using just the simple process outlined above but that it can be improved to achieve this goal. Finally, I will describe how the improved double-inversion procedure is implemented.

5.1.2 Limitations of inversion by ALD

STED-DLW yields a woodpile template that should ideally resemble what is shown in Figure 5.1a. The ZnO-air-matrix resulting from inversion of the polymer template is coated conformally with TiO_2, starting from the ZnO-air-interface. Since the woodpile consists of interpenetrating polymer rods, this interface does not have a cylindric shape. For the following considerations it is sufficient to think of it as a diameter-modulated cylinder. Since the TiO_2-coating *via* ALD grows conformally, it will stop once that the narrowest cross-section of the cylinder seals off the flow of precursors to the inside of the template. This is called pinch-off and is illustrated in Figure 5.1b for the case of the aforementioned diameter modulated cylinder. The air filled spaces that were originally occupied by massive polymer will thus not be filled with massive TiO_2 but will be a TiO_2-shell containing small inclusions of air once that pinch-off has occured. These inclusions will need to be accounted for in the design and optimisation of the woodpile.

In an ideal case the shape and size of the air inclusion could be deduced from the polymer geometry. In reality, however, it is determined by two other limiting factors. The first is related to the practically achievable conformality: Growth of TiO_2 can only occur as long as the precursor gases have access to the inside of the ZnO-Matrix that the TiO_2 is being grown into. Therefore any deviation of the ALD process from perfect conformality that results in a higher growth rate at the entrance of the pores will result in larger air inclusions than those dictated by the polymer template's geometry. Secondly, deviations of the polymer or ZnO template from the ideal geometry depicted in Figure 5.1a tend to lead to larger air inclusions as well. This is the case if either the rod's cross-section in Figure 5.1 is smaller than in the ideal case at *any one point* along the length of the rod or if the shape of the rods composing the woodpile deviates

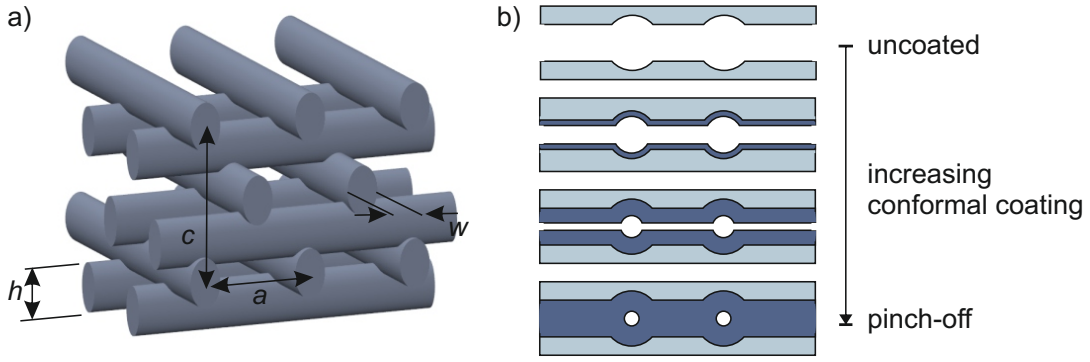

Figure 5.1: a) Sketch of the usually considered "ideal" of a woodpile. STED-DLW allows for the fabrication of polymer templates that closely resemble this geometry. Double-inversion of such a template using a conformal coating process such as ALD will result in an object whose exterior surface resembles the original polymer template. Its inside will contain air inclusions due to a pinching-off of the precursor flow even in the ideal case. Illustrated in b).

from a cylinder. The latter effect especially occurs at the region where 2 rods cross and overlap. Here, some regions are passed by the writing laser focus twice and some broadening of the polymer line occurs due to an effect called proximity effect.

These two limiting factors, will in the end lead to a fraction f of the volume occupied by TiO_2 in the "ideal" woodpile to be occupied by air. As detailed above, f should be expected to be determined by the sample's imperfections rather than its design. We therefore decided to empirically estimate f from test-samples. Figure 5.2 shows a focused-ion-beam cut of such a test-sample. From this we deduced f to be of the order 10 % for a woodpile with the structural parameters $a = 310\,\text{nm}$, $c = 369\,\text{nm}$, $w = 121\,\text{nm}$, and $h = 200\,\text{nm}$.

5.1.3 Implications for bandstructure calculations and design

In the past an effective medium approach has been applied successfully to treat the air inclusions in silicon woodpiles made by double-inversion [15,43]. In this approach, the rods composing the woodpile are treated as being made of a homogeneous material that has an effective permittivity ϵ_{eff}. This is reduced with respect to the bulk-permittivity of the double-inversion material, titania in our case, according to

$$\epsilon_{\text{eff}}(f) = f \cdot \epsilon_{\text{air}} + (1 - f) \cdot \epsilon_{\text{TiO}_2}\,, \tag{5.1}$$

where ϵ_{eff}, ϵ_{air} and ϵ_{TiO_2} are the effective permittivity, the permittivity of vacuum and the permittivity of TiO_2, respectively. This approach has also been examined systematically in Reference [107] and been found to adequately describe the impact

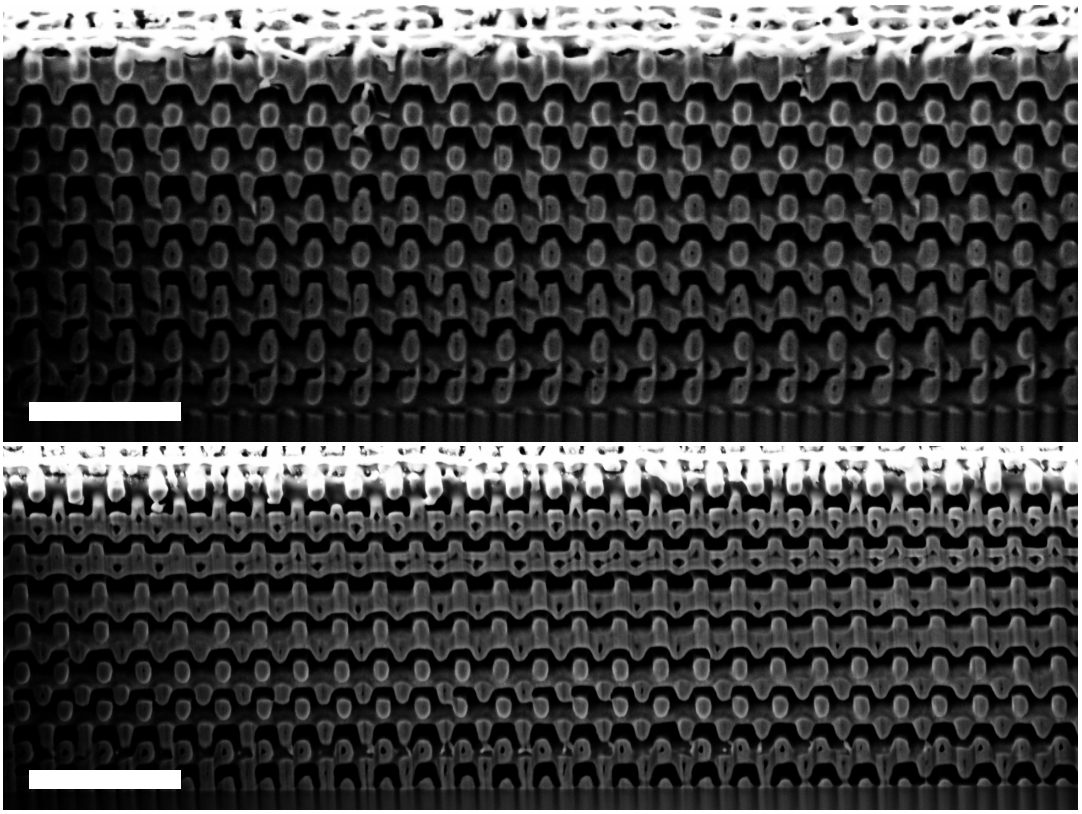

Figure 5.2: Two focussed ion beam (FIB) cuts of a double-inverted woodpile. The cutting planes are approximately parallel and less than 1 µm seperated from each other. They cut those rods that are perpendicular to the cutting plane in different locations of the unit cell. Some voids are visible and their estimated filling fraction is 15 %. Notice that the cutting planes are not exactly perpendicular to the substrate. Scalebars in both images are 1 µm.

of the air inclusions on the size and position of the complete photonic bandgap[1]. We therefore decided to follow the same approach.

Figure 5.3a shows a gapmap, *i.e.*, the size of the complete photonic bandgap for different geometric parameters of the woodpile for a given effective rod-permittivity. Every data point in this plot corresponds to the size of the complete photonic bandgap in a bandstructure for one set of parameters. For the bandstructure calculations I used the MPB software package, see Chapter 2 for details. In this case, the rod-width w and rod aspect-ratio h/w are varied with the other geometric parameters fixed at $a = 310\,\mathrm{nm}$ and $c = 416\,\mathrm{nm}$. As can be seen from this, the woodpiles do not possess a

[1]The crystal examined in the mentioned article is a diamond derived photonic crystal, but no woodpile. Also, the voids considered have a regular, well define shape that is the same for every unit cell, *i.e.*, the lattice-discrete translational symmetry of the crystal is maintained.

photonic bandgap for a lot of parameters and the largest attainable bandgap has a size of 2.8 % (where the size is again measured as gap-to-midgap ratio, *i.e.*, the ratio of the gapsize to the gap center-frequency). These values correspond to an ideal woodpile in the framework of the effective medium approach. The actually fabricated samples will be real woodpiles of finite size and they will contain imperfections. Those may lead to a reduced effective gapsize. I therefore aimed at woodpiles with an as big as possible complete photonic bandgap in the visible part of the spectrum.

Looking at the data shown in Figure 5.3a we see that for an effective permittivity of 5.51 woodpiles with complete bandgaps appear only if we either reduce the rod diameter w or the rod aspect ratio beyond 120 nm and 1.6, respectively. These two numbers essentially represent the practical limit of what is currently achievable with STED-DLW and are marked by the circle in Figure 5.3a. Luckily, it is possible to reduce the rod diameter of the final TiO_2-woodpile by conformally coating the ZnO-inverse of the polymer template with ZnO before the start of the TiO_2-deposition. As outlined above this will not change the size of the air inclusions and will further increase the filling fraction f, *i.e.*, reduce the effective index of the rods. We should therefore expect a trade-off between reduced rod-size and effective rod permittivity. Figure 5.3b-d shows gapmaps covering the same geometrical parameter space already shown in Figure 5.3a but for different, lower effective rod permittivities corresponding to different amounts of reinfiltrated ZnO. As we can see, there are configurations for which the final TiO_2-woodpile has a complete photonic bandgap in the visible.

In order to use the ZnO reinfiltration step to improve the gapsize it is necessary to know the dimensions of the template at the start of the procedure. The reason for this is that this step has both advantageous and detrimental effects: There is a trade-off between the effective rod permittivity and rod aspect-ratio one one side and the rod-diameter on the other side. The rod permittivity should be kept as high as possible and the aspect-ratio should be kept as low as possible while a decreased rod-width w intially increases the gapsize. ZnO-reinfiltration is reducing the rod-width but lowers the effective permittivity and increases the aspect-ratio. Figure 5.3 illustrates this: Following the line indicating the geometrical parameters of the polymer template, we see that the gapsize is increased upon reinfiltration with up to 8.5 nm of ZnO but that it decreases again if 12 nm are reinfiltrated. In addition to the need to know the dimensions of the polymer rods, one also needs to know the axial lattice constant c which also enters the gapmaps shown in Figure 5.3.

5.1.4 Non-destructive determination of woodpile dimensions

The parameters of the polymer template can – after some iterative learning and tuning of the DLW parameters – be tailored with some certainty during the direct laser writing process, see Chapter 3 for general details.To achieve this learning we produced a series of polymer templates of which we took FTIR transmittance and reflectance spectra. After this, the samples were single-inverted with doped ZnO, cut open with

a focused ion beam (FIB) and examined with a scanning electron microscope.[2] Using these images I could roughly link the transmittance and reflectance spectra to classes of geometrical parameters. I then used this as a reference to estimate the geometry of future polymer templates from their FTIR spectra without having to destroy them by FIB cutting. Also, we always produced polymer templates in a series of varied power of the writing laser. This way, every series contained polymer templates with spectra similar to those of already produced samples. Additionally, we always produced two nominally identical polymer templates to be able to cut one of them open if need-be.

5.2 Implementation of the titania double-inversion

In this section I will discuss the implementation of the concepts described so far: The principles for double-inversion and direct laser writing were already introduced. I will first line out the fabrication-hurdles that have to be overcome with the samples we were interested in. What is different about them with respect to samples that have already been discussed in the literature are two things: They have a very large footprint, a high polymer filling-fraction, and small feature sizes simultaneously. All this results in a long writing time for the polymer template. Also, since we aim at structures with an optical functionality, the required precision is higher than for, *e.g.*, structures that are produced by DLW for application as a mechanical metamaterial. This increases the sensitivity to mechanical drifts of the DLW-setup. In the subsequent double-inversion procedure the main challenge is to maintain as high a degree of conformality as possible.

5.2.1 DLW of large samples and for long writing times

Writing strategy

The most straight forward strategy for writing a woodpile with DLW is to write it in a layer-by-layer fashion. In every layer one would write the single rods one after the other, *i.e.*, one would move the piezo stage along the path shown in Figure 5.4c on the top. During this movement one would switch on the writing laser for those parts of the path shown in red. However, we found that this leads to a pairing-up of the individual rods both on the top of the woodpile as well as in the bulk, as can be seen in the FIB-cuts in Figure 5.4a and b. If such a superstructure is introduced into the crystals, they are no longer invariant under translations along the fcc basis-vectors discussed in Chapter 2. Effects related to such a superstructure have been discussed for woodpile photonic crystals in Reference [34]. Here, it is unwanted. Changing the writing pattern to the one shown at the bottom of panel c) this effect does not occur any more. For the surface of the woodpile this is evident in Figure 5.4d). The

[2] The single-inversion has the purpose of stabilising the sample against damage induced by the focused ion beam. When cutting polymer samples produced by STED-DLW with a FIB, deformations can otherwise occur, that would falsify the information contained in the images.

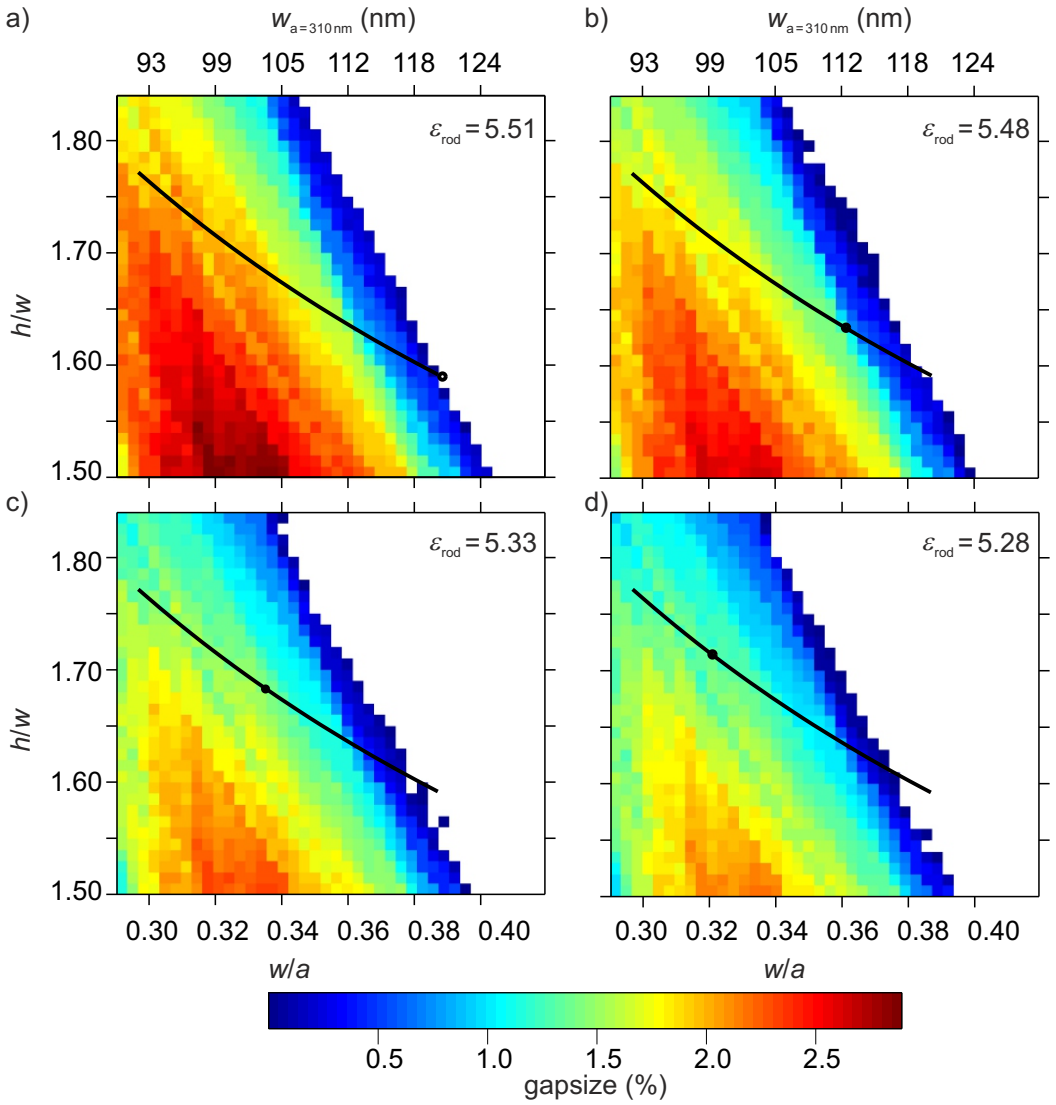

Figure 5.3: Gapsizes of the complete photonic bandgap for woodpile photonic crystals with dimensions as given by the axes. The rod diameter is measured in units of the rod distance $a = 310\,\text{nm}$ and is indicated in nm at the top scale. The axial lattice constant is $c = 416\,\text{nm}$. White color corresponds to no photonic bandgap. Panels a) through d) correspond to the effective rod permittivities as indicated. a) A double-inverted woodpile derived from a polymer template with $w = 120\,\text{nm}$ and $w/h = 1.6$ with a 12.5% air filling fraction f without the ZnO-reinfiltration. This woodpile will change its final dimensions as indicated by the line if the ZnO-reinfiltration-technique discussed in the text is used during the double-inversion. Also, it will have the dimensions indicated by the dot after infiltration with a) 0 nm, b) 4 nm, c) 8.5 nm, and d) 12.5 nm of ZnO. The permittivities in panels a) through d) correspond to the air filling fractions obtained for these ZnO thicknesses. Adapted from Reference [108].

FIB-cuts of the double-inverted woodpiles shown in Chapter 6 show that it is also absent in the bulk of the woodpiles.

Footprint-related issues

The woodpile samples we aimed at producing were supposed to measure 70 µm by 135 µm because they needed to have a sufficient footprint for the transmission measurements discussed in Chapter 6. In STED-DLW, a piezo-stage is used to move the sample with respect to the laser focus, see Figure 5.5a. It has a 200 µm by 200 µm field of movement along two perpenidcular axes of movement and 20 µm in the remaining direction. The two 200 µm axes define an x-y-plane that is nominally parallel to the glass-photoresist interface after taking a global tilt due to the mounting of the glass-substrate into account. The remaining direction is refered to as the z-direction and is ideally pointing along the optical axis of the system. The piezo has built-in capacitive sensors measuring the position of the stage with reference to the rigid body holding it and uses this to control its movement. However, we noticed that the displacement of the glass-photoresist interface is not rigidly linked to the displacement of the piezo-stage that is detected by the sensors. Using the piezo-stage to move the sample in the x-y-plane does not leave the distance of the laser focus and the glass-resist interface unchanged. Upon scanning the sample across the whole field of movement, the laser focus will instead change its position with respect to the interface by up to 150 nm in the z-direction. Since the interlayer distance $c/4$ in visible bandgap woodpiles is on the order of 100 nm, a fabrication error of this size is not a tolerable intolerance.

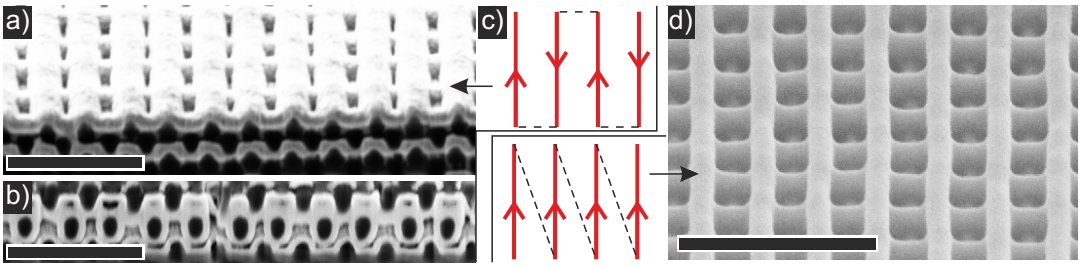

Figure 5.4: Writing strategy for woodpile photonic crystals. a,b) FIB-cuts of doped ZnO-coated polymer woodpiles written using the writing strategy shown at the top of panel c. They show that the rods form pairs both in the bulk and at the surface. This introduces an unwanted superstructure. The ZnO coating is the bright material in the pictures, the polymer is dark. c) Two writing strategies for woodpiles. The lines indicate the trajectory of the piezo-stage. The laser is switched on during those parts of the trajectory that are marked red. d) Using the writing strategy at the bottom of panel c), the superstrucutre is absent. Scalebars are 1 µm.

We mapped the relative displacement of the laser focus and the glass-photoresist interface along z that results from positioning the piezo at different points in the x-

$y-$-plane and found a reproducible deviation and a non-reproducible contribution, see Figure 5.5b, mostly likely due to temperature variations as discussed below. The reproducible deviation is most pronounced at the edges of the piezo's field of movement. To measure the data shown in Figure 5.5, we stepped the piezo-stage in the x-y-plane and scanned the piezo-stage in the z-direction along the optical axis following every step. The z-position for which the maximum reflection of the depletion laser from the interface occurred was denoted as the interface position. [10] We then chose to work on the area in which the deviation is smallest as indicated in Figure 5.5.

Another problem related to large footprint-samples is shrinkage of the polymer template during the development step. This step has been discussed in Chapter 3 in a general context. It is aggravated in large footprint samples however, since the forces developed upon shrinkage are sufficient to rip corners of the polymer-woodpile off the substrate. Using the camera and the microscope built into the DLW-setup it is possible to follow the development step. This way we were able to check that the structures are fine before development. Well attached structures are arrived at by silanizing the glass-substrates used for direct-laser-writing with 3-Methacryloxypropyltrimethoxysilane (3MPTS). Silanisation is a commonly known process. Not all of the procedures found in literature yield non-smeared, residue-free glass substrates that are compatible with high-resolution STED-DLW. Therefore, I have included the process I used for the silanisation in the appendix 1.

Issues related to mechanical drifts

A second class of problems that only arises in direct-laser-writing over long periods of time or for high-precision is related to the stability of the setup.

First, temperature has a direct effect on the size of the components employed in the setup. Since not all the materials employed have the same thermal expansion coefficient, the relative positions of the components are expected to change. Most notably this will lead to a displacement Δd of the laser focus with respect to the sample. On one hand, the sample is attached to a piezo-scanstage that is in turn attached to the top of a microscope. On the other hand, the microscope objective used to focus the laser beams is attached at the middle of the microscope. This means that the sample is held at a certain height h above the optical table by the metal the microscope housing is made of. The objective, is held at roughly half this height by half the amount of metal. A linear expansion Δl of the metal due to a temperature change ΔT should thus lead to a change of $\Delta d = c\Delta T \cdot h/2$, where c is the expansion coefficient of the metal. Indeed this is the case as can be seen in Figure 5.6. For these measurements, we measured the temperature of the microscope body and the air inside the laboratory over a period 42 hours. During this time we also tracked changes in the relative position of the glass-photoresist interface using the method already described above. The data in Figure 5.6 shows a correlation of the temperature of the microscope body with the changes in the interface position. The inset in Figure 5.6b reveals that substantial interface drifts also occur at a scale of less than 10 minutes. Eventually, we decided to account for these drifts in the writing

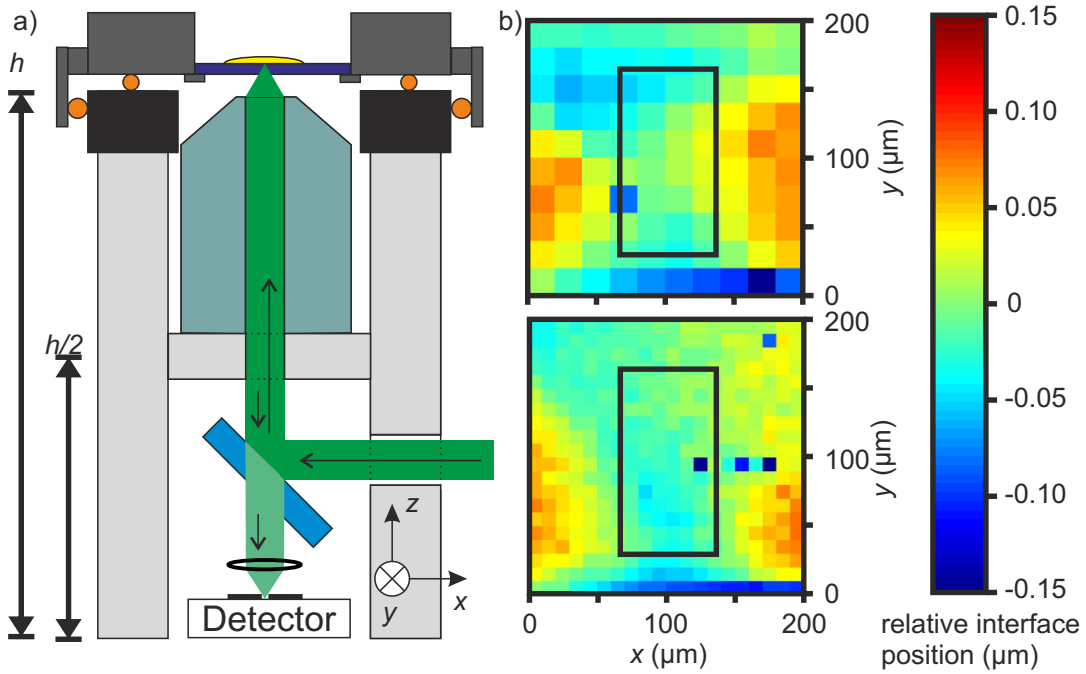

Figure 5.5: a) Schematic of those parts of the STED-DLW setup necessary to illustrate the effects discussed in section 5.2.1. The depletion laser beam (green) is focused by the microscope objective (grey-blue). It passes the immersion oil (not shown), the glass substrate (purple) and enters the photoresist (yellow). At the glass-resist interface some of the green light is reflected, crosses a partially transmitting element (blue) and is detected. The detector signal is at a maximum if the laser is focused at the interface. The microscope objective is held by the microscope body (gray). The body also holds a piezo-driven stage (black and dark gray). In this stage, piezoelectric crystals (orange) can be used to move the dark gray parts with respect to black parts in the x-, y-, and z-directions indicated. Inbuilt sensors are used to measure the position of the black and the dark grey parts of the piezo stage. b) Deviation of piezo displacement and interface displacement. The two measurements at the top and the bottom show the change of the interface's z-coordinate as a function of piezo-displacement in the x-y-plane. The top panel corrresponds to 20 µm steps, the bottom one to 10 µm stepwidth and to measurement durations of 15 minutes and 1 hour, respectively with correspondingly different impact of thermal drifts (see Figure 5.6). The interface's positon is determined as described in the main text, The rectangles show the footprint of a woodpile.

strategy by measuring the position of the interface after every ten written lines. This corresponds to an interval of on average 13.75 s. Without this measure, one woodpile can be written in four hours. Since searching the interface takes about nine seconds, the duration for the production of one woodpile is increased to about seven hours. One series of twelve woodpiles is then usually produced over the course of 54 hours.

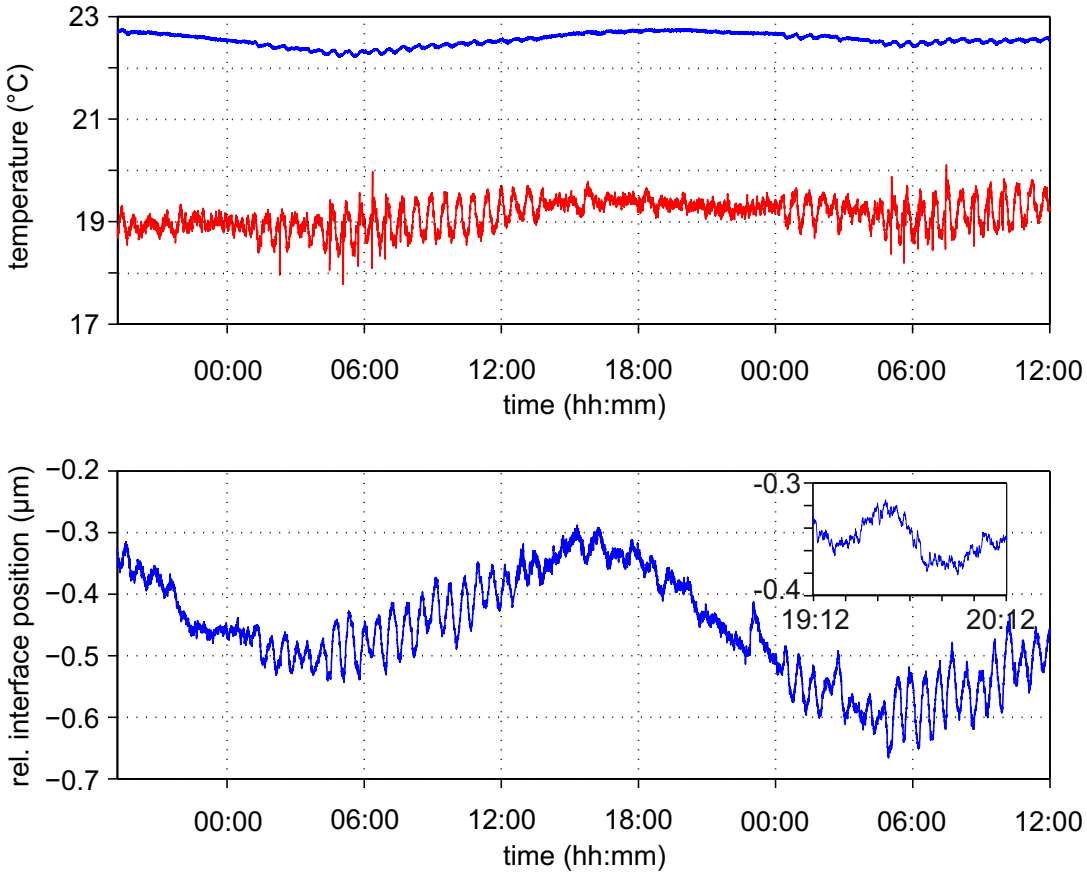

Figure 5.6: Drifts of the interface with respect to the laser focus. Top: Temperature of the writing microscope's body (blue) and the air above the optical table (red) recorded over a period of 42 hours. Bottom: Relative position of the interface and the depletions laser's focus measured over the same time. The drifts on the time scale of several hours are correlated to the microscope body's temperature. The inset shows one hour of drifts, revealing that drifts also occur on time scales that are a shorter than the time required to write one layer of a woodpile.

Over the course of 54 hours, a second effect becomes important: STED-DLW relies on a precise alignment of the excitation and the depletion focus. Since these two laser beams do not exactly follow the same beam path until they enter the microscope objective that creates the laser foci, drifts of the beam paths will lead to a misalignment

of the two foci and different effective doses. If the misalignment is known, it can be automatically corrected using a motorised mirror in the setup. The foci can be measured by three-dimensionally scanning a gold nano-bead through the focus and measuring the backscattered light. For details see Reference [10].

In order to automatically measure the alignment of the foci *during* the writing-process we deposited a PDMS piece with gold beads on one side next to the writing area. The gold beads are immobilized by the covering PDMS piece and also separated from the photoresist. This way they can be found reproducibly by simple translations of the sample stage and it is possible to realign the foci automatically.

5.2.2 Titania double-inversion

For a sample with a reliable estimate of the polymer geometry the double-inversion procedure into titania then follows the scheme depicted in Figure 5.7.

The fabrication starts with a polymer woodpile template made by STED-DLW. The templates had a footprint of 135 µm by 70 µm. It has a slightly tapered edge, meaning that the size of its top-surface is only 125 µm by 60 µm. This is illustrated (not to scale) in Figure 5.7. Its footprint was already discussed. The reason for the taper is the necessitiy that the top of the end of every polymer rod is exposed during the sputtering step used to open the ZnO coating. Without such a taper, a closed ZnO-layer would remain at the side-face of the ZnO-inverse woodpile made from the template. In this case, the inside of the inverse woodpile would only be accesible to gas-flow from the top-surface, leading to an unnecessarily early pinch-off.

The double-inversion procedure starts by coating the template conformally with ZnO until no gas flowpaths to its interior are present anymore. Due to the conformal nature of the ZnO-ALD process this ZnO-polymer composite is completely enclosed by a thin ZnO-layer. This layer needs to be opened in order to enable the selective removal of the enclosed polymer. The opening is performed by sputter-etching the sample in an Argon-Plasma in a reactive ion etching machine. After this step the polymer is exposed at the surface and at the edge of the woodpile. It can then be removed by heating the sample to 420 °C in an oven for 12 hours. During heating the glass-substrate expands by about 400 nm along the long side of the sample (135 µm) whereas an equal amount of ZnO only expands by about a third of this value, as calculated based on the data-sheet of the glass substrates and the data published in Reference [109]. Therefore, care in heating and cooling the sample needs to be taken here to minimize the impact of stresses that build up due to the different thermal expansion coefficients of ZnO, polymer and substrate.

The now air-filled ZnO-inverse of the polymer template is reinfiltrated with the desired ZnO-thickness at 110 °C substrate temperature. All other parts of the machine were also held at this temperature. The substrate temperature is intentionally chosen to be as low as possible to minimize the impact of the slow thermal DEZn-decomposition [80, 110] on the conformality of the ALD process. After this, TiO_2 can be grown into the diameter-reduced air channels in the ZnO backbone. This is done at 250 °C, with 110 s residence time of the precursors inside the ALD chamber and

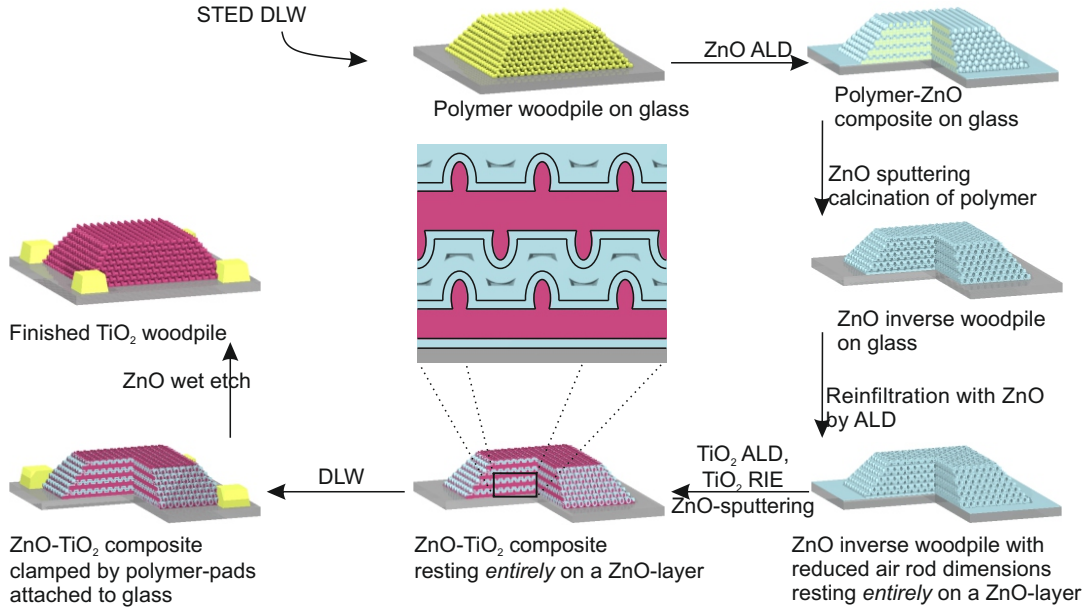

Figure 5.7: Titania double-inversion. First, a polymer template produced with STED-DLW is infiltrated with ZnO by ALD until pinch-off occurs. The resulting composite is enclosed with ZnO. The topmost layer of ZnO is removed *via* sputtering in an Ar-plasma. The polymer contained in the composite is exposed now and can be removed by calcination in air, resulting in a ZnO-inverse woodpile which is conformally reinfiltrated with ZnO to reduce the diameter of the air-rods. Following this, TiO_2 is grown conformally by ALD. The ZnO-TiO_2-layer enclosing the resulting ZnO-TiO_2-composite is removed by RIE of TiO_2 and subsequent sputtering of ZnO. At this point the ZnO-TiO_2-composite is resting entirely on a ZnO that was grown in the initial ZnO-inversion and the ZnO-infiltration. Therefore, a ZnO wet-etch would – at this point – result in detachment of the composite. To prevent this, the substrate is first silanzed once more. After this, rigid polymerpads can be defined on the glass-substrate. These are written such that they extend over the edge of the composite, thus clamping it to the glass substrate. Now, an HCl-etch removes the ZnO from the composite selectively, resulting in a double-inverted TiO_2-woodpile with smaller rods than the original polymer template. The zoom of the cut across the composite shows the ZnO (blue) that was reinfiltrated into the ZnO inverse woodpile (blue as well) and the TiO_2 (purple). The black line delimits the ZnO-films grown in the two ZnO-ALD steps. Adapted from Reference [108].

120 s of purge time. Since the air channels get narrower due to the ongoing deposition of TiO_2 their aspect ratio quickly approaches infinity. Therefore it would be desirable to also increase the residence time of the precursors inside the ALD chamber allowing more time for transport of the precursors into the channels. However, purge Argon-gas is continuously flowing into the chamber at a flow rate of 20 sccm while the precursors are held in the chamber, thus increasing the pressure inside the chamber. After approximately 110 s the O-Ring used to seal the chamber is not working reliably anymore due to a lack of compression. Also, longer residence times are not desirable for the thermal stability during the coating process since the increase in pressure increases the heat transfer from the heated substrate to the unheated cover of the ALD reactor. Within 110 s this effect amounts to a 4 °C temperature variation of the heated part of the body of the ALD reactor as measured by a thermocouple built into the outer part of the body.[3]

Since the ZnO grown during the reinfiltration covered those sites on the glass substrate that were originally occupied by the polymer woodpile, the TiO_2-woodpile grown by ALD will not be attached to the glass-substrate but rests on a thin ZnO-layer.

Once that the ZnO-reinfiltration and TiO_2-ALD are finished, the TiO_2-ZnO-composite is again enclosed in a TiO_2-ZnO-shell that needs to be removed before the ZnO-backbone can be removed selectively. TiO_2 can be etched directionally by employing a variation of a reactive ion etching process based on CHF_3 and Ar originally developed for the RIE of SiO_2 by Oxford Plasma Technology, Inc. The process uses a flow of 38 sccm argon, 12 sccm CHF_3, works at a pressure of 30 mTorr, and uses a forwarded power of 200 W. In this thesis an Oxford Plasmalab 80 plus was used. With this machine, the process left visible residues on the sample surface that could neither be removed by an Oxygen-plasma nor by a dip in piranha-solution. Changing from CHF_3 to SF_6 as the fluorine-providing species it was possible to etch the TiO_2 without residue. The etch rate was not entirely reproducible, but on the order of 20 nm/min.

To remove the layer of ZnO deposited on the glass during the reinfiltration, the same process as outlined above is employed. However, the ZnO-layer that the sample is resting on is not removed at the places where it is protected from the directional etching steps by the woodpile. Before it is removed together with the ZnO-backbone, the following step is introduced to prevent detachment of the TiO_2-woodpile and the glass-substrate due to dissolution of the ZnO-layer that connects them: After another silanisation of the samples, polymer pads adhering to the exposed glass-substrate and extending over the edge of the TiO_2-ZnO composite are produced by STED-DLW. These pads clamp the TiO_2-woodpile to the glass substrate even after the ZnO-Backbone has been removed.

As outlined above, we produced the woodpiles in series of varied writing parameters

[3] The remaining process parameters for the ZnO and TiO_2 ALD were as follows: 110 s exposure and 120 s purge time for the ZnO-ALD under a constant flow of 20 sccm argon. For the TiO_2 ALD, all reactor parts except for the substrate heater were heated to 150 °C. For the methods of precursor delivery see Chapter 3.

and sorted and processed them according to their estimated geometries. As there are usually several different woodpiles produced on a single glass substrate, this necessitated cutting the glass substrates into small pieces. Due to their small size, these pieces were not compatible with the STED-DLW setup anymore so that we had to glue the pieces upside down onto a 20 µm thick spacer on top of a regular glass substrate. We then infiltrated photoresist between the 2 glass pieces. This way, the woodpiles are close enough to the glass substrate that STED-DLW is possible.

Finally, the ZnO is removed from the TiO_2-ZnO-composite using a dip in 0.5% HCl for approximately 5 minutes.

6 A complete photonic bandgap material for visible light

In the last chapters I described how a combination of STED-DLW, ALD and selective etch processes can be used to fabricate a titania woodpile that, according to theory, should have a complete photonic bandgap. In this chapter, I will present one sample, named $FSL212_3$, that was obtained with this approach, describe the experiments I performed on it, compare the results to theoretical predictions and finally see that the experiments are in good agreement with the theoretical predictions for a complete photonic bandgap. In the end, we will therefore be able to confidently conclude to have produced the first photonic crystal with a complete photonic bandgap in the visible part of the electromagnetic spectrum. Another photonic crystal, named $FSL212_4$ was produced whose optical transmission spectrum suggests that it has a complete photonic bandgap and that it is almost identical to $FSL212_3$. Its spectra are shown in appendix 2. The proof that it has a complete photonic bandgap cannot be made without damaging it, which we decided not to do. Here, I therefore only discuss the sample $FSL212_3$.

6.1 Description of the sample

In this chapter I will discuss experiments on the photonic crystal $FSL212_3$ that has a complete photonic bandgap in the visible. Figure 6.1a,b shows optical micrographs of this crystal. The polymer pads used to attach it to the glass substrate are visible. In panel b, the site of the focused ion-beam (FIB) cut shown in panels c and d is visible as well. The FIB-cut will be discussed completely in connection with the theoretical modeling. Here, I would like to point out that the rod width is $w = 103\,\text{nm}$, and the rod height is $h = 174\,\text{nm}$, this means that the ZnO-reinfiltration changed the dimensions of this woodpile as indicated by the lines show in Figure 5.3. At this point I would also like to say that the crystal is homogeneous in the centre judged by the microscopy images and the FIB-cut. The woodpiles have intentionally been produced with a rectangular footprint of 70 µm by 135 µm such that they still have a projected cross-section of approximately 70 µm by 70 µm when tilted by 60 °as done during the optical experiments discussed below. However, as discussed in Chapter 5, the woodpiles have a tapered edge, resulting in an effectively useful footprint of 10 µm less in every direction.

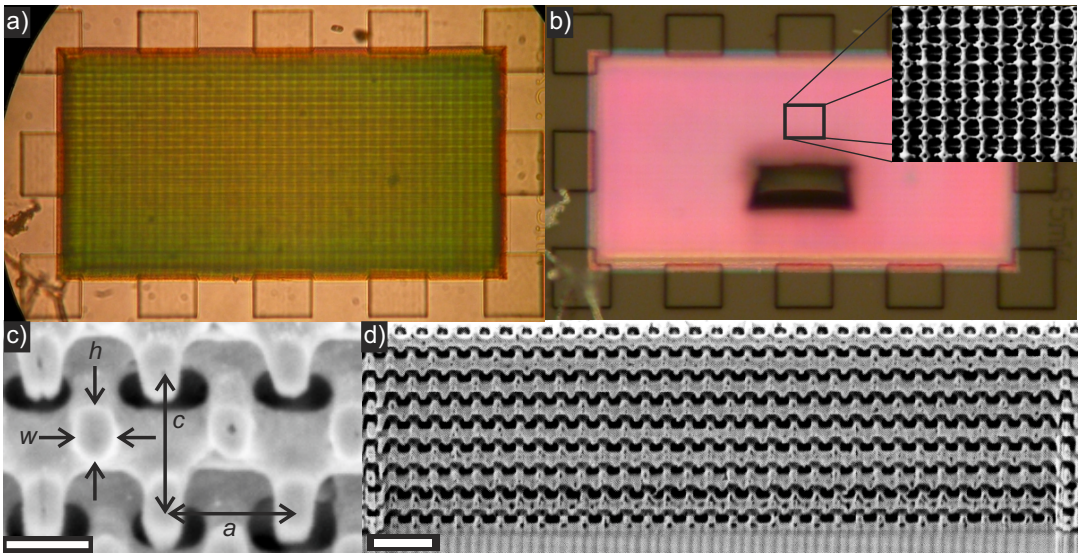

Figure 6.1: Sample FSL212$_3$. a) Optical micrograph of the sample in transmission. b) optical micrograph of the same sample in reflection. The site of the focused ion beam (FIB) cut shown in c),d) is visible. The inset shows the top surface of the woodpile. It is slightly damaged due to the dry-etching process but shows that the woodpile is terminated by rods parallel to its short side. c) Close-up of the titania rods in the woodpile. The rod distance $a = 310\,\text{nm}$, axial lattice constant $c = 416\,\text{nm}$, rod width $w = 103\,\text{nm}$, and the rod height $h = 174\,\text{nm}$ are indicated. The viewing angle is 54 °. d) overview of the cut surface. Scalebars in c) and d): 200 nm and 1 µm. Panels c and d are adapted from Reference [108].

6.2 Setup for angle- and polarisation-resolved transmission spectroscopy

As discussed in Chapter 2, a photonic crystal with a complete photonic bandgap will exhibit a vanishing transmission for incident light with frequencies inside the photonic bandgap irrespective of the angle of incidence and polarisation. I systematically screened all photonic crystals for this criterion using an adaption of a home-built setup originally built by Markus Deubel. [111] It is shown in Figure 6.2. In this setup, light from a glass fibre is collimated by lens L1, passed through a polarizer and collected by microscope objective O1 which focuses it on the sample which rests on a rotation stage. There is an aperture centered in front of the objective O1 that, when closed to the minimum open diameter, limits the spread of incidence angles of the light cone focused onto the sample to 5° half-opening angle. The transmitted light is collected by objective O2 and imaged by a second lens L2 onto an intermediate image plane. In this intermediate image plane there is an aperture A1. Using the kinematic mirror M2, the intermediate image plane can be imaged onto a camera using lenses L3 and

L5 in order to control the sample alignment and position of the aperture A1 with respect to the woodpile under consideration. If M2 is removed the light is collected by lens L4 and imaged onto a 200 µm core-diameter glass-fibre which guides it to an optical spectra analyzer (OSA).

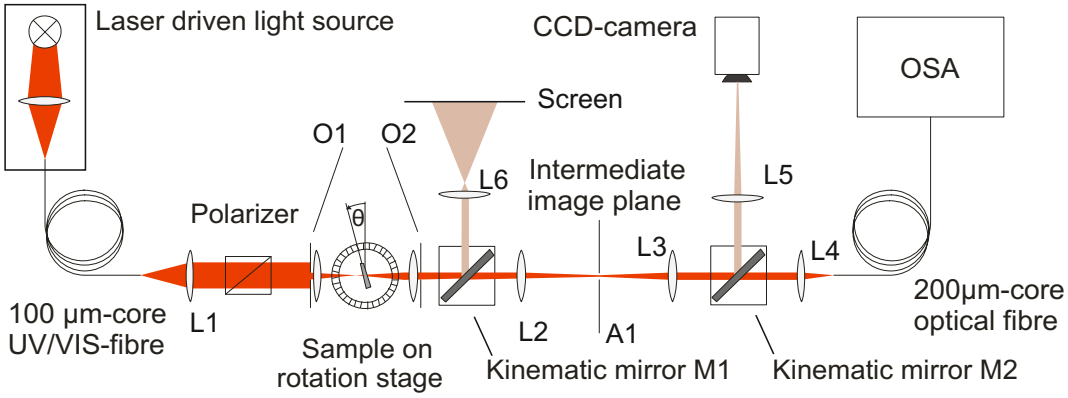

Figure 6.2: Setup for angle- and polarisation-resolved transmission spectroscopy on woodpile photonic crystals. L1: Lens, $f = 25.2\,\text{mm}$, Polarizer: Glan-Thompson polariser. O1, O2: Zeiss Achroplan LD 20x objectives, NA= 0.4, $f = 8\,\text{mm}$ with circular apertures attached. L2, L3: Lenses,$f = 150\,\text{mm}$. L4: Microscope objective lens, $f = 16.5\,\text{mm}$. L5: Lens, $f = 500\,\text{mm}$. L6: Lens, $f = 150\,\text{mm}$. A1: Rectangular knife-edge aperture. The effective numerical aperture of O1 can be reduced to 0.088 if the circular aperture in front of it is closed to its minimum diameter of 1.4 mm. Adapted from Reference [9].

Light passing the photonic crystal can undergo Bragg diffraction from the periodic lattice. In order to allow for a meaningful comparison with calculated spectra it is necessary to know which diffraction orders have been collected. After passing the objective O2 light that was diffracted will not be centered on the optical axis, but will propagate parallel to it. In order to collect only the undiffracted light the aperture behind objective O2 can be closed until only the central beam is collected. The presence of diffracted orders can be checked for by using the kinematic mirror M1. If this mirror is inserted into the setup, the diffracted orders can easily be discerned from the central beam on the screen after lens L6. The aperture of objective O2 can then be closed until they disappear.

As a light source, we used the plasma driven light source EQ99-FC by Energetiq, Inc.. In this light source, a plasma is struck inside a glass bulb containing Xenon and is then maintained *via* heating by a 20 W laser focused onto it. A sphere of approximately 100 µm radius is heated to 15000 K this way. The emission spectrum of the Xenon-plasma is approximately that of a 15000 K hot black body in the visible part of the spectrum with a correspondingly high spectral power density. Since a lot of light is lost in the setup due to the aperture in front of the first microscope

objective and due to the size of the sample investigated, the use of a high-brightness lamp was necessary to still be able to reliably detect the low transmission expected for light with frequencies inside the stopbands and the complete photonic bandgap. The minimum of transmission that we could reliably determine with this setup was $2 \cdot 10^{-4}$. The quality of the optical image obtained by the camera deteriorates for angles approaching 60 °. I therefore set a small enough aperture (approx. 20 µm by 20 µm) in the image plane to be sure to only measure the bulk of the photonic crystal and not its edges. All transmission spectra of woodpiles shown in the remainder of this chapter have been normalized to the transmission of the bare glass substrate at the same aperture, angle of incidence and polarisation.

6.3 Experimental results and comparison to theory

The middle column of Figure 6.3 shows the angle-resolved transmission spectra of the sample shown in Figure 6.1 for s- and p-polarisation for wavelengths between 500 nm and 850 nm on a colour scale. A pronounced suppression of transmission exists for all angles and polarisations. If one takes 1% as the minimum transmission that is compatible with the existence of a stopband for a certain angle of incidence, the measured overlap of all stopbands spans from 686.3 nm to 706.7 nm. This range is then the experimental upper boundary for the complete photonic bandgap we are looking for. The spectra which limit this range are those at 30 °and 60 °for p-polarised incident light. These are shown in the left column of Figure 6.3 together with the normal incidence spectra for s- and p-polarisation. Comparing the normal incidence spectra in s- and p-polarisation, we see that there is a marked difference of transmission for the two polarisations, in accordance with theory (see below). This is a further indicator of the high structural quality of the samples. Notably, the minimum observable transmission of $2{\cdot}10^{-4}$ is also reached for every angle of incidence and every polarisation.

Since our measurements cover neither all internal directions of propagation nor all external angles of incidence, we expect the complete photonic bandgap to be smaller than this experimental boundary. A comparison to theoretical predictions therefore seems necessary to convincingly establish the existence of a complete photonionc bandgap. The results of simulations performed by Thomas Zebrowski using the S-matrix code of Prof. Kurt Busch's group [112–115] are shown in the right colum of Figure 6.3. The basis for these calculations are the geometrical parameters of the woodpile, the measured refractive index of titania (see Chapter 3) and the void filling fraction (see Chapter 5). The calculations also take the dispersion of the real part of the titania refractive index into account. An imaginary part of the titania refractive index is taken into account as well, but in order to account for scattering from fabrication imperfections, it is taken heuristically as $\mathrm{Im}(n_{\mathrm{titania}}) = 7500\,\mathrm{nm}^2 * \lambda^{-2}$. Since the physical reason for incorporating this heuristic imaginary part of the refractive index is scattering, it might be surprising that we have chosen a λ^{-2}-dependence. Koenderik and Vos have, however, shown in Reference [116] that scattering from irregularities in photonic crystals follows this dependence, instead of the λ^{-4}-dependence expected

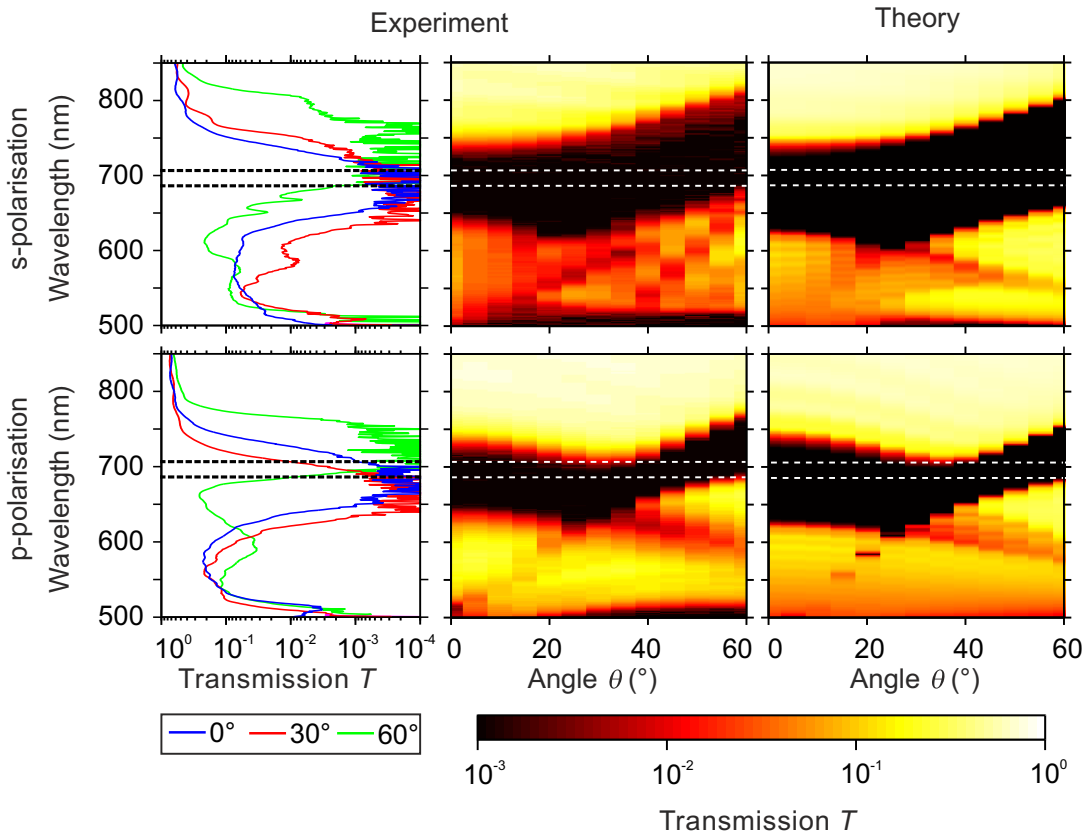

Figure 6.3: Angle- and polarisation-resolved transmission spectra of the woodpile photonic crystal shown in Figure 6.1. Left column: Line plots of the transmission for s- and p-polarised incident light (top and bottom, respectively) on a logarithmic scale. Middle column: Spectra for all angles and polarisations shown on a colour scale. Right column: Corresponding calculated spectra using the geometric parameters from the FIB cut and the measured material parameters of titania as described in the text. All colour plots are displayed using the same logarithmic colour scale which cuts off at $T = 10^{-3}$. The dashed lines delimit the wavelength interval in which $T < 1\%$ for all polarisations and angles of incidence. This interval is limited by the stopbands for p-polarisation under 30° and 60° angles of incidence.

from Rayleigh-scattering. The calculations also take the correct surface termination and number of layers (33 layers) in the stacking direction of the woodpile into account. The woodpile is considered to be infinitely extended in the lateral directions.

The geometrical parameters for the calculations are taken from the FIB cut as indicated in Figure 6.1: They are rod distance $a = 310\,\text{nm}$, axial lattice constant $c = 416\,\text{nm}$, rod width $w = 103\,\text{nm}$, and rod height $h = 174\,\text{nm}$, which agrees well

with the actual dimensions of the sample as this FIB-cut shows the rods at their points of narrowest cross-section. Since the theoretical prediction for the transmission and the experimental data match well, we are confident that these geometrical and optical parameters represent a good description of the woodpile. We are therefore confident that a photonic band structure calculation using the same parameters will also yield the actual photonic band structure of the woodpile we produced. This band structure is shown in Figure 6.4 together with the Brillouin zone for this particular case of the centered tetragonal geometry.

Using the software package MIT Photonic Bands (MPB), we can also compute the photonic density of states. To do this, we can approximate the density of states $\rho(\omega)$ by the number of states in a certain frequency interval as follows:

$$\begin{aligned}
\rho(\omega) &= \frac{\mathrm{d}n}{\mathrm{d}\omega} = \sum_i \frac{\mathrm{d}}{\mathrm{d}\omega} \int \mathrm{d}^3k \delta(\omega - \omega_{i,\boldsymbol{k}}) && (6.1)\\
&\approx \frac{\Delta n}{\Delta \omega} && (6.2)\\
&= \frac{1}{\Delta\omega} \sum_i \int \mathrm{d}^3k \Theta(\omega + \Delta\omega/2 - \omega_{i,\boldsymbol{k}}) \cdot \Theta(\omega_{i,\boldsymbol{k}} - \Delta\omega/2 - \omega) && (6.3)\\
&\approx \sum_i \sum_{\boldsymbol{k}} (\Delta k)^3 \Theta(\omega + \Delta\omega/2 - \omega_{i,\boldsymbol{k}}) \cdot \Theta(\omega_{i,\boldsymbol{k}} - \Delta\omega/2 - \omega) && (6.4)
\end{aligned}$$

Here, Δn is the number of states in the frequency interval $[\omega - \Delta\omega, \omega + \Delta\omega]$ and Δk is the volume element in reciprocal space over which the integral $\int \mathrm{d}^3k$ is discretized. For the density of states shown in Figure 6.4, the reciprocal space was discretized in 50 steps of size $\Delta k_x = \Delta k_y = 2\pi/(50 \cdot a_{\mathrm{fcc}})$ along the k_x- and k_y-direction and in 50 steps of size $\Delta k_z = 2\pi/(0.949 \cdot 50 \cdot a_{\mathrm{fcc}})$ along the k_z-direction to account for the compression of the lattice with respect to the fcc geometry that corresponds to the axial lattice constant of 416 nm. 32,830 points of this grid lie in the irreducible Brillouin zone. For these points, I computed all bands up to frequencies corresponding to 500 nm wavelength and used this data to evaluate equation 6.4. Since the volume of the irreducible Brillouin zone is is one 16^{th} of the volume of the whole Brillouin zone, this corresponds to a calculation for 381,280 points in the Brillouin zone.

The band structure calculations along the high-symmetry lines and the one on the whole Brillouin zone show that in the frequency range between 424 THz and 431 THz no modes of the electromagnetic field exist inside the photonic crystal. This frequency range, which corresponds to the wavelengths between 707 nm and 696 nm, is completely inside the visible part of the electromagnetic spectrum. Neither the website of the National Institute of Standards nor that of the Physikalisch-Technische Bundesanstalt give an official definition for the extent of visible spectrum that one could use to substantiate this claim. However, the visible spectrum is usually considered to extend up to wavelengths of 750 nm, sometimes even up to 780 nm. Wikipedia

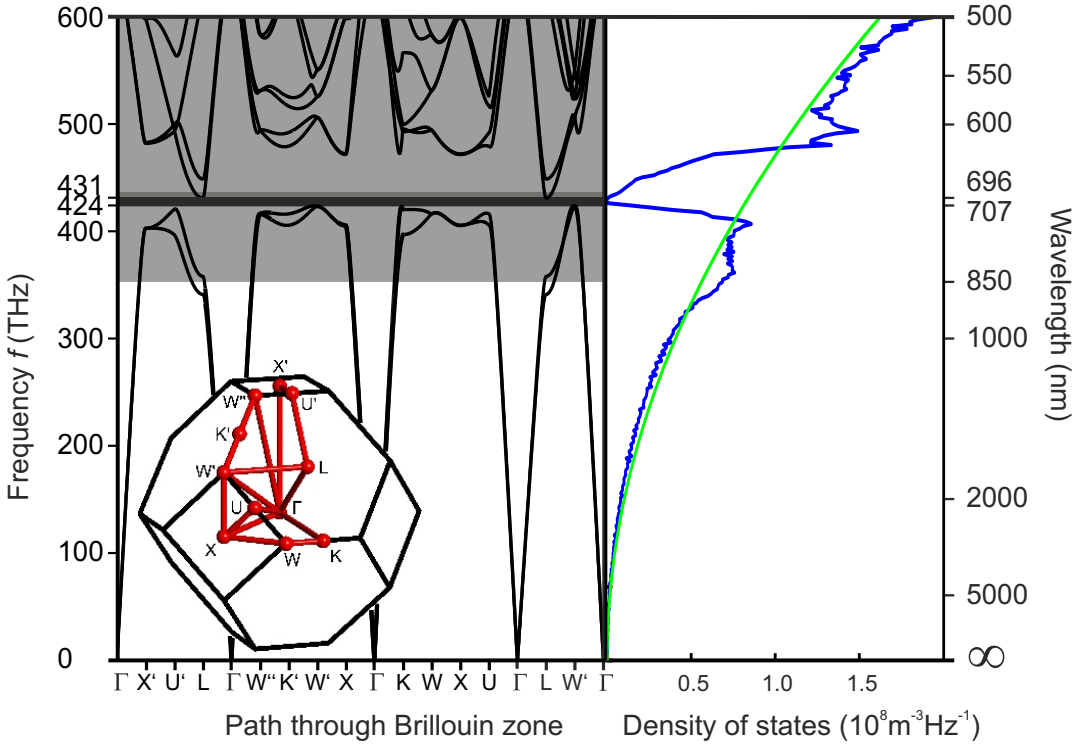

Figure 6.4: A complete photonic bandgap for visible light. Left: Section of the band structure of a woodpile along the path shown in the inset. The woodpile has the rod dimensions $w = 103\,\text{nm}$, and $h = 174\,\text{nm}$, a rod distance of $a = 310\,\text{nm}$ and an axial lattice constant of $c = 416\,\text{nm}$, *i.e.*, the dimensions taken from the FIB-cut in Figure 6.1c. The permittivity of the woodpile rods is $\epsilon = 5.33$, derived as discussed in the text from the measured properties of titania films grown under precisely the same conditions as those under which the woodpile was fabricated. Right: The photonic density of states of this photonic crystal (blue) and that in a bulk material with a permittivity of $\epsilon = 5.33$ (green) evaluated on a grid of 381,280 points in the Brillouin zone. As on the left side, the frequency region between 424 THz and 431 THz does not contain *any* modes. This interval corresponds to the wavelengths between 707 nm and 696 nm.

defines the colour red as belonging to the wavelength range 620 to 740 nm. Therefore, the woodpile $FSL212_3$

- that is considered in Figure 6.4,
- whose measured and calculated transmission agree well as shown in Figure 6.3,
- and SEM images of which are shown in Figure 6.1c,d, confirming the validity of the theoretical modelling,
- that looks homogeneous as judged by the visible light optical micrographs in Figure 6.1a,b, and
- that has been produced in a process thoroughly trimmed at the highest attainable precision and freedom from defects as discussed in Chapter 5, and
- whose rods are composed of titania whose permittivity is known from ellipsometry measurements on material grown during the same process that the woodpile was made with

is the first reported complete photonic bandgap material for visible light.

6.4 Outlook: Angle-resolved photon emission spectroscopy

In order to further test whether the description of this sample in terms of a photonic band structure is adequate, we can perform the following experiment using the setup shown in Figure 6.5: Here, the photonic crystal is irradiated with light from a continuous wave laser which excites emitters that happen to be embedded into it. The fluorescence is collected using the objective of an inverted microscope. If the photonic crystal is at the focus of the objective, the electric field distribution at the back focal plane for a given frequency is the fourier-transform of the wave-vector distribution before entering the objective and thus of the distribution of propagation directions, which we expect to be highly anisotropic due to the band structure. The lenses L1 and L2 create an image of the back focal plane at a plane outside of the inverted microscope. By scanning the end of a glass fiber across the image and detecting the light coupled into the fibre, it is possible to record the intensity distribution in the back focal plane. The spatial resolution is then given by the fiber's core diameter. If one uses a grating spectrometer with an attached CCD camera, it is even possible to do this for many frequencies simultaneously.[1]

[1] Another, long sought-after, hallmark of a complete photonic bandgap was the inhibition of spontaneous emission by an emitter or even a non-markovian radiative decay. In principle, these experiments can be performed with our photonic crystals as well. Since the gap is comparably small, however, the already stringent requirements for an emitter in such an experiment are aggravated by the additional requirement that its spectrum must be narrower than the size of the gap. Ruby, argon and the vapors of bromine and iodine have narrow emission lines in the spectral range of interest. Ruby could be introduced into the crystals as a nanoparticle or possibly even grown as a thin film by ALD. Unfortunately, the glass substrate the crystals rest fluoresces in a way that is undiscernible from the ruby fluorescence.

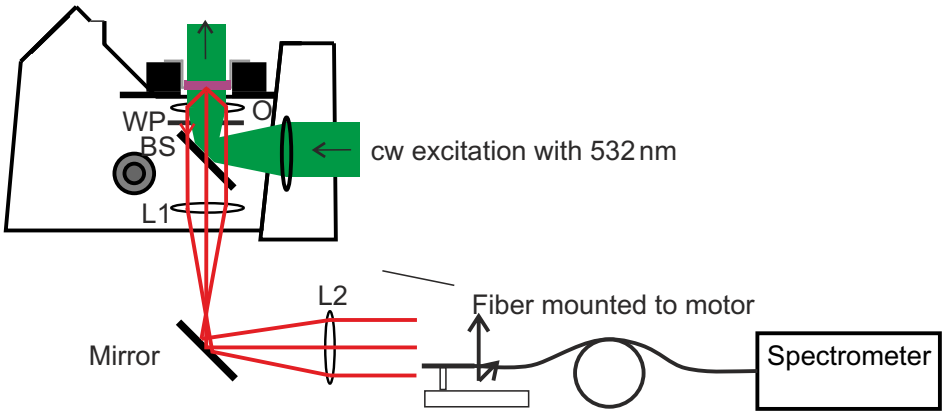

Figure 6.5: Setup for angle-resolved photon emission spectroscopy on photonic crystals. The sample (purple) is mounted on the stage of an inverted microscope in the focus of a microscope objective O with a numerical aperture of 1.4 and irradiated by a continuous wave, frequency-doubled Nd:YAG laser with a wavelength of 532 nm. The titania the rods are made of absorbs some of this light and undergoes fluorescence. The fluorescence spectrum of bulk titania is broad and redshifted with respect to the excitation laser. The excited titania then couples to regions of the band structure in which the shape of the isofrequency surfaces deviates strongly from a sphere, resulting in anisotropic emission. The fluorescence photons are collected with the microscope objective O. The tube lens L1 of the microscope and the lens L2 image the back focal plane of the objective into a plane in which it can be scanned with a fiber with a core diameter of 100 µm. The image of the back focal plane contains information about the direction of emission as described in the text. WP is a quarter wave plate that is installed in the microscope and BS is a beamsplitter.

As I will now show, the thus-recorded intensity distribution for a given frequency f is intimately connected to the band structure. Specifically, it is a measure of the projection of the isofrequency surface $\omega(\boldsymbol{k}) = 2\pi f$ onto the plane of wavevectors lying parallel to the glass-photonic-crystal interface. Consider an excited emitter in the photonic crystal with the emission frequency $f = \omega/2\pi$. It couples to Bloch modes of frequency f that have non-zero field strength at the location of the emitter. Both the photonic crystal and the homogeneous media (glass being the relevant case here) surrounding it are invariant under lattice translations that are parallel to the crystal-medium interface. The conserved quantity associated to this symmetry is the wavevector component $\boldsymbol{k}_{||}$ parallel to the interface (modulo reciprocal lattice vectors $\boldsymbol{G}$ that are parallel to the interface). We know therefore that for the frequency f, only those electromagnetic waves in the homogeneous media for which

$$\boldsymbol{k}_{\mathrm{B},\parallel} = \boldsymbol{k}_{\mathrm{glass},\parallel} = \sqrt{\left(\frac{2\pi n f}{c}\right)^2 - k_{z,\mathrm{glass}}^2} \tag{6.5}$$

holds can be excited by a Bloch mode. Here, n is the refractive index of the glass substrate, c is the speed of light in vacuum, $k_{z,\mathrm{glass}}$ is the wavevector component of the emitted light that is normal to glass interface and $\boldsymbol{k}_{\mathrm{B},\parallel}$, $\boldsymbol{k}_{\mathrm{glass},\parallel}$ are the wavevector components of the Bloch mode and the electromagnetic wave propagating in the glass, respectively. It is therefore possible to sample whether an excited Bloch mode with frequency f and wavevector component $\boldsymbol{k}_{\mathrm{B},\parallel}$ couples to an electromagnetic mode in the glass. This means to measure the projection of a cut of the band structure at frequency f (an isofrequency surface) onto the plane of wavevectors parallel to the interface. I will refer to this quantity as the projected band structure $p_{\omega=2\pi f}(\boldsymbol{k}_{\mathrm{B},\parallel})$. It can be written as

$$p_\omega(\boldsymbol{k}_{\mathrm{B},\parallel}) = \sum_j \int \mathrm{d}k_z \delta\left(\omega - \omega_j(\boldsymbol{k}_{\mathrm{B},\parallel}, \boldsymbol{k}_z)\right) \tag{6.6}$$

where the index j is the band index. The projected band structure is similar to the density of states, in that it gives the number of states having a certain frequency and a certain wavevector component $\boldsymbol{k}_{\mathrm{B},\parallel}$ parallel to the interface. In accordance with the definition in equation 6.6 it has the unit $\mathrm{Hz}^{-1}\mathrm{m}^{-1}$. One can compute $p_\omega(\boldsymbol{k}_{\mathrm{B},\parallel})$ from a dense discretisation of the band structure using the procedure described above for the density of states.

The method of measuring $p_\omega(\boldsymbol{k}_{\mathrm{B},\parallel})$ which I outline here has the following limitations:

1. Bloch modes with wavevectors for which $\boldsymbol{k}_{\mathrm{B},\parallel} > \frac{2\pi n f}{c}$ holds will not be able to excite propagating modes in the medium at the interface.

2. Without knowledge of the field distribution $\boldsymbol{H}_{j,\boldsymbol{k}}$ for a given mode it is not possible to say if a mode will couple to modes in the medium, even if $\boldsymbol{k}_{\mathrm{B},\parallel}$ can be conserved.

3. Points in the image of the back focal plane cannot be assigned unambiguously to $\boldsymbol{k}_{\mathrm{B},\parallel}$. It is only possible to assign them to $\boldsymbol{k}_{\mathrm{B},\parallel} \pm m\boldsymbol{G}$, where m is an arbitrary integer and $\boldsymbol{G}$ is a reciprocal lattice vector that is parallel to the interface.

The impact of the first point is easily calculated, that of the second point can in principle also be calculated. If this is not done, measuring $p_\omega(\boldsymbol{k}_{\mathrm{B},\parallel}) = 0$ for a given f and $\boldsymbol{k}_{\mathrm{B},\parallel}$ does not prove that no mode exists for these parameters but only that no mode coupling to modes in the glass substrate exists. Even with this in mind, a measurement of $p_\omega(\boldsymbol{k}_{\mathrm{B},\parallel})$ can, of course, not be used to definitely prove that a photonic crystal has the band structure underlying the calculation. It can, however, be used to exclude those band structures whose projected $p_\omega(\boldsymbol{k}_{\mathrm{B},\parallel})$ is known to be in disagreement with the measured $p_\omega(\boldsymbol{k}_{\mathrm{B},\parallel})$.

In our case, the emitters are the titanium-dioxide rods of the woodpile which are excited *via* a one-photon absorption process and the fluroescence is collected with a microscope objective with a numerical aperture (NA) equal to 1.4. This implies the following for the measured intensity distribution:

1. Only those modes for which $\boldsymbol{k}_{B,||} \leq \mathrm{NA} \cdot \frac{2\pi f}{c}$ is satisfied will be collected.

2. Since the emitters are localized in the dielectric, their coupling strength to a given mode will depend on the field strength of that mode in the dielectric.

3. Titania rods at and near the surface as well as titania rods in the bulk of the photonic crystal will be excited and contribute to the detected fluorescence.

Again, the first point is easily evaluated. A quantitative evaluation of the second point requires the knowledge of the field distributions of the modes. However, as a rule of thumb, we expect the coupling to be most efficient to the modes in the first and second band of the photonic crystal since these modes are more strongly localized in the dielectric than those in the third and fourth band. The impact of the third point can not be quantified from the band structure or the field distributions obtained in the framework describes in Chapter 2 because there, an infinite crystal is assumed. For a quantification it would be necessary to have knowledge about the states of the electromegnetic field at the interface of the photonic crystal. One way to eliminate the contribution of the emitters at the surface would be to excite the titania rods *via* two-photon absorption. We tested whether this is possible with the pulsed titanium-sapphire laser used as the writing laser in our STED-DLW setup. While it is possible to excite fluorescence with this excitation, a test titania woodpile bleached and took irreversible damage that was visible under the microscope.

With all this in mind, let us take a look at the outcome of the experiment I just outlined. Figure 6.6 shows $p_\omega(\boldsymbol{k}_{\mathrm{B},\parallel})$ measured for nine different frequencies *after the FIB cut* on the sample $\mathrm{FSL212}_3$ and the calculated map of $p_\omega(\boldsymbol{k}_{\mathrm{B},\parallel})$ using the same discretisation as for the density of states. The excited area is approximately 20 µm wide. All measured and all calculated colour plots use the same colour scale, except the calculated one for 696 nm. Here, the values have been multiplied by 3.5 for ease of viewing. The yellow circle in the right column indicates those wavevectors $\boldsymbol{k}_{\mathrm{B},\parallel}$

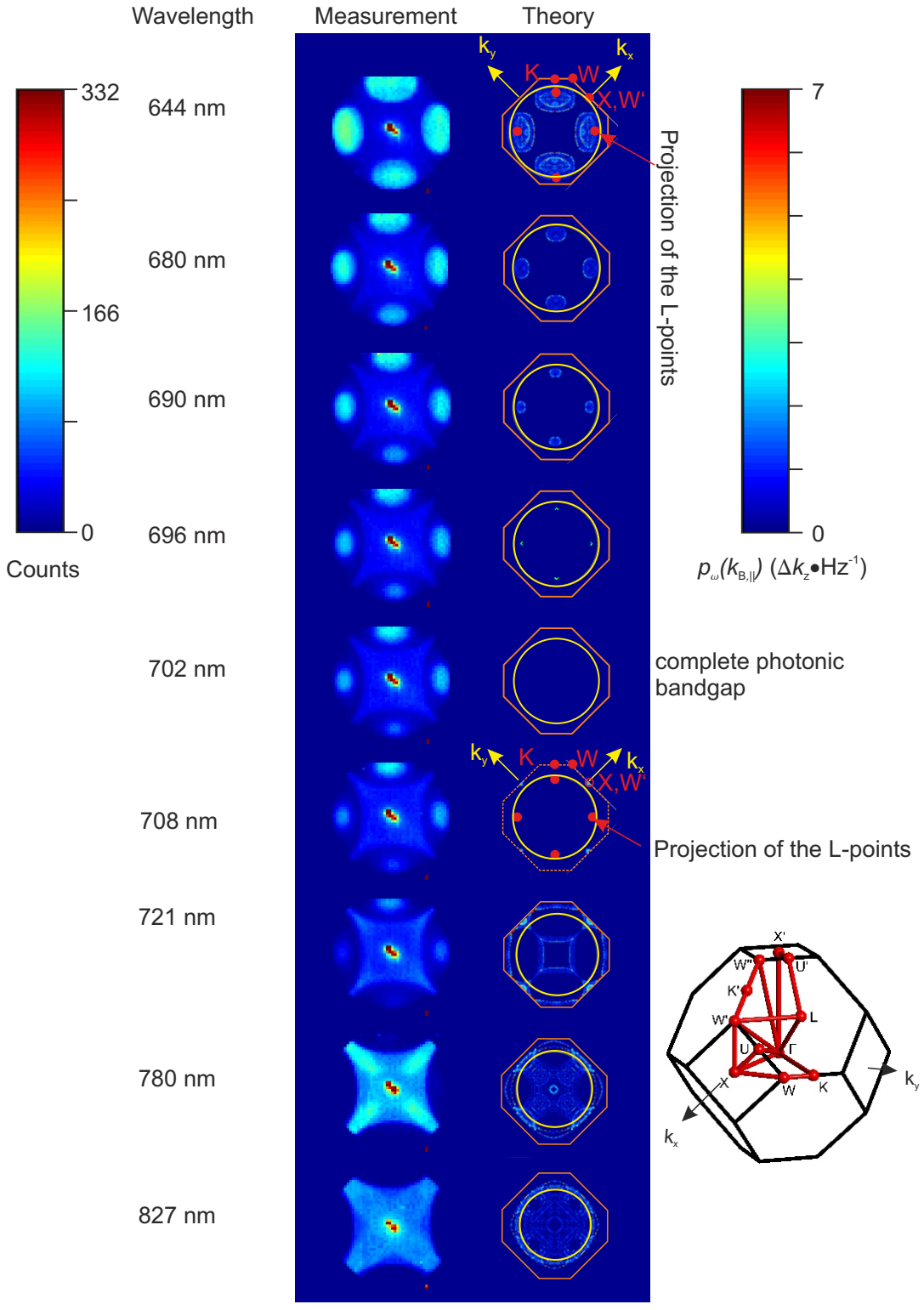

Figure 6.6: Angel resolved photon emission spectra of $FSL212_3$ and corresponding calculations. Description in the main text.

that are accesible with our setup. The k_x-k_y-plane is the plane in reciprocal space that contains the wavevectors parallel to the interface. Its intersection with the edge of the first Brillouin zone (see inset) is indicated in orange and some points of high symmetry or their projections onto the k_x-k_y-plane are indicated in red. The size of the discretisation in reciprocal space corresponds to a value of $\Delta k_z = 2\pi/(50 \cdot 0.949 \cdot a_{\mathrm{fcc}}) = 3.021 \cdot 10^5\,\mathrm{m}^{-1}$.

In the measurement column, the recorded images of the back focal plane at the indicated wavelength are shown. This means that the colour of one pixel in the images shown in 6.6 gives the counts that were collected at the wavelength indicated during the time in which the end of the fibre was held at that pixel of the image. The red spot in the center of the picture is most likely due to light from the excitation laser that was reflected either at the waveplate WP or at the glass-crystal interface and passed though the beamsplitter BS (see Figure 6.5). This light could still cause measurable fluorescence in the fibre used to scan the image plane. I will therefore disregard this spot for the rest of the discussion.

For the interpretation of the measurements I will assume that the circular aperture that is visible in the measured images corresponds to the full extent of the yellow circle of accessible states in the right column. As outlined above, it is the field distribution associated with a Bloch mode that determines how strongly it couples both to the emitter and to modes in the substrate. Therefore, I will refrain from a quantitative comparison at this point and focus on qualitative features of theory and measurement. The first thing we see is that the directions of emission predicted by theory are present in the measurements, but they are broadened with respect to the prediction based on the band structure. We also note that for frequencies inside the complete photonic bandgap, light is still detected in the image plane. As discussed above, this is not utterly surprising since the surface of the photonic crystal is excited as well as the bulk.

There is also a contribution to the signal that is not explained by the calculated p_ω: The predicted emission features are smeared out spatially in the image plane as well as spectrally – both of the fourfold rotationally symmetric features predicted by theory for the air band and the dielectric band are discernible at the side of the bandgap they are not predicted at. For the air band, the predicted feature is the 4 circle-like spots at the projection of the L-points for $\lambda \leq 697\,\mathrm{nm}$. For the dielectric band it is the feature that can be described as cross-like at $\lambda = 780\,\mathrm{nm}$ and that develops a hole in the middle as λ approaches 720 nm. The cross (the four circles) should be visible exclusively at wavelengths below (above) the bandgap for a perfect, bulk photonic crystal with the band structure discussed in Figure 6.4. This spectral smearing out of the features might be caused by the above-mentioned emitters at the surface of the crystal. Also, the crystal might be damaged by the FIB cut.

In any case, an indicator of quality is the fact that the fourfold symmetry is well maintained in the experiment both for wavelengths in the air- and in the dielectric band. In previous experiments that investigated emission from quantum dots from three-dimensional opaline photonic crystal samples [29] or the diffusive transport of light through opaline samples [31,117], no breaking of the rotational symmetry by the

sample was demonstrated. The reasons cited for this were the polycrystallinity of the samples under investigation and the presence of defects, especially near the surface. This encourages me to claim that the photonic crystal made by us is a photonic single-crystal, as one would also have expected from the fabrication method and the optical and SEM micrographs.

The angle-resolved measurement of fluorescence outlined here has some similarity to the method of angle resolved photoelectron spectroscopy. The latter is a standard method to investigate electronic band structures by measuring the angular distribution of electrons exiting the sample upon irradiation with ultraviolet light. [118] It allows the direct measure of the electronic band structure if one assumes that absorption of an ultraviolet photon creates a free electron inside the crystal. This assumption allows for the determination of the electron's wavevector component perpendicular to the interface. I currently do not see a valid analogon to this assumption in the study of photonic band structures by angle-resolved photon emission spectroscopy. If a method or valid assumption to determine this missing wavevector component were to be found, the amount of information about the photonic band structure that can be gathered would greatly increase. In this light, I would like to conclude this chapter by stating that the angle-resolved measurement of photoluminescence of emitters inside high-quality photonic crystals is an interesting method that allows the measurement of quantities that are closely linked to the band structure.

7 Conclusion and outlook

In the field of design there is a statement that "Form follows function", *i.e.*, that the shape of an object should be deduced from its function. In the design of optical elements such as glass lenses this is especially true since, given a particular glass, form is inherently linked to function. Thus, what is a guideline in normal design is a constraint in optical design. With the work shown in this thesis I tried to alleviate this constraint by providing tailored optical materials.

The general approach taken for this was to exploit the effect of defining a structure and a material at the scale of one wavelength or smaller. Since I was treating optical materials, this implied three-dimensional structures with sizes on the order of a micrometer, even considerably smaller in some cases.

As I outlined in Chapter 3, direct laser writing (DLW) and its resolution-enhanced version stimulated emission depletion DLW (STED-DLW) are methods of choice for structuring a polymer in three dimensions. DLW allows for the formation of almost arbitrary shapes by exploiting a polymerisation reaction driven by two-photon absorption of the photoinitiator. As I also outlined, the resolution achievable with DLW is not sufficient for the creation of the samples discussed in Chapter 6. Luckily, STED-DLW was able to provide a sufficient resolution by combining the two-photon absorption process with photodeactivation of excited photoinitiator molecules. Thus, it was possible to define the desired geometries.

The approach taken to define a material was atomic layer deposition (ALD). This method deposits films conformally, *i.e.*, it will cover surfaces of any shape with a film of homogeneous thickness. This quality makes it the method of choice for working with three-dimensional templates. As I discussed in Chapter 3, the conformality of a film grown by an ideal ALD process is the result of growing the film chemically from a reaction between the vapors of two precursors. A conformal film growth mode can be ensured if the chemical reaction can be split up into two half reactions. Both of these reactions have to be able to take place at the surface of the growing film where they also have to be selfterminating. A surface that is exposed to the first precursor will then become reactive to the second, and *vice versa*. Sequential exposure of the sample surface to the precursors, while maintaining a strict separation of the precursors in the gas phase, then results in the desired conformal film growth that is substrate limited and independent of all other parameters. With such a deposition scheme, it is possible to allow a theoretically unlimited amount of time for the precursors to reach every part of an arbitrarily shaped polymer structure. Most precursors that are available behave less than ideally though and since this behaviour originates from the properties of the precursor molecule, it cannot be easily controlled or compensated with the means

provided by an ALD reactor. I therefore also discussed some effects and mechanism of precursor non-idealities and how they can be reduced to a minimum under the constraints imposed by the applications we had in mind and the apparatus we used. For the case of titanium dioxide ALD, I undertook a detailed survey of precursors and ALD process parameters, based both on literature and my own experiments. With the application of photonic crystals in mind, I also optimized the process parameters. The goal here was reproducibility and to obtain high refractive index titanium dioxide films. The optimum refractive index was achieved for the precursor combination of titanium isopropoxide and hydrogen peroxide grown at 250 °C. These films are at least in parts composed of the anatase phase of titanium dioxide and have a refractive index of 2.48 at a wavelength of 700 nm, corresponding to a permittivity of $\epsilon = 6.15$.

In Chapter 4, I then turned to the first application dealing with tailored materials. Here, I demonstrated that a combination of the ALD processes for zinc oxide (ZnO) and aluminum oxide can be used to deposit aluminum doped zinc oxide (AZO). Here, the layer-by-layer film growth in ALD offers a conceptually easy way for doping: The dopants are introduced as precursors during film growth and control over the dopant concentration is achieved by controlling the ratio of aluminum- to zinc precursor pulses. As I had previously outlined in Chapter 2, I expected the permittivity of the thus-grown films to be governed by the Drude model. The decisive parameter here is the plasma frequency which depends on the free carrier density that should, in turn, be proportional to the dopant concentration. A systematic investigation of AZO films doped to varying degrees showed that the aluminum concentration in the films is indeed proportional to the ratio of precursor pulses. Also, the plasma frequency depends on this ratio as expected up to a ratio of 1 aluminum precursor pulse per 12 zinc precursor pulses. The range of plasma frequencies that is covered this way spans more than one octave, corresponding to frequencies between 400 THz and 150 THz. With a view to applications of AZO in three-dimensional metamaterials, I demonstrated that AZO-ALD yields smooth, conformal films and developed and demonstrated techniques for depositing, patterning and etching this material.

The following Chapter 5 was devoted to a fabrication method for another tailored, three-dimensionally structured material – the woodpile photonic crystal. As I had described in Chapter 2, these materials consist of two dielectrics that are arranged periodically on a lattice. The goal here was to produce a photonic crystal with a band structure tailored such that it has a complete photonic bandgap for visible light. Therefore, the rod distance had to be on the order of 300 nm and one of the two dielectrics needed to have a permittivity of the order of $\epsilon = 5.5$, while the other material had to be air. Because of the small rod distance, the lattice had to be defined by STED-DLW and the polymer needed to be replaced with titanium dioxide (TiO_2). The need to write large, high quality polymer templates brought up some challenges that are not usually encountered in STED-DLW if the sample size is small or if the need for precision is relaxed.

One disturbing influence to be eliminated was the influence of temperature on the

distance between the focusing optics and the sample. During the process optimization we found out that within 20 minutes, this distance can change by up to 40 nm. This translates directly into an equally large error in the fabricated polymer template. We were able to track this drift and were thus able to compensate it. With this measure in place, the writing time for one polymer template was 7 hours. On this time scale, mechanical drifts of the optical components of the setup become important as well. These lead to a misalignment of the two foci used for STED-DLW with respect to each other and, thus, a variation of the effective exposure dose. It was possible to correct for this effect as well after the writing procedure had been adapted to include automated measurements of the foci.

The conversion of the polymer template to TiO_2 using a double-inversion process was a materials processing challenge that, in the end, was overcome by us. Having the adaption of a double-inversion (DI) procedure previously developed for silicon in mind, it was, evidently, necessary to find an ALD precursor for TiO_2. However, changing only the final material of the DI was not possible. The reason for this is the necessity to be able to etch it selectively against the intermediate material. This is not the case if one uses the intermediate material known from silicon DI. Thus, with new final and intermediate materials, a whole new set of material processing steps needed to be found. For a successful DI to be possible I had to implement a ZnO ALD step, use a novel sputtering procedure to dry-etch the ZnO, adapt the calcination procedure for removal of the polymer to the constraints imposed by ZnO, find a TiO_2 precursor suited for long residence times at high enough temperatures to yield high refractive index material, and find a wet-etch method which etches ZnO but leaves TiO_2 untouched.

The TiO_2-based photonic crystals produced this way have comparably small bandgaps. Hence, the impact of unfilled inclusions that are produced by a double-inversion procedure based on conformal coatings needed to be considered more carefully than in the case of silicon DI, as well. I found that they have a non-negligible impact on whether a complete photonic bandgap can be formed and that for most geometries that can be defined using STED-DLW alone, no bandgap exists after double-inversion into TiO_2. Therefore, a new step was introduced into the DI procedure: By infiltrating the ZnO inverse of the polymer template conformally with ZnO by ALD before the TiO_2 ALD step, the rod dimensions of the final TiO_2 woodpile were changed. This results in a complete photonic bandgap if the amount of ZnO is chosen correctly. The optimum amount is dependent on the dimensions of the template. Hence, a non-destructive system needed to be devised that allows for a reliable estimate of the polymer template dimensions. After the ZnO-reinfiltraion step by ALD all surfaces of the sample are covered with ZnO. Thus, the TiO_2 grown by ALD will grow on ZnO exclusively. Then it will not be attached to the substrate anymore after removal of the ZnO. Therefore, a mechanical clamp on every woodpile was defined by STED-DLW right before the ZnO was removed.

Once this process was developed, titania woodpiles were produced and their angle- and polarisation resolved transmission spectra were measured as described in Chapter

6. One sample whose transmission spectra were compatible with a complete photonic bandgap was cut open with a focused ion beam (FIB). We took the dimensions taken from the FIB cut and the measured material properties of TiO_2 as inputs for calculations corresponding to the spectra we had measured. Theory and experiment matched well, reassuring us that the computed photonic band structure for the exact same parameters would present a meaningful description of the sample. The band structure had a complete photonic bandgap between 696 and 707 nm. By this detailed and thorough characterisation and modeling we have confidence in the claim to have produced a photonic crystal that has a complete photonic bandgap for visible light.

With this sample, we were also able to perform an experiment that is a close analogy to angle resolved photoemission spectroscopy, a method used to measure the electronic bandstructure of solids. Here, we exploited the fluorescence emission of the TiO_2 composing the woodpile to study the coupling of emitters to the electromagnetic modes inside the crystal. The observed quantity was the angular distribution of emitted light. As outlined in section 6.4, this is closely linked to the photonic band structure. In combination with a thorough theoretical modeling it could potentially yield more information than the angle- and polarisation resolved transmission spectroscopy.

As I have already mentioned, photonic crystals with complete photonic bandgaps can – and have been – realized at microwave and infrared frequencies. Thus, the valid question arises of why one would need to go through all these efforts to make one at visible frequencies. I have two answers to this question. One cannot be quantified or proven, whereas the other one is a technical one: The technical tool box for the visible part of the electromagnetic spectrum is much evolved, making some experiments easier than in other frequency regions. Also, any application of photonic crystals that is related to human perception will necessarily have to work in the visible. However, the envisioned applications of photonic crystals for lighting or perception to date do not specifically ask for a complete photonic bandgap. Therefore, I would like to point out that the visible range has a certain psychological appeal as well.

This leads to my second answer for which I would first like to quote from the November 2012 issue of Nature Materials, a focus issue dedicated to the 25th anniversary of the conception of photonic crystals. The closing sentences of the editorial are "... the realization of truly 3D photonic crystals, particularly at optical wavelengths, has proved persistently challenging owing to the intricacy of periodically nanosculpturing a material in all three spatial dimensions, and at the moment this limits the technological impact of these structures. With continuous advances in the synthesis, fabrication and self-assembly of photonic nanomaterials we can be hopeful that those challenges will eventually be overcome, closing another chapter in what has until now been a success story."

Also, in the March 2007 issue of Nature Materials, a news and views article reports on a novel fabrication method that might be used to one day create photonic crystals with visible complete photonic bandgaps [44]. In this article, the author states in reference to the birth of the field of photonic crystals, that"... the original goal, a

three-dimensional material with a complete photonic bandgap for visible light, has eluded us." This article was entitled "A view of the future".

I take that as a pleasant praise for our achievement and as an indication that there is a considerable interest in visible complete photonic bandgap materials in their own right. However, I neither think that it is necessary to close a chapter at this point nor to stop thinking about the future. The photonic crystals developed and the method to produce them will hopefully be only a starting point for future experiments using samples like ours, which are an interesting optical analogue of electronic solid-state physics. For example, the angle resolved fluorescence can be measured using samples that are significantly smaller than those needed for transmission spectroscopy. Smaller samples can be produced with even less imperfections than the ones shown in this thesis, especially since the conformality requirements during the ALD step are relaxed. In addition it would be great to investigate effects of the photonic bandstructure on the decay rate of emitters whose emission frequency lies inside the gap. For this, it will be necessary to transfer the photonic crystals from the glass substrate to a different substrate, which is work-intensive but feasible.

Taking a step back to consider the question of tailored optical materials, the examples of both the doped ZnO and the photonic crystal made by double-inversion have shown that ALD is a suitable tool to impart optical functionality onto a three-dimensional geometry. The outer edges of the range of imaginable permittivities remain uncovered by ALD so far, however: No metal with a plasma frequency in the UV range has been grown in optical quality by ALD so far and neither has any material with a permittivity comparable to that of silicon been grown by ALD.

Still, with the techniques presented in this thesis, the statement "Form follows function" which, in the context of optical design, had to be read more like "Form and function cannot be seperated", can now be interpreted in a more relaxed manner with the techniques developed in this thesis.

Appendix

1 Silanisation

These 3TMPS-molecules used for the silanisation of glass subtrates serve to enhance the adhesion of the written polymer structure. They are composed of a propanyl-backbone that is a attached to a trimethoxy-silane-group at one end and to a methacrylic-acid group at the other end. Three methanol-groups linked to a silicon atom form the trimethoxy-silane-group. In the presence of water or hydroxyl groups on a surface, the reactions depicted in Figure 1 take place: This way a surface covered with

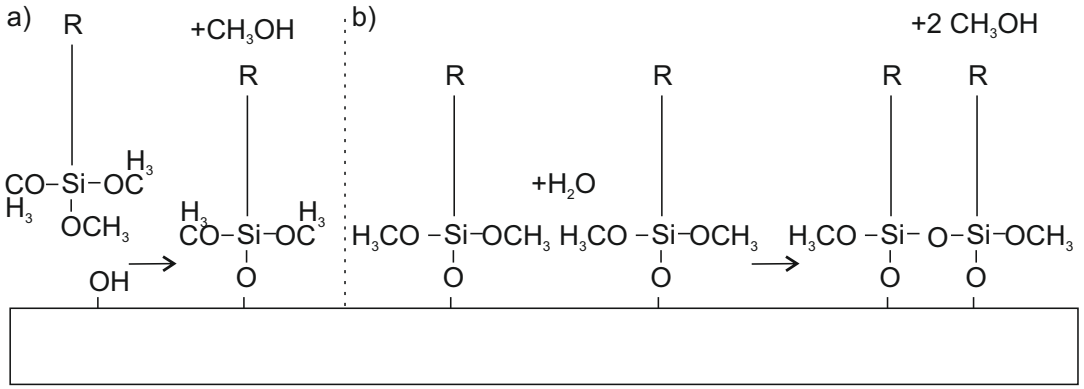

Figure 1: Reactions taking place during silanisation of a glass slide with a trimethoxy-silane. a) Trimethoxy-silane molecules chemisorb to the substrate. b) In the presence of water two chemisorbed trimethoxy-silane molecules can link. R denotes the remaining parts of the molecule. In this case it is a propanyl-group whose free end exhibits a methacrylic-acid functionality.

a high density of hydroxyl groups and traces of adsorbed water can be covered by an interconnected monolayer of 3MPTS. The exposed end of this molecule exhibits the methacrylic-acid functionality. This functionality is also contained in the monomer of the STED-DLW photoresist and used in the laser-driven reaction driving the polymerization. So essentially, one has now chemically bonded a monolayer of photo-resist monomer to the glass substrate, resulting in an excellent adhesion of the exposed photoresist to the glass substrate.
A lot of recipes for silanization of glass can be found in the literature. The silanization needs to yield clean, residue-free glass-substrates that are compatible with STED-DLW, however, and this is not the case for all procedures found in literature. I therefore state the procedure I used:

1. Subject the glass slides to an air plasma for 10 min
2. Immediately after that, quickly dip them in deionized water, then blow-dry thoroughly with nitrogen.
3. Immerse the glass slides in a 1 mmol solution of 3MPTS in water-free toluol. Cover the container with parafilm and leave them for 60 min. It is preferable that the glass slides are kept standing upwards to minimize sedimentation of particulates in the solution.
4. Remove the glass-slides and immediately thoroughly rinse them in water-free toluol, then blow-dry with nitrogen.

Other people have obtained results sufficient for conventional DLW [119, 120], but this procedure has always worked in my case, while others were not reliable. My hypothesis is that residues appearing on the glass-slides after silianization with other methods are due to trace water that is introduced into the silanizing toluol-solution. The water-molecules should be able to react with the silane-groups of 3MPTS and lead to cross-linking. Depending on whether the trace water is solved as an impurity in the toluol or contained in the form of micro-droplets, this should lead either to continuously growing chanis of 3MPTS or to micelle-like 3MPTS-shells around water micro-droplets. Both of these could sediment and/or attach to the substrate surface leading to smears.

2 Sample FSL212$_4$

As mentioned in chapter 6, a similar woodpile to the one discussed there was produced. Unfortunately, it was contaminated with a particle during the direct-laser-writing. Its spectra are shown here in Figure 2. Both samples have been written with identical writing parameters and were double-inverted in the same process. The templates have similar, but not identical FTIR-spectra (the spectrum of FSL212$_4$ was taken away from the particle). Both samples are not more than 200 µm apart from each other on the same glass substrate so that variations in the process conditions should be minimal. The angle- and polarisation resolved transmissions spectra were taken avoiding the particle as well as possible. They are qualitatively similar to those of FSL212$_3$, but the wavelength-interval of 1% transmission suppression ranges only from 682 nm to 691 nm. Still, the minimum observable transmission of $2{\cdot}10^{-4}$ is reached for every angle of incidence and every polarisation.

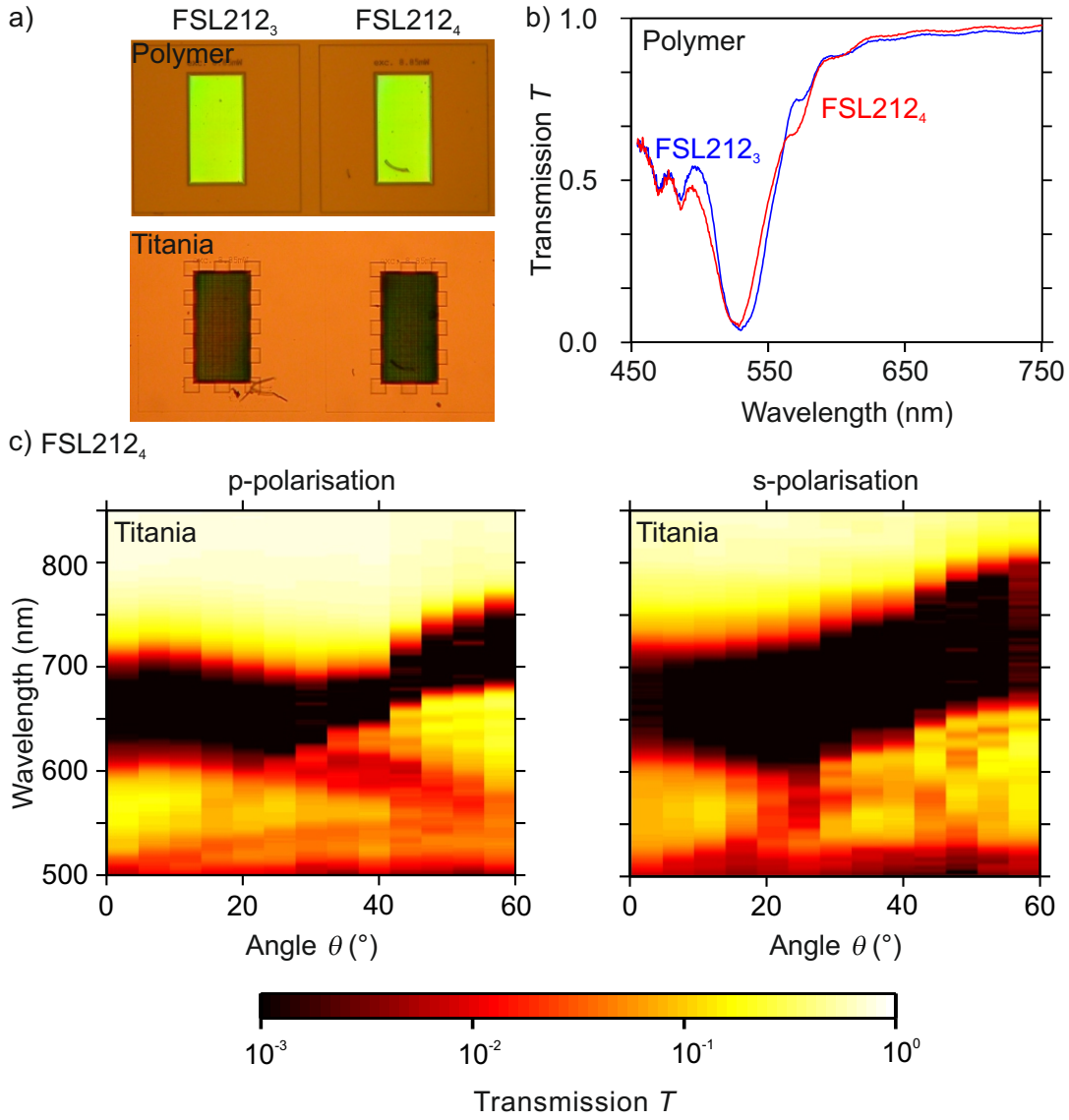

Figure 2: Sample FSL212$_4$. a) The optical appearance of both the polymer template and the double-inverted sample FSL212$_4$ (right column) is very similar to FSL212$_3$, the sample discussed in chapter 6 (left column). b) The same holds true for the FTIR transmission spectra of FSL212$_3$ and FSL212$_4$. c) The angle- and polarisation resolved transmission spectrum of FSL212$_4$. A strong suppression of transmission centered around 690 nm is present.

Bibliography

[1] Jiu Zhang, Zhong-lin Wang, Jun Liu, Shaowei Chen, and Gang-yu Liu. *Self-Assembled Nanostructures*. Nanostructure Science and Technology. Springer, 2002.

[2] Vicki L. Colvin. From opals to optics: Colloidal photonic crystals. *MRS Bulletin*, 26(08):637–641, 2001.

[3] Ganapathi Subramania, Yun-Ju Lee, and Arthur J Fischer. Silicon-based near-visible logpile photonic crystal. *Advanced materials*, 22(37):4180–4185, October 2010. PMID: 20803766.

[4] Ganapathi Subramania, Yun-Ju Lee, Arthur J Fischer, and Daniel D Koleske. Log-Pile TiO_2 photonic crystal for light control at Near-UV and visible wavelengths. *Advanced Materials*, 22(4):487–491, January 2010.

[5] Na Liu, Hongcang Guo, Liwei Fu, Stefan Kaiser, Heinz Schweizer, and Harald Giessen. Three-dimensional photonic metamaterials at optical frequencies. *Nature Materials*, 7(1):31–37, January 2008.

[6] D. C. Meisel, M. Wegener, and K. Busch. Three-dimensional photonic crystals by holographic lithography using the umbrella configuration: Symmetries and complete photonic band gaps. *Physical Review B*, 70(16):165104, October 2004.

[7] M. Campbell, D. N. Sharp, M. T. Harrison, R. G. Denning, and A. J. Turberfield. Fabrication of photonic crystals for the visible spectrum by holographic lithography. *Nature*, 404(6773):53–56, March 2000.

[8] Shoji Maruo, Osamu Nakamura, and Satoshi Kawata. Three-dimensional microfabrication with two-photon-absorbed photopolymerization. *Optics Letters*, 22(2):132–134, January 1997.

[9] Markus Deubel. *Three-Dimensional Photonic Crystals via Direct Laser Writing: Fabrication and Characterization*. PhD thesis, Universität Karlsruhe (TH), Karlsruhe, 2006.

[10] Joachim Fischer. *Three-dimensional optical lithography beyond the diffraction limit*. PhD thesis, Karlsruhe Institute of Technology, Karlsruhe, 2012.

[11] Tuomo Suntola and Jorma Antson. United states patent: 4058430 - method for producing compound thin films, November 1977.

[12] J. B. Pendry, D. Schurig, and D. R. Smith. Controlling electromagnetic fields. *Science*, 312(5781):1780–1782, June 2006.

[13] Sajeev John. Strong localization of photons in certain disordered dielectric superlattices. *Physical Review Letters*, 58(23):2486–2489, June 1987.

[14] Eli Yablonovitch. Inhibited spontaneous emission in solid-state physics and electronics. *Physical Review Letters*, 58(20):2059–2062, May 1987.

[15] N. Tétreault, G. von Freymann, M. Deubel, M. Hermatschweiler, F. Pérez-Willard, S. John, M. Wegener, and G. A. Ozin. New route to three-dimensional photonic bandgap materials: Silicon double inversion of polymer templates. *Advanced Materials*, 18(4):457–460, 2006.

[16] John D. Joannopoulos, Steven G. Johnson, Joshua N. Winn, and R. D. Meade. *Photonic Crystals: Molding the Flow of Light*. Princeton University Press, Princeton, 2nd edition edition, 2008.

[17] Steven Johnson and John Joannopoulos. Block-iterative frequency-domain methods for maxwell's equations in a planewave basis. *Optics Express*, 8(3):173–190, January 2001.

[18] Christian Wolff. *Band Structure Based Analysis of Certain Photonic Crystal Structures*. PhD thesis, Karlsruhe Institut of Technology, Karlsruhe, 2011.

[19] J. M. Harrison, P. Kuchment, A. Sobolev, and B. Winn. On occurrence of spectral edges for periodic operators inside the brillouin zone. *Journal of Physics A: Mathematical and Theoretical*, 40(27):7597, July 2007.

[20] K.M. Ho, C.T. Chan, C.M. Soukoulis, R. Biswas, and M. Sigalas. Photonic band gaps in three dimensions: New layer-by-layer periodic structures. *Solid State Communications*, 89(5):413–416, February 1994.

[21] Sajeev John and Tran Quang. Spontaneous emission near the edge of a photonic band gap. *Physical Review A*, 50(2):1764–1769, August 1994.

[22] Sajeev John and Jian Wang. Quantum electrodynamics near a photonic band gap: Photon bound states and dressed atoms. *Physical Review Letters*, 64(20):2418–2421, May 1990.

[23] Ulrich Hoeppe, Christian Wolff, Jens Küchenmeister, Jens Niegemann, Malte Drescher, Hartmut Benner, and Kurt Busch. Direct observation of non-markovian radiation dynamics in 3D bulk photonic crystals. *Physical Review Letters*, 108(4):043603, January 2012.

[24] Matthew R. Jorgensen, Jeremy W. Galusha, and Michael H. Bartl. Strongly modified spontaneous emission rates in diamond-structured photonic crystals. *Physical Review Letters*, 107(14):143902, 2011.

[25] M. D. Leistikow, A. P. Mosk, E. Yeganegi, S. R. Huisman, A. Lagendijk, and W. L. Vos. Inhibited spontaneous emission of quantum dots observed in a 3D photonic band gap. *Physical Review Letters*, 107(19):193903, November 2011.

[26] Ivan S. Nikolaev, Peter Lodahl, A. Floris van Driel, A. Femius Koenderink, and Willem L. Vos. Strongly nonexponential time-resolved fluorescence of quantum-dot ensembles in three-dimensional photonic crystals. *Physical Review B*, 75(11):115302, March 2007.

[27] Peter Lodahl, A. Floris van Driel, Ivan S. Nikolaev, Arie Irman, Karin Overgaag, Daniël Vanmaekelbergh, and Willem L. Vos. Controlling the dynamics of spontaneous emission from quantum dots by photonic crystals. *Nature*, 430(7000):654–657, August 2004.

[28] Masayuki Fujita, Shigeki Takahashi, Yoshinori Tanaka, Takashi Asano, and Susumu Noda. Simultaneous inhibition and redistribution of spontaneous light emission in photonic crystals. *Science*, 308(5726):1296 –1298, May 2005.

[29] Bart H. Husken, A. Femius Koenderink, and Willem L. Vos. Angular redistribution of near-infrared emission from quantum dots in 3D photonic crystals. *The Journal of Physical Chemistry C*, December 2012.

[30] Henry P. Schriemer, Henry M. van Driel, A. Femius Koenderink, and Willem L. Vos. Modified spontaneous emission spectra of laser dye in inverse opal photonic crystals. *Physical Review A*, 63(1):011801, December 2000.

[31] A. Femius Koenderink and Willem L. Vos. Light exiting from real photonic band gap crystals is diffuse and strongly directional. *Physical Review Letters*, 91(21):213902, November 2003.

[32] E. Yablonovitch, T. J. Gmitter, and K. M. Leung. Photonic band structure: The face-centered-cubic case employing nonspherical atoms. *Physical Review Letters*, 67(17):2295–2298, October 1991.

[33] S. Y. Lin, J. G. Fleming, D. L. Hetherington, B. K. Smith, R. Biswas, K. M. Ho, M. M. Sigalas, W. Zubrzycki, S. R. Kurtz, and Jim Bur. A three-dimensional photonic crystal operating at infrared wavelengths. *Nature*, 394(6690):251–253, July 1998.

[34] M. J. A. de Dood, B. Gralak, A. Polman, and J. G. Fleming. Superstructure and finite-size effects in a Si photonic woodpile crystal. *Physical Review B*, 67(3):035322, January 2003.

[35] A. Blanco and C. López. Silicon onion-layer nanostructures arranged in three dimensions. *Advanced Materials*, 18(12):1593–1597, 2006.

[36] Sung-Gyu Park, Masao Miyake, Seung-Man Yang, and Paul V Braun. Cu_2o inverse woodpile photonic crystals by prism holographic lithography and electrodeposition. *Advanced Materials*, 23(24):2749–2752, June 2011.

[37] G. M. Gratson, F. García-Santamaría, V. Lousse, M. Xu, S. Fan, J. A. Lewis, and P. V. Braun. Direct-write assembly of three-dimensional photonic crystals: Conversion of polymer scaffolds to silicon hollow-woodpile structures. *Advanced Materials*, 18(4):461–465, 2006.

[38] J. G. Fleming and Shawn-Yu Lin. Three-dimensional photonic crystal with a stop band from 1.35 to 1.95 µm. *Optics Letters*, 24(1):49–51, January 1999.

[39] S. Noda, N. Yamamoto, H. Kobayashi, M. Okano, and K. Tomoda. Optical properties of three-dimensional photonic crystals based on III-V semiconductors at infrared to near-infrared wavelengths. *Applied Physics Letters*, 75(7):905–907, August 1999.

[40] Susumu Noda, Katsuhiro Tomoda, Noritsugu Yamamoto, and Alongkarn Chutinan. Full three-dimensional photonic bandgap crystals at near-infrared wavelengths. *Science*, 289(5479):604 –606, July 2000.

[41] Shigeki Takahashi, Katsuyoshi Suzuki, Makoto Okano, Masahiro Imada, Takeshi Nakamori, Yuji Ota, Kenji Ishizaki, and Susumu Noda. Direct creation of three-dimensional photonic crystals by a top-down approach. *Nature Materials*, 8(9):721–725, 2009.

[42] J. M van den Broek, L. A Woldering, R. W Tjerkstra, F. B Segerink, I. D Setija, and W. L Vos. Inverse-Woodpile photonic band gap crystals with a cubic diamond-like structure made from Single-Crystalline silicon. *Advanced Functional Materials*, 2011.

[43] M. Hermatschweiler, A. Ledermann, G. A. Ozin, M. Wegener, and G. von Freymann. Fabrication of silicon inverse woodpile photonic crystals. *Advanced Functional Materials*, 17(14):2273–2277, 2007.

[44] David J. Norris. Photonic crystals: A view of the future. *Nat Mater*, 6(3):177–178, March 2007.

[45] I. Staude, M. Thiel, S. Essig, C. Wolff, K. Busch, G. von Freymann, and M. Wegener. Fabrication and characterization of silicon woodpile photonic crystals with a complete bandgap at telecom wavelengths. *Optics Letters*, 35(7):1094–1096, April 2010.

[46] J.J. Sakurai. *Modern Quantum Mechanics*. Addison-Wesley, New York, 1993.

[47] D. R. Smith, J. B. Pendry, and M. C. K. Wiltshire. Metamaterials and negative refractive index. *Science*, 305(5685):788–792, August 2004.

[48] Stefan Linden, Christian Enkrich, Martin Wegener, Jiangfeng Zhou, Thomas Koschny, and Costas M. Soukoulis. Magnetic response of metamaterials at 100 terahertz. *Science*, 306(5700):1351–1353, November 2004.

[49] Justyna K. Gansel, Michael Thiel, Michael S. Rill, Manuel Decker, Klaus Bade, Volker Saile, Georg von Freymann, Stefan Linden, and Martin Wegener. Gold helix photonic metamaterial as broadband circular polarizer. *Science*, 325(5947):1513 –1515, 2009.

[50] Gunnar Dolling, Christian Enkrich, Martin Wegener, Costas M. Soukoulis, and Stefan Linden. Simultaneous negative phase and group velocity of light in a metamaterial. *Science*, 312(5775):892–894, May 2006.

[51] Jason Valentine, Shuang Zhang, Thomas Zentgraf, Erick Ulin-Avila, Dentcho A. Genov, Guy Bartal, and Xiang Zhang. Three-dimensional optical metamaterial with a negative refractive index. *Nature*, 455(7211):376–379, September 2008.

[52] Joachim Fischer, Tolga Ergin, and Martin Wegener. Three-dimensional polarization-independent visible-frequency carpet invisibility cloak. *Optics Letters*, 36(11):2059–2061, June 2011.

[53] Zubin Jacob, Leonid V. Alekseyev, and Evgenii Narimanov. Optical hyperlens: Far-field imaging beyond the diffraction limit. *Optics Express*, 14(18):8247–8256, September 2006.

[54] Zhaowei Liu, Hyesog Lee, Yi Xiong, Cheng Sun, and Xiang Zhang. Far-field optical hyperlens magnifying sub-diffraction-limited objects. *Science*, 315(5819):1686–1686, March 2007.

[55] Alexandra Boltasseva and Harry A. Atwater. Low-loss plasmonic metamaterials. *Science*, 331(6015):290 –291, January 2011.

[56] P. R West, S. Ishii, G. V Naik, N. K Emani, V. M Shalaev, and A. Boltasseva. Searching for better plasmonic materials. *Laser & Photonics Reviews*, 4(6):795–808, November 2010.

[57] Gururaj V. Naik and Alexandra Boltasseva. A comparative study of semiconductor-based plasmonic metamaterials. *Metamaterials*, 5(1):1–7, April 2011.

[58] Huanyang Chen, C. T. Chan, and Ping Sheng. Transformation optics and metamaterials. *Nature Materials*, 9(5):387–396, May 2010.

[59] Ulf Leonhardt and Thomas G. Philbin. Chapter 2 - transformation optics and the geometry of light. In E Wolf, editor, *Progress in Optics*, volume Volume 53, pages 69–152. Elsevier, 2009.

[60] Andrea Alù, Mário G. Silveirinha, Alessandro Salandrino, and Nader Engheta. Epsilon-near-zero metamaterials and electromagnetic sources: Tailoring the radiation phase pattern. *Physical Review B*, 75(15):155410, April 2007.

[61] Evgenii E. Narimanov and Alexander V. Kildishev. Optical black hole: Broadband omnidirectional light absorber. *Applied Physics Letters*, 95(4):041106–041106–3, July 2009.

[62] Zubin Jacob, Igor I. Smolyaninov, and Evgenii E. Narimanov. Broadband purcell effect: Radiative decay engineering with metamaterials. *Applied Physics Letters*, 100(18):181105, 2012.

[63] Gururaj V. Naik, Jingjing Liu, Alexander V. Kildishev, Vladimir M. Shalaev, and Alexandra Boltasseva. Demonstration of Al:ZnO as a plasmonic component for near-infrared metamaterials. *Proceedings of the National Academy of Sciences*, 109(23):8834–8838, June 2012.

[64] Alexander V. Kildishev, Alexandra Boltasseva, and Vladimir M. Shalaev. Planar photonics with metasurfaces. *Science*, 339(6125), March 2013.

[65] C. L. Cortes, W. Newman, S. Molesky, and Z. Jacob. Quantum nanophotonics using hyperbolic metamaterials. *Journal of Optics*, 14(6):063001, June 2012.

[66] Omar Kidwai, Sergei V. Zhukovsky, and J. E. Sipe. Dipole radiation near hyperbolic metamaterials: applicability of effective-medium approximation. *Optics Letters*, 36(13):2530–2532, July 2011.

[67] Ying Huang, Yijun Feng, and Tian Jiang. Electromagnetic cloaking by layered structure ofhomogeneous isotropic materials. *Optics Express*, 15(18):11133–11141, September 2007.

[68] Franziska Klein, Thomas Striebel, Joachim Fischer, Zhongxiang Jiang, Clemens M. Franz, Georg von Freymann, Martin Wegener, and Martin Bastmeyer. Elastic fully three-dimensional microstructure scaffolds for cell force measurements. *Advanced Materials*, 22(8):868–871, 2010.

[69] E Abbe. Beiträge zur theorie des mikroskops und der mikroskopischen wahrnehmung. *Archiv für mikroskopische Anatomie*, 9:413–468, 1873.

[70] Stefan W. Hell. Microscopy and its focal switch. *Nature Methods*, 6(1):24–32, 2009.

[71] J. Fischer and M. Wegener. Three-dimensional optical laser lithography beyond the diffraction limit. *Laser & Photonics Reviews*, pages 22–44, 2012.

[72] Joachim Fischer and Martin Wegener. Three-dimensional direct laser writing inspired by stimulated-emission-depletion microscopy. *Optical Materials Express*, 1(4):614–624, August 2011.

[73] Riikka L. Puurunen. Surface chemistry of atomic layer deposition: A case study for the trimethylaluminum/water process. *Journal of Applied Physics*, 97(12):121301–121301–52, June 2005.

[74] K. L. Siefering and G. L. Griffin. Growth kinetics of CVD TiO_2: Influence of carrier gas. *Journal of The Electrochemical Society*, 137(4):1206–1208, April 1990.

[75] K. L. Siefering and G. L. Griffin. Kinetics of Low-Pressure chemical vapor deposition of TiO_2 from titanium tetraisopropoxide. *Journal of The Electrochemical Society*, 137(3):814–818, March 1990.

[76] Jaan Aarik, Aleks Aidla, Teet Uustare, Mikko Ritala, and Markku Leskelä. Titanium isopropoxide as a precursor for atomic layer deposition: characterization of titanium dioxide growth process. *Applied Surface Science*, 161(3–4):385–395, July 2000.

[77] Qi Xie, Yu-Long Jiang, Christophe Detavernier, Davy Deduytsche, Roland L. Van Meirhaeghe, Guo-Ping Ru, Bing-Zong Li, and Xin-Ping Qu. Atomic layer deposition of TiO_2 from tetrakis-dimethyl-amido titanium or Ti isopropoxide precursors and H_2O. *Journal of Applied Physics*, 102(8):083521–083521–6, October 2007.

[78] Swagelok. Valve sizing, technical bulletin, 2007.

[79] Ana (Editor) Londergan. *Atomic Layer Deposition Applications 4*, volume 16 of *ECS Transactions*. The Electrochemical Society, 2008.

[80] David M King, Samantha I Johnson, Jianhua Li, Xiaohua Du, Xinhua Liang, and Alan W Weimer. Atomic layer deposition of quantum-confined ZnO nanostructures. *Nanotechnology*, 20(19):195401, May 2009. PMID: 19420639.

[81] C. E. Kriegler, M. S. Rill, M. Thiel, E. Müller, S. Essig, A. Frölich, G. Freymann, S. Linden, D. Gerthsen, H. Hahn, K. Busch, and M. Wegener. Transition between corrugated metal films and split-ring-resonator arrays. *Applied Physics B*, 96(4):749–755, May 2009.

[82] K.-E. Elers, T. Blomberg, M. Peussa, B. Aitchison, S. Haukka, and S. Marcus. Film uniformity in atomic layer deposition. *Chemical Vapor Deposition*, 12(1):13–24, 2006.

[83] Jaan Aarik, Aleks Aidla, Teet Uustare, and Väino Sammelselg. Morphology and structure of TiO_2 thin films grown by atomic layer deposition. *Journal of Crystal Growth*, 148(3):268–275, March 1995.

[84] D R G Mitchell, G Triani, D J Attard, K S Finnie, P J Evans, C J Barbé, and J R Bartlett. Atomic layer deposition of TiO_2 and Al_2O_3 thin films and nanolaminates. *Smart Materials and Structures*, 15(1):S57–S64, February 2006.

[85] M. A. Cameron, I. P. Gartland, J. A. Smith, S. F. Diaz, and S. M. George. Atomic layer deposition of SiO_2 and TiO_2 in alumina tubular membranes: Pore reduction and effect of surface species on gas transport. *Langmuir*, 16(19):7435–7444, September 2000.

[86] J. Musschoot, Q. Xie, D. Deduytsche, S. Van den Berghe, R.L. Van Meirhaeghe, and C. Detavernier. Atomic layer deposition of titanium nitride from TDMAT precursor. *Microelectronic Engineering*, 86(1):72–77, January 2009.

[87] Polly Wanda Chu. *Ultrahigh vacuum metalorganic chemical vapor deposition and in situ characterization of nanoscale titanium dioxide films.* PhD thesis, Cornell University, Cornell, USA, 1994.

[88] Adriana Szeghalmi, Michael Helgert, Robert Brunner, Frank Heyroth, Ulrich Gösele, and Mato Knez. Atomic layer deposition of Al_2O_3 and TiO_2 multilayers for applications as bandpass filters and antireflection coatings. *Applied Optics*, 48(9):1727–1732, March 2009.

[89] J.A. Woolam, B. Johs, C. Herzinger, J. Hilfiker, R. Synowicki, and C. Bungay. Overview of variable angle spectroscopic ellipsometry (VASE), part i: Basic theory and typical applications. In *SPIE Proceedings*, 1999.

[90] Mikko Ritala, Markku Leskela, Lauri Niinisto, and Pekka Haussalo. Titanium isopropoxide as a precursor in atomic layer epitaxy of titanium dioxide thin films. *Chemistry of Materials*, 5(8):1174–1181, August 1993.

[91] Jeremy K. Burdett, Timothy Hughbanks, Gordon J. Miller, James W. Richardson, and Joseph V. Smith. Structural-electronic relationships in inorganic solids: powder neutron diffraction studies of the rutile and anatase polymorphs of titanium dioxide at 15 and 295 k. *Journal of the American Chemical Society*, 109(12):3639–3646, June 1987.

[92] C. Legrand and J. Delville. Sur les paramètres cristallins du rutile et de l'anatase. *Comptes Rendus Hebdomadaires des Seances de l Academie des Sciences*, 236(1):944, 1953.

[93] E.P. Meagher and G.A. Lager. Polyhedral thermal expansion in the TiO_2 polymorphs; refinement of the crystal structures of rutile and brookite at high temperature. *The Canadian Mineralogist*, 17:77–85, 1979.

[94] A. Rahtu and M. Ritala. Reaction mechanism studies on titanium Isopropoxide–Water atomic layer deposition process. *Chemical Vapor Deposition*, 8(1):21–28, 2002.

[95] G. Luka, L. Wachnicki, B.S. Witkowski, T.A. Krajewski, R. Jakiela, E. Guziewicz, and M. Godlewski. The uniformity of al distribution in aluminum-doped zinc oxide films grown by atomic layer deposition. *Materials Science and Engineering: B*, 176(3):237–241, February 2011.

[96] Vesa Lujala, Jarmo Skarp, Markku Tammenmaa, and Tuomo Suntola. Atomic layer epitaxy growth of doped zinc oxide thin films from organometals. *Applied Surface Science*, 82-83:34–40, December 1994.

[97] Andreas Frölich and Martin Wegener. Spectroscopic characterization of highly doped ZnO films grown by atomic-layer deposition for three-dimensional infrared metamaterials. *Optical Materials Express*, 1(5):883–889, September 2011.

[98] J. W. Elam and S. M. George. Growth of ZnO/Al_2O_3 alloy films using atomic layer deposition techniques. *Chemistry of Materials*, 15(4):1020–1028, February 2003.

[99] Isabelle Philippa Staude. *Functional Elements in Three-Dimensional Photonic Bandgap Materials*. PhD thesis, Karlsruhe Institute of Technology, Karlsruhe, 2011.

[100] Valeri P. Tolstoy, Irina V. Chernyshova, and Valeri A. Skryshevsky. *Handbook of Infrared Spectroscopy of Ultrathin Films*. John Wiley & Sons, Hoboken, New Jersey, 2003.

[101] Seong Keun Kim, Cheol Seong Hwang, Sang-Hee Ko Park, and Sun Jin Yun. Comparison between ZnO films grown by atomic layer deposition using H_2O or O_3 as oxidant. *Thin Solid Films*, 478(1-2):103–108, May 2005.

[102] Jin Yong Kim, Yong-June Choi, Hyung-Ho Park, Stephen Golledge, and David C. Johnson. Effective atomic layer deposition procedure for Al-dopant distribution in ZnO thin films. *Journal of Vacuum Science & Technology A: Vacuum, Surfaces, and Films*, 28(5):1111, 2010.

[103] Jeong-Seok Na, Giovanna Scarel, and Gregory N. Parsons. In situ analysis of dopant incorporation, activation, and film growth during thin film ZnO and ZnO:Al atomic layer deposition. *The Journal of Physical Chemistry C*, 114(1):383–388, January 2010.

[104] Benjamin Richter, Thomas Pauloehrl, Johannes Kaschke, Dagmar Fichtner, Joachim Fischer, Alexandra M. Greiner, Doris Wedlich, Martin Wegener, Guillaume Delaittre, Christopher Barner-Kowollik, and Martin Bastmeyer. Three-dimensional microscaffolds exhibiting spatially resolved surface chemistry. *Nature Materials*, (submitted), 2013.

[105] Han-Ki Kim, J. W. Bae, T.-K. Kim, K.-K. Kim, T. Y Seong, and I. Adesida. Inductively coupled plasma reactive ion etching of ZnO using BCl_3-based plasmas. *Journal of Vacuum Science Technology B: Microelectronics and Nanometer Structures*, 21(4):1273–1277, 2003.

[106] Isabelle Staude, Christopher McGuinness, Andreas Frölich, Robert L. Byer, Eric Colby, and Martin Wegener. Waveguides in three-dimensional photonic bandgap materials for particle-accelerator on a chip architectures. *Optics Express*, 20(5):5607–5612, February 2012.

[107] J. H. Moon, Y. Xu, Y. Dan, S.-M. Yang, A. T. Johnson, and S. Yang. Triply periodic bicontinuous structures as templates for photonic crystals: A pinch-off problem. *Advanced Materials*, 19(11):1510–1514, 2007.

[108] Andreas Frölich, Joachim Fischer, Thomas Zebrowski, Kurt Busch, and Martin Wegener. Titania woodpiles with complete three-dimensional photonic bandgaps in the visible (accepted). *Advanced Materials*, 2013.

[109] H. Ibach. Thermal expansion of silicon and zinc oxide (II). *physica status solidi (b)*, 33(1):257–265, 1969.

[110] David M. King, Xinhua Liang, Casey S. Carney, Luis F. Hakim, Peng Li, and Alan W. Weimer. Atomic layer deposition of UV-Absorbing ZnO films on SiO_2 and TiO_2 nanoparticles using a fluidized bed reactor. *Advanced Functional Materials*, 18(4):607–615, 2008.

[111] M. Deubel, M. Wegener, S. Linden, and G. von Freymann. Angle-resolved transmission spectroscopy of three-dimensional photonic crystals fabricated by direct laser writing. *Applied Physics Letters*, 87(22):221104–221104–3, November 2005.

[112] Jens Küchenmeister, Thomas Zebrowski, and Kurt Busch. A construction guide to analytically generated meshes for the fourier modal method. *Optics Express*, 20(16):17319–17347, July 2012.

[113] Lifeng Li. Formulation and comparison of two recursive matrix algorithms for modeling layered diffraction gratings. *Journal of the Optical Society of America A*, 13(5):1024–1035, May 1996.

[114] Lifeng Li. New formulation of the fourier modal method for crossed surface-relief gratings. *Journal of the Optical Society of America A*, 14(10):2758–2767, October 1997.

[115] Thomas Zebrowski. *The Full Anisotropic Adaptive Fourier Modal Method and its Application to Periodic and Aperiodic Photonic Nanostructures*. PhD thesis, Karlsruhe Institute of Technology (KIT, Karlsruhe, Germany, 2012.

[116] A. Femius Koenderink, Ad Lagendijk, and Willem L. Vos. Optical extinction due to intrinsic structural variations of photonic crystals. *Physical Review B*, 72(15):153102, October 2005.

[117] A. Femius Koenderink and Willem L. Vos. Optical properties of real photonic crystals: anomalous diffuse transmission. *Journal of the Optical Society of America B*, 22(5):1075–1084, May 2005.

[118] S. Hüfner. *Photoelectron Spectroscopy: Principles and Applications*. Springer, Berlin, 1995.

[119] Benjamin Richter. *Selektive Funktionalisierung driedimensionaler Mikrostrukturen für kontrolliertes Zellwachstum.* Diplomarbeit, Universität Karlsruhe (TH), 2010.

[120] Andrea Scheiwe. Unpublished results.

Acknowledgments

At this point it is my great pleasure to say thank you to everyone who has contributed to the success of the last four years.

First, I would like to thank my supervisor, Prof. Dr. Martin Wegener for giving me the opportunity to work on the topics of photonic crystals and metamaterials in his group. His profound knowledge and his feedback have been extremely beneficial to the progress of this thesis. I think that it is a unique opportunity to work in an excellent environment such as the one he creates in his group. It was a pleasure and I consider it a privilege to be working on something that has truly never been done before. Finally, I am also grateful to him for the opportunity to visit conferences, not only to present my work, but also to get in touch with other scientists in the field of atomic layer deposition.

I would also like to thank Prof. Dr. Kurt Busch for agreeing to co-referee this thesis and for the succesful cooperation on the photonic crystal projects.

Dr. Joachim Fischer, deserves a special thanks for his groundbreaking work on STED-DLW without which the part of this thesis that I like the most would not have been possible. I would also like to thank him in general for the very successful and pleasant cooperation.

Thomas Zebrowski has also contributed to the success of the work of the last years by making it possible to compare measured data to theoretical prediction. This fruitful cooperation has resulted in two publications and I am happy to have the opportunity to thank him for this here.

Thanks also go to Alexandru Vlad with whom I had the pleasure to work on a different approach to the fabrication of photonic crystals.

It was an equally great pleasure to collaborate with Isabelle Staude, Justyna Gansel and Tiemo Bückmann on other successful projects.

In all these projects, the ability to have a look at the inside of the structures we made was invaluable. For this, Patrice Brenner deserves thanks and a tip to the hat for his skilled operation of the focused ion beam machine.

I am sure that the work of the last years would not have been nearly as successful and

enjoyable without the continuous support and the good humour of all current and past members of the Wegener group, and I would like to say thanks to all of them for this. I would also like to thank Christian Wolff, with whom it was always possible to have an inspiring and informative discussion. Furthermore, Tiemo Bückmann, Joachim Fischer, Martin Husnik, Jonathan Müller, Benjamin Richter, Andrea Scheiwe, Robert Schittny, and Thomas Zebrowksi are gratefully acknowledged for proof-reading this thesis.

This is also the opportunity to thank everyone who keeps the things that I need to work running in the background smoothly. Besides Michael Hippe, Helmut Lay and Werner Gilde from the electronics workshop, I am happy to thank the mechanical workshop for the continuous, quick and unproblematic support and I mention Werner Wagner, who always asked me until when I needed something and was never appalled by the answer.

Johann Westhauser, the technician of our group was also very helpful in the last years. Thank you.

Without Renate Helfen and Claudia Alaya, the institute's secretaries, things would not have run as smoothly as they did. I always appreciated their helpfulness and probably do not even know everything they have kept off my back.
Finally, it is my pleasure to thank my friends and family for the interest in my progress and their support in the last years.